

Evidence for a \mathbb{Z}_2 Dirac spin liquid in the generalized Shastry-Sutherland model

Atanu Maity,^{1,2} Francesco Ferrari,^{2,3} Sylvain Capponi,⁴ Karlo Penc,^{5,2} Janik Potten,¹ Tobias Müller,¹ Andreas Feuerpfel,¹ Ronny Thomale,^{1,2} Jong Yeon Lee,^{6,*} Rhine Samajdar,^{7,8,†} and Yasir Iqbal^{2,‡}

¹*Institut für Theoretische Physik und Astrophysik and Würzburg-Dresden Cluster of Excellence ctd.qmat, Julius-Maximilians-Universität Würzburg, Am Hubland, Campus Süd, Würzburg 97074, Germany*

²*Department of Physics and Quantum Centre of Excellence for Diamond and Emergent Materials (QuCenDiEM), Indian Institute of Technology Madras, Chennai 600036, India*

³*Institut für Theoretische Physik, Goethe Universität Frankfurt, Max-von-Laue-Straße 1, 60438 Frankfurt am Main, Germany*

⁴*Univ Toulouse, CNRS, Laboratoire de Physique Théorique, Toulouse, France.*

⁵*Institute for Solid State Physics and Optics, Wigner Research Centre for Physics, H-1525 Budapest, P.O. Box 49, Hungary*

⁶*Department of Physics and Anthony J. Leggett Institute for Condensed Matter Theory, University of Illinois at Urbana-Champaign, Urbana, IL 61801, USA*

⁷*Department of Physics, Princeton University, Princeton, NJ 08544, USA*

⁸*Princeton Center for Theoretical Science, Princeton University, Princeton, NJ 08544, USA*

We present a multimethod investigation into the nature of the recently reported quantum spin liquid (QSL) phase in the spin-1/2 Heisenberg antiferromagnet on the Shastry-Sutherland lattice. A comprehensive projective symmetry group classification of fermionic mean-field *Ansätze* on this lattice yields 46 U(1) and 80 \mathbb{Z}_2 states. Using density-matrix renormalization group (DMRG) and exact diagonalization calculations, we find that the Shastry-Sutherland model and the square-lattice J_1 - J_2 Heisenberg antiferromagnet share the same QSL phase. Motivated by this observation, we establish an explicit mapping of our *Ansätze* to those on the square lattice, and identify the counterpart of the square-lattice \mathbb{Z}_2 Dirac QSL (Z2Azz13) in the Shastry-Sutherland system. Employing state-of-the-art variational Monte Carlo calculations with Gutzwiller-projected wavefunctions, further improved by Lanczos steps, we demonstrate excellent agreement in both energies and correlation functions between a gapless (Dirac) \mathbb{Z}_2 spin liquid—characterized by only a few variational parameters—and results obtained from neural quantum states and DMRG. Finally, we apply the recently developed Keldysh formulation of the pseudo-fermion functional renormalization group to compute the dynamical spin structure factor. The resulting spectra exhibit features consistent with Dirac cones in the excitation spectrum, providing strong independent evidence for a Dirac QSL ground state. Our identification of a d -wave pairing \mathbb{Z}_2 Dirac QSL is consistent with recently observed signatures of QSL behavior in $\text{Pr}_2\text{Ga}_2\text{BeO}_7$ and outlines predictions for future experiments.

I. INTRODUCTION

The celebrated spin-1/2 Heisenberg antiferromagnet on the Shastry-Sutherland lattice presents a rare example of a two-dimensional spin model which admits an *exact* solution for its ground state [1]. This Archimedean lattice, which is also called the snub square or $(3^2, 4, 3, 4)$ lattice, features two symmetry-inequivalent bonds, and the Shastry-Sutherland model (SSM) is defined on this lattice as

$$\hat{H} = J_s \sum_{\langle i,j \rangle_{\text{square}}} \hat{\mathbf{S}}_i \cdot \hat{\mathbf{S}}_j + J_d \sum_{\langle i,j \rangle_{\text{dimer}}} \hat{\mathbf{S}}_i \cdot \hat{\mathbf{S}}_j. \quad (1)$$

Here, \mathbf{S}_i denotes the SU(2) spin operator acting on the spin $S = 1/2$ representation at site i . The nearest-neighbor antiferromagnetic exchange is given by J_s , with the first sum in Eq. (1) running over all the bonds of

the square lattice. The next-nearest-neighbor interaction is represented by J_d and the second sum runs over the additional diagonal bonds introduced on every other plaquette of the square lattice, creating a pattern of alternating dimers [see Fig. 1(b)]. In the limit $J_s/J_d = 0$, the Hamiltonian reduces to one consisting of decoupled dimers and the ground state is given by a tensor product of singlets with an energy of $-3/8 J_d$ per site. This state is always an exact eigenstate of Eq. (1) and remains the ground state till a finite critical J_s/J_d . The opposite limit, $J_s/J_d \rightarrow \infty$, yields the Heisenberg model on the square lattice, which has a two-sublattice Néel-ordered ground state.

Over the past few decades, the SSM has been the focus of extensive theoretical efforts to map out the phase diagram of Eq. (1), with interest intensifying in particular after the discovery of $\text{SrCu}_2(\text{BO}_3)_2$ [2, 3], which is well approximated by this model¹. Other intriguing compounds in the family of Shastry-Sutherland lat-

* jongyeon@illinois.edu

† rhine_samajdar@princeton.edu

‡ yiqbal@physics.iitm.ac.in

¹ The role of interlayer couplings in accurately describing its behavior has lately been appreciated [4].

tice materials have also attracted much attention lately, due to their promise for hosting exotic nonmagnetic ground states, possibly QSLs, as well as exciting possibilities to realize altermagnetism [5]. These include rare-earth magnets such as $\text{BaCe}_2\text{ZnS}_5$ [6], $\text{Pr}_2\text{Ga}_2\text{BeO}_7$ [7], $\text{Pr}_2\text{Be}_2\text{GeO}_7$ [8], $\text{Yb}_2\text{Be}_2\text{GeO}_7$ [9], $\text{Er}_2\text{Be}_2\text{SiO}_7$ [10], and $\text{Er}_2\text{Be}_2\text{GeO}_7$ [11, 12].

With regard to the ground-state phase diagram of Eq. (1), while most early works advocated for a direct transition between the dimer and Néel phases [13–15], one of the first studies based on Schwinger-boson mean-field theory [16], and subsequent variational calculations [17], found an intermediate state with helimagnetic order, which is known to be the classical ($S \rightarrow \infty$) ground state [1]. Later investigations based on series expansion, stochastic state selection [18], coupled-cluster [19], and perturbative [20, 21] methods introduced the possibility of a gapped nonmagnetic intermediate phase, with either plaquette [22, 23] or columnar [24] valence bond crystal (VBC) order. The presence of plaquette order was subsequently confirmed by a large- N expansion based on a generalization to $Sp(2N)$ symmetry [25], exact diagonalization and a combination of dimer- and quadrumer-boson methods [26], triplon mean-field analysis [27], two-step density-matrix renormalization group (DMRG) [28], and $D = 2$ projected entangled pair states [29]. More recently, numerical quantum many-body approaches using tensor networks [30], DMRG [31], and the pseudo-fermion functional renormalization group (pf-FRG) [32] have established the presence of a plaquette-ordered ground state.

Today, the existence of an intermediate plaquette VBC phase between the dimer and Néel orders has found broad consensus. This VBC breaks reflection symmetry across the lines containing the J_d bonds, implying a twofold degenerate ground state, and features resonating singlets on “empty” plaquettes (with no J_d bonds). In $\text{SrCu}_2(\text{BO}_3)_2$, a plaquette VBC, likely ascribed to broken fourfold rotation symmetry about the centers of the empty squares, has been realized under the application of hydrostatic pressure [33, 34]. Thermodynamic measurements under high pressure have also provided evidence for the exciting possibility of a deconfined quantum critical point (DQCP) between Néel order and the plaquette VBC [35]. Theoretical evidence for a continuous transition between the plaquette VBC and Néel-ordered states, and a resultant DQCP exhibiting emergent $O(4)$ symmetry, has been provided by a combination of infinite density-matrix renormalization group (iDMRG) calculations and field-theoretic analysis [31], as well as recent tensor-network studies [36]. Other works have argued for a weak first-order transition between these phases [37–39] and suggested that the DQCP might instead be proximate in parameter space [37, 40]. A recent field-theoretic study [41] by some of us formulated a fermionic gauge theory for the transition, characterizing it as a pseudo-critical point with emergent $SO(5)$ symmetry that nat-

urally accommodates a gapless \mathbb{Z}_2 Dirac spin liquid between the adjacent VBC and Néel phases.

In contrast to both these scenarios, recent numerical investigations using DMRG [42], exact diagonalization [43–45], pf-FRG [32], and state-of-the-art neural-network quantum states [46, 47] have all reported the presence of a QSL phase sandwiched between the plaquette VBC and Néel-ordered states. This QSL phase occupies a narrow parameter range, $0.77 \lesssim J_s/J_d \lesssim 0.82$ [42, 46]. This raises the question of whether one can (i) explore an extended parameter space to widen the window of QSL behavior, and (ii) identify its precise microscopic character, i.e., if it is gapped or gapless, as well as the nature of its low-energy gauge group.

In this work, using a combination of DMRG and exact diagonalization calculations, we demonstrate that a broader “river” of spin liquidity can be accessed by activating antiferromagnetic exchange couplings on all the “other” diagonal bonds (within the square plaquettes) that were originally excluded in the Shastry-Sutherland geometry. As the strength of these additional interactions is increased, we observe no signs of a phase transition all the way to the square-lattice J_1 – J_2 limit. This suggests the intriguing possibility that the quantum spin liquids realized in the two models are adiabatically connected and therefore belong to the same quantum phase. Our analysis rigorously establishes this continuity using both numerical diagnostics and the framework of projective symmetry groups (PSGs). Unlike conventional ordered phases, which are characterized by spontaneous symmetry breaking and local order parameters, quantum spin liquids exhibit a more subtle form of organization known as “quantum order”. In this case, global symmetries are preserved, but they are implemented projectively on emergent fractionalized excitations such as spinons. This projective symmetry structure, captured systematically by the PSG classification, determines the allowed operators in the low-energy gauge theory and thereby fixes the universality class of the spin liquid.

Quantifying the width of the spin-liquid regime, we find that not only does it extend continuously from the square lattice to the Shastry-Sutherland but it also retains a finite extent in the parameter space of the latter, thus yielding new evidence for a robust QSL phase in the SSM. We find that the shared phase is a gapless \mathbb{Z}_2 Dirac quantum spin liquid, characterized by linearly dispersing spinon excitations at symmetry-protected Dirac nodes and an emergent gapped \mathbb{Z}_2 gauge field. Physically, such a state exhibits algebraically decaying spin correlations, broad continuum features in the dynamical structure factor rather than sharp magnon modes, and fractionalized spin-1/2 quasiparticles as its elementary excitations.

Importantly, the PSG construction does not merely enumerate symmetric parton *Ansätze*; as mentioned above, it determines how lattice symmetries act pro-

jectively on fractionalized spinons and thereby fixes the symmetry-allowed structure of the emergent gauge theory. Within this framework, the Dirac spin liquid naturally emerges as a parent state from which Néel and VBC phases can be obtained via Higgs instabilities, placing the Shastry-Sutherland and square-lattice models within a unified description of fermionic deconfined criticality.

II. CONNECTION TO THE SQUARE-LATTICE J_1 - J_2 HEISENBERG MODEL

Previous studies using variational Monte Carlo (VMC) [48, 49], many-variable VMC [50], neural-network wavefunctions [51], DMRG [52], and tensor networks [53, 54] have offered evidence for the presence of a gapless spin liquid sandwiched between the Néel and VBC phases in the $S = 1/2$ square-lattice Heisenberg model with nearest-neighbor (J_1) and next-nearest-neighbor (J_2) couplings. On the other hand, as noted above, numerical simulations on the J_s - J_d SSM point to a variety of possibilities, including weakly first-order or continuous phase transitions or a gapless QSL phase. Given the geometric similarity between these two models, we introduce the following Hamiltonian which straightforwardly interpolates between them [37]:

$$\hat{H} = J_s \sum_{\langle\langle i,j \rangle\rangle} \hat{\mathbf{S}}_i \cdot \hat{\mathbf{S}}_j + J_d \sum_{\langle\langle i,j \rangle\rangle_{\text{dimer}}} \hat{\mathbf{S}}_i \cdot \hat{\mathbf{S}}_j + J'_d \sum_{\langle\langle i,j \rangle\rangle_{\text{orthogonal}}} \hat{\mathbf{S}}_i \cdot \hat{\mathbf{S}}_j + J_{\square} \sum_{\langle\langle i,j \rangle\rangle_{\text{other}}} \hat{\mathbf{S}}_i \cdot \hat{\mathbf{S}}_j. \quad (2)$$

These couplings are pictorially depicted in Fig. 1(c). In addition to the standard nearest-neighbor and dimer interactions of the SSM, denoted by J_s and J_d , respectively, we introduce two additional exchange couplings. Specifically, J'_d labels the interactions on dimers that are orthogonal to those present in the original Shastry-Sutherland lattice, while J_{\square} denotes the interactions on the square plaquettes that are vacant in the SSM.

With these definitions, the limit $J'_d = J_{\square} = 0$ reduces to the SSM, whereas the isotropic limit $J'_d = J_d = J_{\square}$ corresponds to the square-lattice J_1 - J_2 model. In the following, to interpolate continuously between the Shastry-Sutherland and square-lattice geometries, we vary a single tuning parameter defined as $\mathcal{J} \equiv J'_d = J_{\square}$.

A. Density-matrix renormalization group

In Fig. 1, we illustrate the schematic phase diagram for this Hamiltonian, where the approximate phase boundaries are obtained from iDMRG simulations on an infinite cylinder with a circumference of length $L = 10$ and a bond dimension $\chi = 2000$. In the hatched white region—which is studied more thoroughly in the next subsection—the

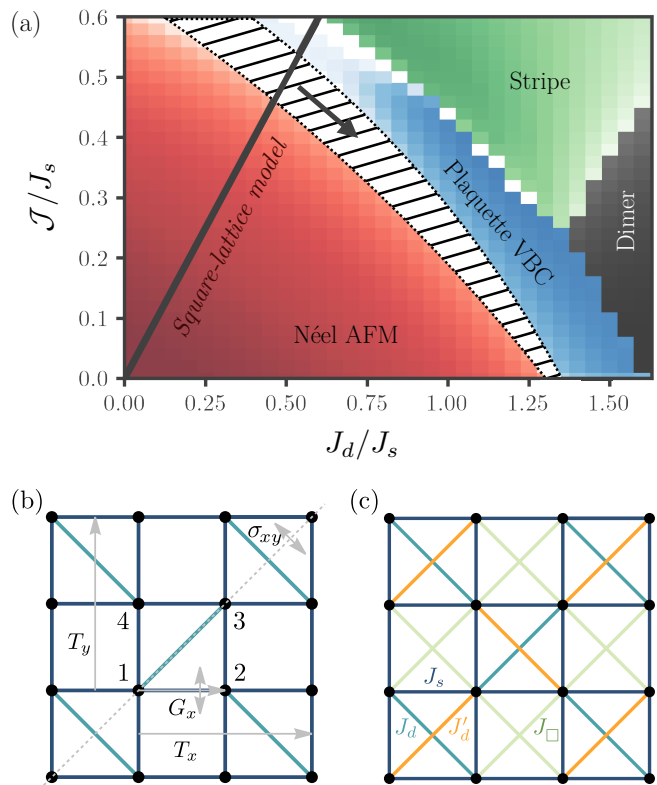


FIG. 1. (a) Schematic quantum ground-state phase diagram of the Hamiltonian (2) interpolating between the square-lattice J_1 - J_2 Heisenberg and Shastry-Sutherland models. The solid line in the figure indicates the parameters of the square-lattice model, while the horizontal axis corresponds to the pure SSM. The shading of the color conveys the strength of the appropriate order parameter as computed using iDMRG (Sec. II A). The hatched region indicates the extent of the gapless spin liquid phase identified in our exact diagonalization calculations (Sec. II B). (b) Structure of the Shastry-Sutherland lattice, highlighting its space-group symmetries. (c) Mapping of the Shastry-Sutherland lattice to the square lattice. The two additional types of symmetry-inequivalent bonds are denoted by orange and light green lines, respectively. In the square-lattice limit, i.e., $J_d = J'_d = J_{\square}$, all the diagonal bonds are related by symmetry.

simulation converges very slowly (or not at all, to within the conventionally accepted truncation error of 10^{-5}), with Néel and VBC order parameters that are both small and of similar magnitude. Furthermore, along the transverse direction indicated by the arrow in Fig. 1, we find no signatures of any phase transitions. This suggests that if a gapless spin liquid phase exists in the SSM as proposed in Refs. [42, 46], it should be adiabatically connected to the gapless spin liquid phase of the square-lattice J_1 - J_2 model. For the chosen bond dimension, the phase transition between the VBC and Néel phases in the SSM appears to be weakly first-order.

In the following sections, we provide extensive evidence of this spin liquid phase in the SSM based on exact di-

agonalization numerics.

B. Exact diagonalization

1. Low-energy levels and level spectroscopy

Long-range order in quantum many-body systems is characterized by the spontaneous breaking of a symmetry, manifested in nonvanishing correlation functions of the corresponding order parameters at large distances. Detecting such correlations reliably requires large system sizes, which are beyond the reach of exact diagonalization. However, a symmetry-broken phase is not only characterized by long-range correlations, but also by a characteristic structure of low-energy states: in the thermodynamic limit, symmetry breaking implies a degenerate ground-state manifold, while on finite clusters, this degeneracy is lifted into a set of low-lying states distinguished by symmetry quantum numbers. Appropriate linear combinations of these states form the symmetry-broken ground states. Exact diagonalization excels at computing symmetry-resolved low-energy spectra for small clusters and is ideal for detecting signatures of symmetry breaking.

A paradigmatic example is the Néel antiferromagnet, which breaks $SU(2)$ spin-rotation symmetry. Its finite-size spectrum exhibits the Anderson tower of states: the lowest states in each total-spin sector $S = 0, 1, 2, \dots$ form a rotor spectrum with excitation energies scaling approximately as $S(S+1)/N$, as illustrated in Fig. 2. These states are well separated from other excitations and have known quantum numbers, making the Anderson tower a robust diagnostic of magnetic long-range order in exact diagonalization studies.

Another example is the plaquette-singlet phase of the SSM, which breaks lattice symmetries. The ground-state manifold consists of two quasidegenerate singlets, denoted S_1 and S_2 , distinguished by lattice quantum numbers. The lowest magnetic excitation is a triplet T_1 , followed by a second triplet T_2 related to S_2 , and a quintuplet Q_1 .

Phase transitions between competing orders can therefore be detected via level crossings in the low-energy spectrum. In particular, one of the singlet states (S_1) is common to both the Néel and plaquette phases, while the relative ordering of the second singlet associated with plaquette order and the lowest triplet of the Anderson tower determines whether a Néel or a plaquette state is favored. Tracking these crossings and their finite-size scaling provides a controlled method for locating phase boundaries.

While such level crossings are sufficient to identify transitions into magnetically or lattice-ordered phases, the identification of an intermediate quantum-disordered phase requires additional care. In particular, one must

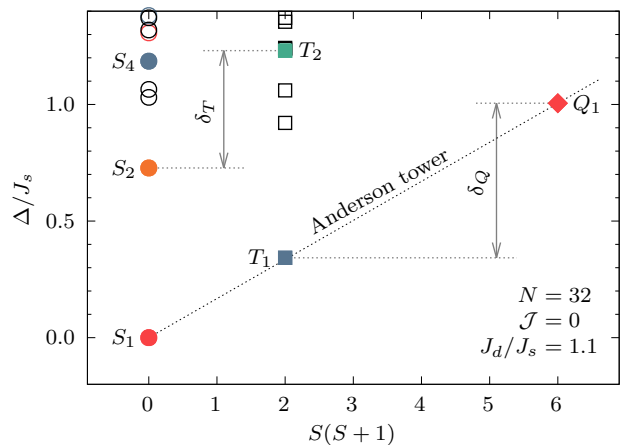


FIG. 2. Low-energy excitation spectrum of the SSM in the Néel phase, obtained from Lanczos exact diagonalization on a cluster of $N = 32$ sites at $J = 1.1$. The characteristic Anderson tower of states is clearly visible in the lowest singlet (S_1), triplet (T_1), and quintuplet (Q_1) excitations. As the level of frustration is increased toward the plaquette-singlet regime, the second singlet excitation (S_2) is observed to decrease in energy. Also indicated are the composite excitation gaps δ_T and δ_Q , as defined by Wang *et al.* [43].

distinguish the absence of order from finite-size artifacts in small clusters. A recent work by Wang *et al.* [43] introduced an improved level-spectroscopic framework for the SSM, demonstrating that composite gaps between excited states (e.g., $\delta_T = E(T_2) - E(S_2)$ or $\delta_Q = E(Q_1) - E(T_1)$) allow unusually precise identification of phase boundaries even on small periodic clusters.

In this work, we extend that framework to a family of Hamiltonians interpolating continuously between

State	S	G_x, G_y	$\sigma_{xy}, \sigma_{x\bar{y}}$	Label
S_1	0	+1	+1	A_e
S_2	0	-1	-1	A_o
S_3	0	+1	-1	B_o
S_4	0	-1	+1	B_e
T_1	1	-1	+1	B_e
T_2	1	+1	-1	B_o
Q_1	2	+1	+1	A_e

TABLE I. Symmetry quantum numbers of the low-energy states used in the level-spectroscopy analysis. All the states are considered at zero wavevector. The labels S_1, S_2, S_3 , and S_4 denote the four lowest singlets, T_1 and T_2 the two lowest triplets, and Q_1 the lowest quintuplet (although their relative ordering may vary). These symmetry labels remain valid throughout the interpolation from the SSM to the J_1 - J_2 limit, with symmetry enlargement occurring only at the latter point. The Néel state is even under the σ_{xy} and $\sigma_{x\bar{y}}$ diagonal reflections, so the states S_1, T_1 , and Q_1 in the Anderson tower have character +1. G_x and G_y denote glide reflections (see Sec. III C below).

the Shastry-Sutherland and J_1 - J_2 limits. Crucially, all lattice and spin symmetries of the SSM are preserved throughout the interpolation, with an enlargement of symmetry occurring only at the J_1 - J_2 point. This allows the same symmetry assignments and identification of low-energy states used by Ref. [43] to be applied uniformly across the full parameter space.

We focus on a small set of symmetry-resolved low-energy states that evolve continuously across all phases. In the Néel phase, the states S_1 , T_1 , and Q_1 become the lowest members of the Anderson tower, while S_2 and T_2 move to higher energies. Table I summarizes the symmetry quantum numbers of the relevant states. As all wallpaper-group and spin symmetries of the Shastry-Sutherland lattice are preserved along the interpolation, these labels remain valid across the entire parameter range, allowing unambiguous tracking of the evolution and crossings of low-energy states.

2. Symmetry-resolved spectra

Figures 3 and 4 show the symmetry-resolved low-energy spectra obtained from Lanczos exact diagonalization for clusters of $N = 32$ and $N = 36$ sites (see also Appendix A for corresponding data on $N = 20, 24, 28$, and 40 site clusters), as the model is interpolated from the Shastry-Sutherland limit to the J_1 - J_2 model. The evolution of the states S_1 , S_2 , T_1 , T_2 , and Q_1 is shown explicitly, together with the level crossings separating the Néel, spin-liquid, and singlet-ordered regimes. In Fig. 4, the downward motion of the B_o (S_3) and B_e (S_4) singlets near the J_1 - J_2 limit, together with S_1 and S_2 , signals the emergence on finite clusters of the quasidegenerate four-state manifold associated with columnar VBC order, marking the termination of the spin-liquid regime on the singlet-ordered side. In the high-symmetry J_1 - J_2 limit, these four singlets occur at momenta $(0, 0)$ ($\times 2$), $(\pi, 0)$, and $(0, \pi)$. This momentum structure is the finite-size fingerprint of columnar VBC order, distinguishing it from a plaquette VBC, which decomposes into a different set of lattice irreducible representations; see Table II of Ref. [55].

Our central result is the identification of an intermediate spin-liquid regime that separates the Néel phase from the space-group-symmetry-breaking singlet-ordered phases. Spectroscopically, within this regime we do not observe clear signatures of either $SU(2)$ spin-rotation symmetry breaking—as inferred via the Anderson tower of states—or quasidegenerate singlet manifolds signaling plaquette or columnar order. Instead, the lowest singlet and triplet excitations evolve smoothly with system size, and the relevant conventional and composite gap crossings delimit a finite-width region in parameter space.

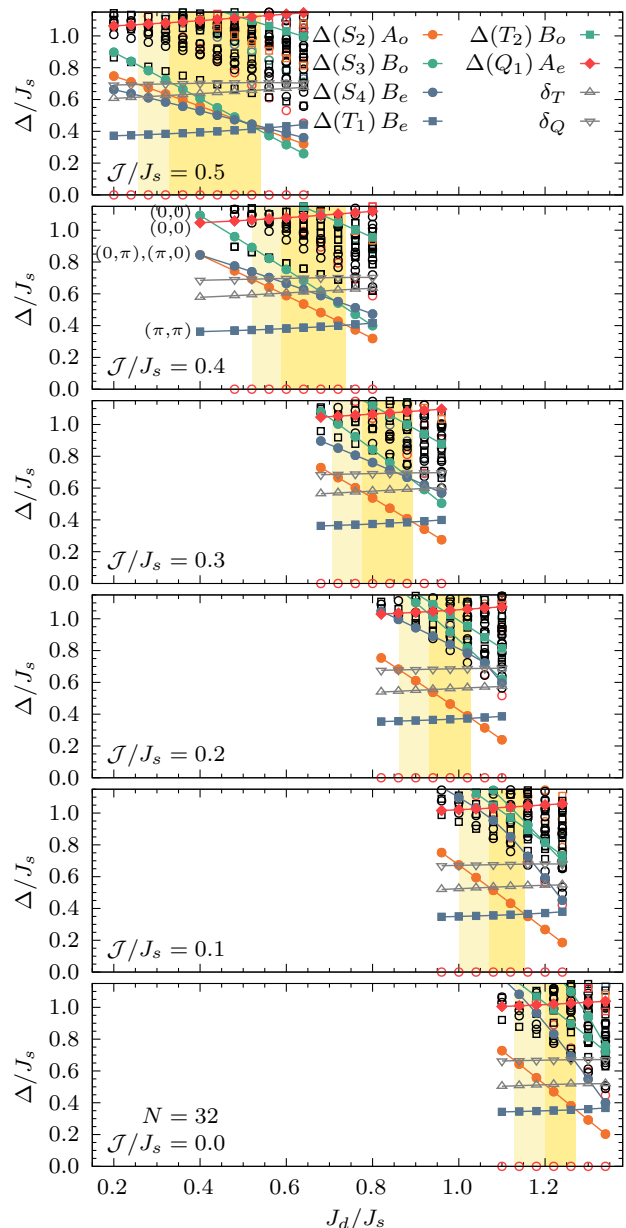


FIG. 3. Symmetry-resolved low-energy excitation spectrum obtained from Lanczos exact diagonalization for the $N = 32$ cluster as the Hamiltonian is interpolated from the Shastry-Sutherland limit toward the J_1 - J_2 model. Shown are the gaps $\Delta(S_2)$, $\Delta(T_1)$, $\Delta(T_2)$, and $\Delta(Q_1)$, together with the composite gaps δ_T and δ_Q , using the same symmetry labeling as in Fig. 4(b) of Ref. [43]. The evolution and crossings of these levels illustrate the competition between the Anderson-tower spectrum of the Néel phase and the singlet structure [$\Delta(S_1) = 0$ here and $\Delta(S_2)$] associated with plaquette ordering, and form the basis for identifying phase boundaries along the interpolation. In the $J/J_s = 0.4$ panel, the $J_d/J_s = 0.4$ point corresponds to the J_1 - J_2 model with enhanced symmetry; we indicate the $(0, 0)$, (π, π) , $(0, \pi)$, and $(\pi, 0)$ momenta (the latter two forming a two-dimensional irreducible representation in which S_2 and S_4 become degenerate). The fact that the singlets $\Delta(S_3)$ and $\Delta(S_4)$ come down upon approaching the J_1 - J_2 limit indicates the onset of columnar VBC order, which is known to be one of the competing phases [55].

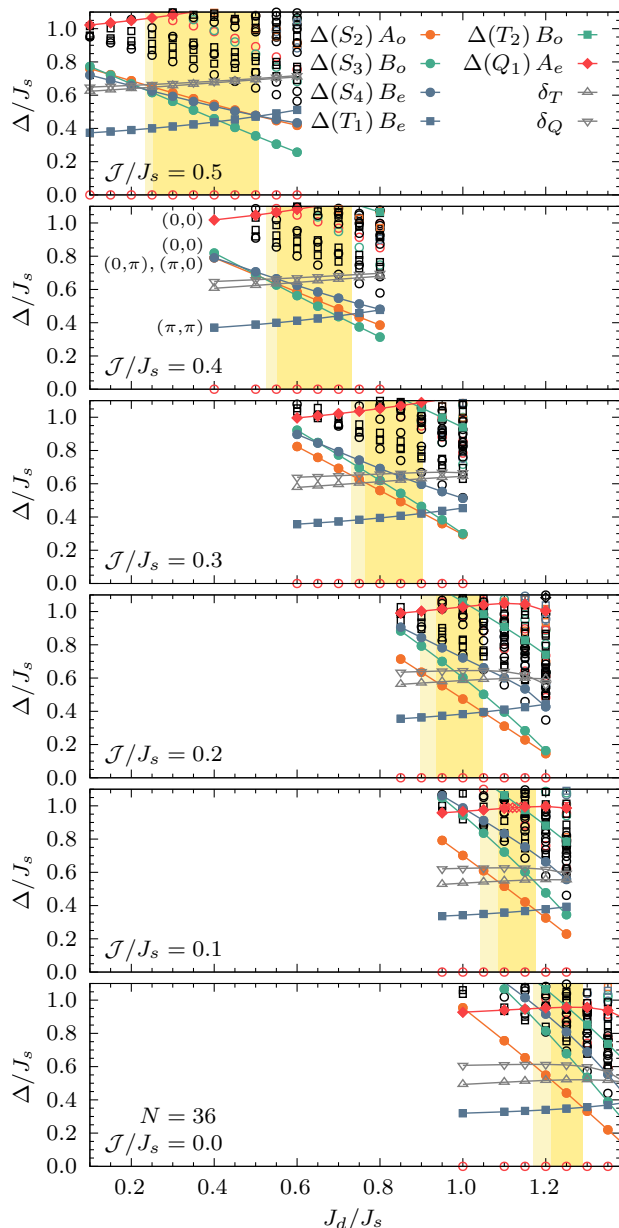


FIG. 4. Symmetry-resolved low-energy excitation spectrum obtained from Lanczos exact diagonalization for the $N = 36$ cluster as the Hamiltonian is interpolated from the Shastry-Sutherland limit to the J_1 - J_2 model. The notation and symmetry labeling are the same as in Fig. 3. The spectrum exhibits the same qualitative structure as for $N = 32$, including the evolution and crossings of the states S_1 , S_2 , T_1 , T_2 , and Q_1 . Upon approaching the J_1 - J_2 limit, an additional singlet state belonging to the B_o irreducible representation moves down in energy and eventually becomes the lowest singlet, signaling the proximity to a fourfold degenerate singlet ordered phase on the larger cluster. For the values $\mathcal{J} = J_d = 0.4J_s$, our Hamiltonian reduces to the J_1 - J_2 model with enhanced symmetry, and we indicate the momenta $(0, 0)$ of the S_3 and Q_1 states (as well as the S_1 ground state at $\Delta = 0$, unmarked), (π, π) of the T_1 state, and the two-dimensional irreducible representation with $(0, \pi)$ and $(\pi, 0)$ momenta when S_2 and S_4 become degenerate.

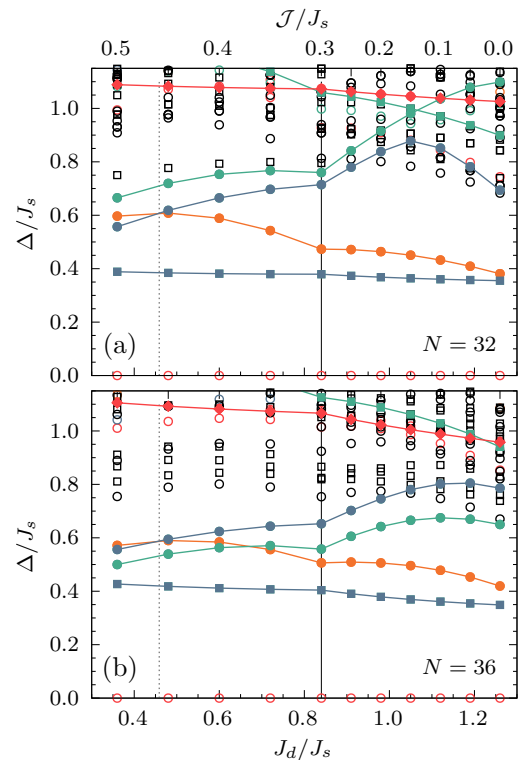


FIG. 5. Symmetry-resolved low-energy excitation spectrum obtained from Lanczos exact diagonalization along representative paths inside the river of liquidity for clusters of size (a) $N = 32$ and (b) $N = 36$. We plot the excitation gaps associated with the low-energy singlet, triplet, and quintuplet states using the same symmetry labeling as in Fig. 3. Along these trajectories, the lowest singlet and triplet levels evolve smoothly as a function of the coupling. The finite-size precursors of the columnar dimer phase, $\Delta(S_3)$ and $\Delta(S_4)$, gradually move down in energy as the J_1 - J_2 limit is approached, but do not disrupt the continuous adiabatic evolution of the spectrum within the spin-liquid regime.

3. Composite gaps and the river of liquidity

To test the internal consistency of the spin-liquid regime, we next follow the evolution of the low-energy spectrum along paths contained entirely within this extended region.

As the Hamiltonian is deformed from the Shastry-Sutherland limit toward the J_1 - J_2 model, these crossings flow continuously without qualitative reorganization, demonstrating adiabatic connectivity of the intermediate phase. The resulting spin-liquid region therefore forms a continuous *river of liquidity* along the boundary of the Neel phase (see Figs. 5 and 6), extending across the full interpolation and terminating naturally at the J_1 - J_2 point.

On the opposite boundary, adjoining the plaquette-singlet phase of the SSM and the columnar dimer phase of the J_1 - J_2 model, the dominant low-energy levels also evolve adiabatically. The only qualitative change is the

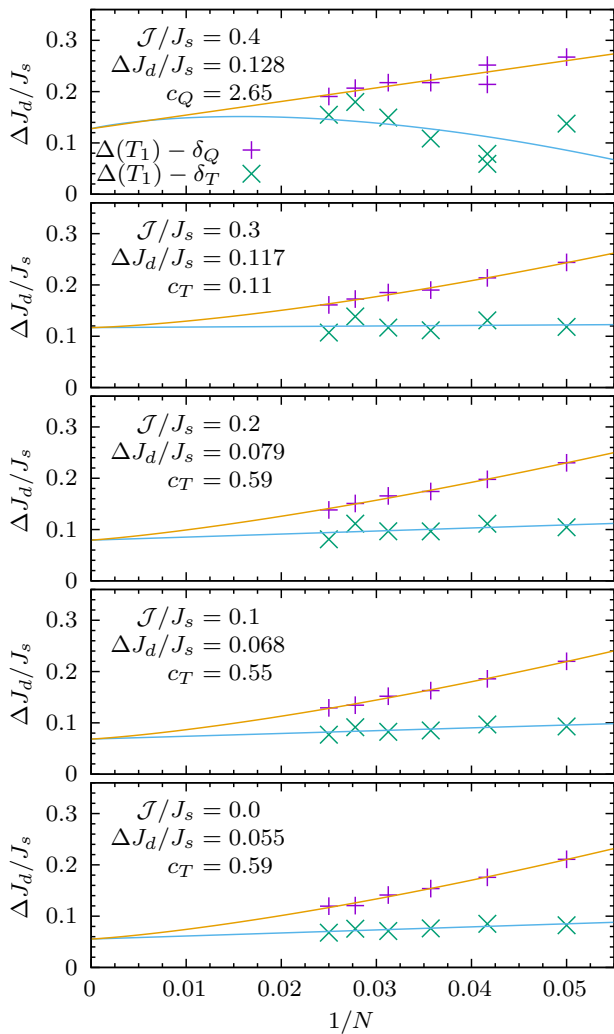


FIG. 6. Finite-size scaling of the extent of the spin-liquid regime, extracted from level-crossing points as a function of $1/N$ for several values of the interpolating coupling. The quantities shown are directly analogous to those used in Fig. 5 of Ref. [43], where crossings between excitation gaps were found to display only weak system-size dependence in the SSM. Here, we employ the same composite-gap constructions while continuously deforming the Hamiltonian toward the square-lattice J_1 - J_2 limit. For each set of parameters, the separation between the relevant crossing points remains finite upon extrapolation to the thermodynamic limit, indicating that the spin-liquid regime identified in the SSM persists throughout the interpolation. Please refer to Appendix A for ED data on $N = 20, 24, 28$, and 40 sites.

gradual appearance of additional singlet states associated with the enlarged degeneracy of the columnar dimer phase. These states “creep in” from higher energies on finite clusters and do not signal a breakdown of adiabatic continuity of the liquid regime, but rather the onset of lattice-symmetry breaking.

The accuracy of composite level spectroscopy in the SSM was demonstrated by Wang *et al.* [43] and our work

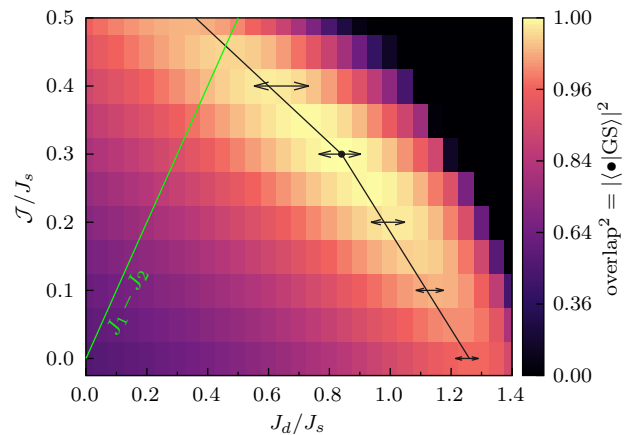


FIG. 7. Density plot of the overlap between a reference spin-liquid state (the ground state $|\bullet\rangle$ at $(J_d/J_s, J/J_s) = (0.84, 0.30)$) and the exact ground states across the space of exchange couplings for the 36-site cluster. The continuous region of high overlap coincides with the river of liquidity. The arrows indicate the extent of the spin-liquid regime as determined independently from the level crossings shown in Fig. 4. The green straight line marks the parameters corresponding to the J_1 - J_2 square-lattice Heisenberg model. The dark straight lines indicate cuts within the river of liquidity along which the excitation spectra are computed in Fig. 5.

extends this framework to reveal an adiabatically connected spin-liquid regime extending across distinct frustrated lattices.

4. Wavefunction overlap

Figure 7 provides complementary evidence for the adiabatic connectivity identified above by showing the overlap between a representative spin-liquid ground state and the exact ground states across the space of exchange couplings as a density plot. A continuous region of large overlap traces the river of liquidity along the Néel boundary, confirming that the spin-liquid states are adiabatically connected across the interpolation pathway.

By combining symmetry-resolved level spectroscopy with wavefunction-overlap diagnostics, we demonstrate that the spin-liquid regime identified in the SSM extends adiabatically to the J_1 - J_2 limit on the square lattice. This river of liquidity forms a continuous boundary between Néel order and lattice-symmetry-breaking singlet phases, providing a unified spectral picture of quantum disorder in frustrated square-lattice antiferromagnets.

C. Summary of theoretical approach and results

To further shed light on the nature of the QSL in the SSM, we employ the framework of projective symmetry

groups (PSGs) [56, 57], described in Sec. III B (and extensively utilized on many two- and three-dimensional lattices [58–86]), to perform a systematic classification of fermionic mean-field states with $SU(2)$, $U(1)$, and \mathbb{Z}_2 low-energy gauge groups. Since, previous studies [42, 46] have provided evidence for a gapless spin liquid, we choose to employ the fermionic representation of spin operators, as opposed to bosonic, since the former enables a description of gapless QSLs while the latter is restricted to describing only gapped QSLs [83]. Considering QSLs which respect the full space-group symmetry as well as QSLs compatible with the lower symmetry of the adjacent plaquette VBC, we present the microscopic *Ansätze* describing these states in Sec. IV. Then, we develop a mapping between the \mathbb{Z}_2 *Ansätze* on the Shastry-Sutherland and square lattices by establishing a connection between the PSGs of the respective symmetry groups. This approach allows us to systematically narrow down the candidate wavefunctions for the potential QSL in the generalized SSM by identifying the parton *Ansätze* that can be adiabatically connected to those of the QSL phase in the J_1 – J_2 model.

In Sec. IV C, we analyze the *Ansatz* on the Shastry-Sutherland lattice that maps to the Z2Azz13 state on the square lattice—a gapless (Dirac) \mathbb{Z}_2 QSL, which is believed to provide an excellent variational description of the QSL in the J_1 – J_2 square-lattice Heisenberg model [48, 51]. To characterize this *Ansatz*, we analyze its spinon band structure and compute the mean-field dynamical and equal-time spin structure factors at $J_s/J_d = 0.80$, which lies within the putative QSL phase [32, 42, 43, 46]. We identify the state to be a gapless \mathbb{Z}_2 Dirac quantum spin liquid with d -wave pairing. In the absence of pairing, the hopping structure produces Dirac nodes at $(\pi/2, \pi/2)$ and symmetry-related momenta, protected by the projective implementation of lattice symmetries. Upon inclusion of d_{xy} pairing on the diagonal bonds, the underlying $U(1)$ gauge structure is Higgsed to \mathbb{Z}_2 , and each Dirac node splits into four symmetry-related cones located at $(\pi/2 \pm \varepsilon, \pi/2 \pm \varepsilon)$. The parameter ε is controlled by the pairing amplitude and reflects the shift of nodal points away from high-symmetry momenta². These Dirac cones imply linearly dispersing spinon excitations, leading to algebraically decaying spin correlations in real space. In the dynamical spin structure factor, the fractionalized spinon pairs produce broad continua rather than sharp magnon modes, with enhanced spectral weight near twice the Dirac energy and characteristic fountain-like features emerging

from the nodal points. The \mathbb{Z}_2 nature of the state reflects the gapping out of gauge fluctuations by pairing, leaving gapless fermionic quasiparticles coupled to a gapped gauge sector.

Finally, in Sec. V, we carry out a state-of-the-art variational Monte Carlo study of the corresponding Gutzwiller-projected wavefunctions supplemented with Lanczos steps, and demonstrate the excellent agreement of the energies and equal-time correlators of our \mathbb{Z}_2 Dirac QSL with those obtained from vision transformer (ViT) neural networks, DMRG, and exact diagonalization on small clusters. We find that the equal-time real-space spin–spin correlations decay as a power law with exponent $z + \eta \sim 1.3$, in excellent agreement with DMRG and neural-network results. Such algebraic decay is a hallmark of gapless quantum spin liquids and is consistent with Dirac spinons coupled to a \mathbb{Z}_2 gauge field. In contrast to a gapped \mathbb{Z}_2 state, which would exhibit exponentially decaying correlations, the observed power-law behavior directly reflects the presence of low-energy Dirac quasiparticles. Additionally, employing a novel Keldysh formulation of the pseudo-fermion functional renormalization group, we present, hitherto unreported, dynamical spin structure factors of the QSL, which reveal a remarkable consistency with the expectation of a Dirac spin liquid. Taken together, these results provide compelling evidence for a \mathbb{Z}_2 Dirac quantum spin liquid phase in the generalized Shastry-Sutherland model. Moreover, the adiabatic continuity established numerically between the Shastry-Sutherland and square-lattice limits indicates that both systems realize the same universal Dirac spin-liquid fixed point, rather than distinct lattice-specific phases. The river of liquidity therefore reflects a shared underlying infrared gauge theory. We emphasize that the projective realizations of the Shastry-Sutherland lattice symmetries are already built into the *Ansätze* and dictate its sign and amplitude structure. Hence, such an approach requires a much smaller number of variational parameters as compared to methods based on neural-network wavefunctions, DMRG, and many-variable VMC that rely on unconstrained optimizations. We also study the energetic competition of our QSL with the Néel antiferromagnet (AFM) and plaquette VBC states, and our estimates of the phase boundaries based on the intersection of energies yield $(J_s/J_d)_{\text{PVBC}} \approx 0.78$, and $(J_s/J_d)_{\text{Néel}} \approx 0.83$, which are in excellent agreement with those obtained from other numerical approaches.

In light of recent observations of gapless QSL behavior in $\text{Pr}_2\text{Ga}_2\text{BeO}_7$ [7], which can approximately be modeled by $S = 1/2$ XXZ interactions on the Shastry-Sutherland lattice, our results find additional significance. In particular, our finding of a d -wave pairing \mathbb{Z}_2 Dirac QSL is compatible with the thermodynamic signatures of a T^2 dependence of the specific heat and a finite κ_0/T arising due to a disorder-induced finite density of states [7]. Taken together with indications from Keldysh pf-FRG of the

² At $J_s/J_d = 0.8$ on a 14×14 cluster, $\varepsilon \approx 0.122\pi/2$. In the Z2Azz13 state, the Dirac cone splits into four cones at $(\pi/2 \pm \varepsilon, \pi/2 \pm \varepsilon)$ due to the d_{xy} pairing on the diagonal bonds connecting site $(0, 0)$ to $(\pm 1, \pm 1)$; instead, if we introduce the d_{xy} pairing on the $(\pm 2, \pm 2)$ bonds, the Dirac cones remain intact at $(\pi/2, \pi/2)$.

persistent signatures of Dirac cones upon introduction of XXZ anisotropy to the Heisenberg model, our work supports the scenario of a \mathbb{Z}_2 Dirac QSL thereby clarifying the microscopic identity of the QSL in $\text{Pr}_2\text{Ga}_2\text{BeO}_7$.

III. METHODOLOGY

A. Parton construction

A powerful framework to construct mean-field theories of QSLs is provided by the ‘‘parton’’ representation of spin operators. The first step in this scheme is to express the spin operators \hat{S}_i^γ ($\gamma = x, y, z$) in terms of spin-1/2, charge-neutral quasiparticles called *spinons*, which can be chosen to have either bosonic or fermionic statistics. As we are interested in describing gapped as well as gapless QSLs and the competition between them, we henceforth consider the spinons to be fermionic. In this language, the spin operator can be rewritten as a bilinear with two flavors of complex fermions [87, 88]:

$$\hat{S}_i^\gamma = \frac{1}{2} \sum_{\alpha\beta} \hat{f}_{i\alpha}^\dagger \tau_{\alpha\beta}^\gamma \hat{f}_{i\beta}. \quad (3)$$

Here, the $\hat{f}_{i\alpha}$ ($\hat{f}_{i\alpha}^\dagger$) are spinon operators which annihilate (create) a spin-1/2 fermion with flavor $\alpha \in \{\uparrow, \downarrow\}$ at site i and τ^γ ($\gamma = x, y, z$) are the three Pauli matrices. In order to make the symmetries of the fermionic representation manifest, it proves instructive to re-express Eq. (3) as

$$\hat{S}_i^\gamma = \frac{1}{2} \text{Tr} \left[\hat{\psi}_i^\dagger \tau^\gamma \hat{\psi}_i \right] \quad (4)$$

in terms of the spinor doublet $\hat{\psi}_i \equiv (\hat{\mathbf{f}}_i, \hat{\hat{\mathbf{f}}}_i)$, where $\hat{\mathbf{f}}_i = (\hat{f}_{i,\uparrow}, \hat{f}_{i,\downarrow})^T$ and $\hat{\hat{\mathbf{f}}}_i = (\hat{f}_{i,\downarrow}^\dagger, -\hat{f}_{i,\uparrow}^\dagger)^T$. Under a right multiplication $\hat{\psi}_i \rightarrow \hat{\psi}_i W_i$ with $W_i \in \text{SU}(2)$, the spin operators in Eq. (4) and the fermionic anticommutation relations of the spinons remain unaffected, i.e., such a transformation does not affect the physical observables. Thus, the fermionization of the spin operators is accompanied by a local gauge freedom associated with an internal symmetry group (ISG) [89, 90], which, in this case, is $\text{SU}(2)$. In distinction to right multiplications, a left $\text{SU}(2)$ multiplication, i.e., $\hat{\psi}_i \rightarrow G \hat{\psi}_i$ effects a rotation in spin space. Moreover, it is important to note that the fermionic Hilbert space is four-dimensional while the spin space is \mathbb{C}^2 . This necessitates the introduction of an additional constraint requiring that there be exactly one fermion per site:

$$\hat{\psi}_i \tau^\gamma \hat{\psi}_i^\dagger = 0, \quad \gamma \in \{x, y, z\}, \quad (5)$$

which ensures that the Hilbert space dimensions of the spin and spinon representations are in agreement.

Inserting Eq. (3) into a generic Heisenberg model such as, say, Eq. (1), yields a four-fermion interaction term

in the Hamiltonian, following which, we can perform a mean-field decoupling to obtain an effective quadratic Hamiltonian. Given that we intend to formulate a low-energy Hamiltonian for a spin-rotation-invariant quantum paramagnet, we restrict this decoupling to only the singlet channel. Since a spin rotation is implemented in the fermionic Hilbert space by a left $\text{SU}(2)$ multiplication, the quadratic field $\hat{\psi}_i^\dagger \hat{\psi}_j$ is manifestly spin-rotation invariant. Accordingly, the mean field in the singlet channel can be identified as $u_{ij} = \langle \hat{\psi}_i^\dagger \hat{\psi}_j \rangle$, which, in turn, consists of two subchannels χ_{ij} and Δ_{ij} :

$$u_{ij} = \begin{bmatrix} \chi_{ij} & \Delta_{ij}^\dagger \\ \Delta_{ij} & -\chi_{ij}^\dagger \end{bmatrix}. \quad (6)$$

Here, χ_{ij} and Δ_{ij} are the hopping and pairing singlet mean fields, respectively, which reside on the bond connecting sites i and j . The resulting quadratic spinon Hamiltonian for a quantum paramagnet generically takes the form

$$\begin{aligned} \hat{H}_{\text{MF}} = & \sum_{\langle ij \rangle} \frac{3}{8} J_{ij} \left[\frac{1}{2} \text{Tr}(u_{ij}^\dagger u_{ij}) - \text{Tr}(\hat{\psi}_i u_{ij} \hat{\psi}_j^\dagger + \text{H.c.}) \right] \\ & + \sum_i \sum_\gamma a_{\gamma,i} \text{Tr} \left[\hat{\psi}_i \tau^\gamma \hat{\psi}_i^\dagger \right]. \end{aligned} \quad (7)$$

The term in the second line above incorporates the constraint forbidding empty and doubly occupied sites at the mean-field level, i.e., $\langle \hat{\psi}_i \tau^\gamma \hat{\psi}_i^\dagger \rangle = 0$, using three Lagrange multipliers a_γ , with $\gamma = x, y, z$, at each site. As the spinon Hamiltonian is completely specified by $(u_{ij}, a_{\gamma,i})$, these fields together constitute an *Ansatz* for a given QSL phase. The mean-field Hamiltonian (7) is now invariant under the following gauge transformations:

$$\hat{\psi}_i \rightarrow \hat{\psi}_i W_i, \quad u_{ij} \rightarrow W_i^\dagger u_{ij} W_j, \quad a_{\gamma,i} \tau^\gamma \rightarrow a_{\gamma,i} W_i^\dagger \tau^\gamma W_i, \quad (8)$$

for $W_i \in \text{SU}(2)$. Therefore, the ISG turns out to also be the gauge-symmetry group in the mean-field construction. Next, we describe how this property leads to nontrivial symmetry operations in the fermionic Hilbert space.

B. Projective symmetry group framework

Fully symmetric QSLs are quantum paramagnets that do not spontaneously break lattice space-group and time-reversal symmetries, and consequently, cannot be characterized by local physical order parameters. In principle, QSLs may break one or more lattice symmetries and time reversal, but they still cannot be uniquely characterized by local order parameters since there can exist a plethora of QSLs breaking the very same symmetries—as occurs for chiral QSLs [69] and spin-/lattice-nematic QSLs [68, 91, 92]. To establish the invariance of an

Ansatz under different symmetry operations, one therefore has to specify how a lattice or time-reversal symmetry operation acts in the fermionic Hilbert space.

In general, an *Ansatz* given by u_{ij} is modified to $u'_{ij} = u_{\mathcal{O}(i), \mathcal{O}(j)}$ under a symmetry operation denoted by \mathcal{O} , so, at first sight, it appears that the symmetry of the *Ansatz* under \mathcal{O} is broken. However, the SU(2) gauge symmetry in the fermionic representation implies that two *Ansätze* related by a SU(2) gauge transformation label the same physical spin state. Thus, if we choose an appropriate local SU(2) matrix W_i that connects u_{ij} and u'_{ij} , the symmetry of the *Ansatz* can be restored. As a result, lattice and time-reversal symmetries are realized projectively (i.e., up to SU(2) gauge transformations) in the fermionic Hilbert space. This lays the foundation for the idea of the projective symmetry group (PSG) framework [56], whereby an *Ansatz* is invariant under a symmetry operation \mathcal{O} iff the following condition is satisfied:

$$W_{\mathcal{O}}^\dagger(\mathcal{O}(i))u_{\mathcal{O}(i)\mathcal{O}(j)}W_{\mathcal{O}}(\mathcal{O}(j)) = u_{ij}. \quad (9)$$

This combined operation of the physical symmetry element and the element of the ISG defines the PSG of an *Ansatz*. Physically, if two *Ansätze* have gauge-inequivalent PSGs, they correspond to two distinct QSL states. Accordingly, PSGs serve to characterize the internal quantum order of an *Ansatz* [57], i.e., different *Ansätze* can be distinguished and characterized by PSGs in a fashion akin to how classical solid-state phases are characterized by crystallographic space-group symmetries. Hence, a systematic classification of projective representations of given lattice space groups can serve as a powerful mathematical tool, enabling the construction of distinct QSL *Ansätze* with a desired low-energy gauge group.

To characterize the *Ansätze* in more detail, note that u_{ij} in Eq. (6) can be re-expressed in terms of four real parameters as

$$u_{ij} = i\chi_{ij}^0\tau^0 + \chi_{ij}^3\tau^z + \Delta_{ij}^1\tau^x + \Delta_{ij}^2\tau^y, \quad (10)$$

where τ^0 is the 2×2 identity matrix. Due to this structure, there always exists a group \mathbb{G} (where \mathbb{G} is either SU(2) or its subgroups U(1) and \mathbb{Z}_2) such that under gauge transformations by $\mathcal{G}_i \in \mathbb{G}$, the *Ansatz* remains invariant. The group \mathbb{G} is called the invariant gauge group (IGG) of the *Ansatz*. Another interpretation of the IGG can be seen by comparing Eqs. (9) and Eq. (11) below, which implies that the IGG is a special subgroup of the PSG corresponding to an identity symmetry operation ($\mathcal{O} = 1$).

When $u_{ij} = i\chi_{ij}^0\tau^0$, and $\chi_{ij}^3 = \Delta_{ij}^1 = \Delta_{ij}^2 = 0$, i.e., the *Ansatz* consists of only imaginary hoppings, the IGG is the global SU(2) gauge group $\{\exp(i\phi \hat{\mathbf{n}} \cdot \hat{\tau})\}$. If we include real hopping terms as well, i.e., $\Delta_{ij}^1 = \Delta_{ij}^2 = 0$, the IGG is the global U(1) gauge group $\{\exp(i\phi \tau^z)\}$ while the inclusion of pairing terms breaks the IGG down to

global \mathbb{Z}_2 , $\{\pm 1\}$. The three different IGGs discussed in this example only involve *global* gauge elements; these correspond to the so-called canonical structures of the *Ansätze*. In canonical form, SU(2) *Ansätze* contain only imaginary hopping terms, U(1) *Ansätze* include only real and imaginary hopping amplitudes, and \mathbb{Z}_2 *Ansätze* can take any generic form. However, owing to the SU(2) gauge redundancy, the elements of the IGG need not always constitute a global gauge group, and the invariance of an *Ansatz* may require the following generic local operation:

$$\mathcal{G}_i^\dagger u_{ij} \mathcal{G}_j = u_{ij}, \quad \mathcal{G} \in \text{IGG}. \quad (11)$$

Thus, in general, the IGG is a *local* gauge group.

C. Symmetries of the Shastry-Sutherland model

The symmetries of the Shastry-Sutherland lattice [see Fig. 1(b)] correspond to the $p4g$ wallpaper group. Let the positions of the lattice sites in the Cartesian coordinate system be denoted by

$$\mathbf{r} \equiv (x, y) \equiv (x\hat{\mathbf{x}} + y\hat{\mathbf{y}})a, \quad (12)$$

where a is the lattice parameter. The symmetry generators and their actions on a lattice site are then as follows [31]:

$$\begin{aligned} T_x(x, y) &\rightarrow (x + 2, y), \\ T_y(x, y) &\rightarrow (x, y + 2), \\ G_x(x, y) &\rightarrow (x + 1, -y), \\ G_y(x, y) &\rightarrow (-x, y + 1), \\ \sigma_{xy}(x, y) &\rightarrow (y, x), \\ \sigma_{x\bar{y}}(x, y) &\rightarrow (-y + 1, -x + 1), \\ C_4(x, y) &\rightarrow (-y + 2, x - 1). \end{aligned} \quad (13)$$

Here, T_x and T_y stand for translations by $2a\hat{\mathbf{x}}$ and $2a\hat{\mathbf{y}}$, respectively, on the underlying Bravais (square) lattice. The operations G_x (G_y) are glide reflections, combining a translation $a\hat{\mathbf{x}}$ ($a\hat{\mathbf{y}}$) with a reflection across the x - (y -) axis. The symmetries σ_{xy} and $\sigma_{x\bar{y}}$ denote reflections across the two diagonal axes, while C_4 represents fourfold rotations about the centers of the empty squares. Note that T_x , T_y , G_y , $\sigma_{x\bar{y}}$, and C_4 can be expressed in terms of G_x and σ_{xy} as

$$\begin{aligned} G_y &= \sigma_{xy} G_x \sigma_{xy}, \\ T_x &= G_x^2, \quad T_y = G_y^2, \\ \sigma_{x\bar{y}} &= \sigma_{xy} G_x G_y^{-1}, \\ C_4 &= G_x \sigma_{xy} G_x G_y^{-1} = G_x \sigma_{x\bar{y}}. \end{aligned} \quad (14)$$

Thus, G_x and σ_{xy} form a minimal set of symmetry generators for the $p4g$ wallpaper group. However, for simplicity, we include the translations T_x and T_y explicitly in the discussion hereafter.

$w_{\mathcal{T}}$	w_{G_x}	$w_{\sigma_{xy}}$	ξ_y	$\xi_{G_{xy}}$	$\bar{\phi}_{G_x,u}$	$\bar{\phi}_{\sigma_{xy},u}$	# of PSG classes
1	0	0	0	$p_{G_{xy}}\pi$	$\{0, p_{G_x T_x}\pi, 0, p_{G_x T_x}\pi + p_{G_{xy}}\pi\}$	$\{0, 0, p_{\sigma_{xy}}\pi, 0\}$	8
1	0	1	0	$p_{G_{xy}}\pi$	$\{0, p_{G_x T_x}\pi, p_{G_x T_x}\pi - p_{G_{xy}}\pi, 0\}$	$\{0, 0, p_{\sigma_{xy}}\pi, 0\}$	8
1	1	0	0	$p_{G_{xy}}\pi$	$\{0, p_{G_x T_x}\pi, 0, p_{G_x T_x}\pi - p_{G_{xy}}\pi\}$	$\{0, 0, p_{\sigma_{xy}}\pi, 0\}$	8
1	1	1	0	$p_{G_{xy}}\pi$	$\{0, p_{G_x T_x}\pi, 0, p_{G_x T_x}\pi - p_{G_{xy}}\pi\}$	$\{0, 0, p_{\sigma_{xy}}\pi, 0\}$	8
0	0	0	0	0	$\{0, 0, 0, 0\}$	$\{0, 0, p_{\sigma_{xy}}\pi, 0\}$	2
0	0	1	0	0	$\{0, 0, 0, 0\}$	$\{0, 0, p_{\sigma_{xy}}\pi, 0\}$	2
0	1	0	0	$p_{G_{xy}}\pi$	$\{0, p_{G_x T_x}\pi, 0, p_{G_x T_x}\pi - p_{G_{xy}}\pi\}$	$\{0, 0, p_{\sigma_{xy}}\pi, 0\}$	8
0	1	1	$-2\xi_{G_{xy}}$	$\xi_{G_{xy}}$	$\{0, p_{G_x T_x}\pi, 0, p_{G_x T_x}\pi - \xi_{G_{xy}}\}$	0	2

TABLE II. The 46 U(1) PSG classes, characterized by different gauge-inequivalent choices of $w_{\mathcal{O}}$, $\bar{\phi}_{\mathcal{O},u}$, and the U(1) phases ξ_{\dots} . Each vector $\{\dots\}$ lists the four values of $\bar{\phi}_{\mathcal{O},u}$ for $u = 1, \dots, 4$. The parameters p_{\dots} are binary variables, which can be either 0 or 1.

Using the notation (m, n, u) , the position of a lattice site is expressed as:

$$\mathbf{r} \equiv (r, u) \equiv (m, n, u) \equiv 2(m\hat{\mathbf{x}} + n\hat{\mathbf{y}})a + \epsilon_u, \quad (15)$$

where $u = 1, 2, 3, 4$ labels the four distinct sites within the geometric unit cell, and

$$\epsilon_1 = 0, \quad \epsilon_2 = a\hat{\mathbf{x}}, \quad \epsilon_3 = a(\hat{\mathbf{x}} + \hat{\mathbf{y}}), \quad \epsilon_4 = a\hat{\mathbf{y}}. \quad (16)$$

The symmetry operations, in this notation, are defined as:

$$\begin{aligned} T_x &: (m, n, u) \rightarrow (m+1, n, u), \\ T_y &: (m, n, u) \rightarrow (m, n+1, u), \\ G_x &: (m, n, u) \rightarrow (m + \delta_{u,2/3}, -n - \delta_{u,3/4}, G_x(u)), \\ \sigma_{xy} &: (m, n, u) \rightarrow (n, m, \sigma_{xy}(u)), \end{aligned} \quad (17)$$

where $\delta_{u,a/b} \equiv \delta_{u,a} + \delta_{u,b}$, $G_x(\{1, 2, 3, 4\}) = (\{2, 1, 4, 3\})$, and $\sigma_{xy}(\{1, 2, 3, 4\}) = (\{1, 4, 3, 2\})$.

In addition to the space-group symmetries, we need to consider time reversal \mathcal{T} given that we are dealing with fully symmetric QSL *Ansätze*. Being an internal symmetry, \mathcal{T} leaves (m, n, u) unchanged and commutes with all space-group operations. Taking \mathcal{T} into account, the symmetry group of the Shastry-Sutherland lattice is then fully specified by the following identity relations:

$$\begin{aligned} T_x^{-1}T_y^{-1}T_xT_y &= 1, \\ G_x^{-1}T_x^{-1}G_xT_x &= 1, \\ G_x^{-1}T_y^{-1}G_xT_y &= 1, \\ T_x^{-1}G_x^2 &= 1, \\ T_y^{-1}\sigma_{xy}^{-1}T_x\sigma_{xy} &= 1, \\ T_x^{-1}\sigma_{xy}^{-1}T_y\sigma_{xy} &= 1, \\ (\sigma_{xy}G_x)^4 &= 1, \\ \sigma_{xy}^2 &= 1, \\ \mathcal{T}^2 &= 1, \\ \mathcal{T}\mathcal{O}\mathcal{T}^{-1}\mathcal{O}^{-1} &= 1, \quad \mathcal{O} \in \{T_x, T_y, G_x, \sigma_{xy}\}. \end{aligned} \quad (18)$$

Finally, time-reversal symmetry acts nontrivially on the mean fields, as $\mathcal{T}(u_{ij}, a_{\gamma}) = -(u_{ij}, a_{\gamma})$ [56, 69]. This imposes the condition

$$W_{\mathcal{T}}^{\dagger}(i)u_{ij}W_{\mathcal{T}}(j) = -u_{ij}, \quad (19)$$

where $W_{\mathcal{T}} \in \text{SU}(2)$ is a site-dependent gauge transformation.

Since the physical symmetries act projectively in the fermionic Hilbert space, the group relations of Eq. (18), which are generically of the type

$$\mathcal{O}_1 \circ \mathcal{O}_2 \circ \dots = 1, \quad (20)$$

naturally translate to gauge-enriched group compositions of the type

$$\tilde{\mathcal{O}}_1 \circ \tilde{\mathcal{O}}_2 \circ \dots = (W_{\mathcal{O}_1} \circ \mathcal{O}_1) \circ (W_{\mathcal{O}_2} \circ \mathcal{O}_2) \circ \dots = \mathcal{G}, \quad (21)$$

where $\mathcal{G} \in \text{IGG}$ is a pure gauge transformation which reduces to the identity operation for spins. The complete set of PSG solutions can be obtained using the relations in Eq. (18).

Let us first consider the case where the IGG is U(1). The generic form of a U(1) PSG solution for any symmetry operator \mathcal{O} , in the canonical gauge, is given by $W_{\mathcal{O}}(m, n, u) = F_3(\phi_{\mathcal{O}}(m, n, u))(i\tau^x)^{w_{\mathcal{O}}}$, where $F_3(\lambda) \equiv \exp(i\lambda\tau^z)$, and $w_{\mathcal{O}}$ takes the values 0 and 1. However, due to the consistency conditions on G_x arising from the relations (18), there exist no solutions with $w_{\mathcal{O}} = 1$ for $\mathcal{O} \in \{T_x, T_y\}$. The solutions for $\phi_{\mathcal{O}}(m, n, u)$ can be written as

$$\phi_{T_x}(m, n, u) = y\xi_y, \quad \phi_{T_y}(m, n, u) = 0, \quad (22)$$

$$\phi_{G_x}(m, n, u) = (-1)^{w_{G_x}}(n\xi_{G_{xy}} + m\xi_y\delta_{u,3/4}) + \bar{\phi}_{G_x,u}, \quad (23)$$

$$\phi_{\sigma_{xy}}(m, n, u) = mn\xi_y + \bar{\phi}_{\sigma_{xy},u}, \quad (24)$$

$$\phi_{\mathcal{T}}(m, n, u) = u\pi\delta_{w_{\mathcal{T}},0}, \quad (25)$$

with $\bar{\phi}_{\mathcal{O},u} \equiv \phi_{\mathcal{O}}(0, 0, u)$; for details, refer to Appendix C. The different gauge-inequivalent choices of the phases

$0 \leq \xi_y, \xi_{G_{xy}}, \bar{\phi}_{G_{x,u}}, \bar{\phi}_{\sigma,u} < 2\pi$ are listed in Table II. We find a total of 46 U(1) solutions that can be realized on the Shastry-Sutherland lattice.

When the IGG is \mathbb{Z}_2 , an identity can be defined up to a global sign in the canonical gauge. The solutions for the \mathbb{Z}_2 PSGs (for details, see Appendix D) can be expressed as

$$W_{T_x}(m, n, u) = W_{T_y}(m, n, u) = \tau^0, \quad (26)$$

$$W_{G_x}(m, n, u) = \eta_{G_{xy}}^n \mathcal{W}_{G_{x,u}}, \quad (27)$$

$$W_{\sigma_{xy}}(m, n, u) = \mathcal{W}_{\sigma_{xy},u}, \quad (28)$$

$$W_{\mathcal{T}}(m, n, u) = \mathcal{W}_{\mathcal{T},u}, \quad (29)$$

where $\eta_{G_{xy}} = \pm$, and the matrices $\mathcal{W}_{\mathcal{O},u} = \mathcal{W}_{\mathcal{O}}(0, 0, u)$ matrices can be read off from Table III. While there are $2^4 \times 5 = 80$ \mathbb{Z}_2 PSGs in total, for the $\eta_{G_x \mathcal{T}} = 1$ class—in the first and fifth rows of Table III—the first-neighbor mean-field amplitudes vanish, so we need to consider only 64 \mathbb{Z}_2 PSGs.

No.	$\mathcal{W}_{\sigma_{xy},u}$	$\mathcal{W}_{\mathcal{T},u}$
1	$\{\tau^0, \tau^0, \eta_{\sigma} \tau^0, \tau^0\}$	$\{\tau^0, \eta_{G_x \mathcal{T}} \tau^0, \tau^0, \eta_{G_x \mathcal{T}} \tau^0\}$
2	$\{\tau^0, \tau^0, \eta_{\sigma} \tau^0, \tau^0\}$	$\{i\tau^y, \eta_{G_x \mathcal{T}} i\tau^y, i\tau^y, \eta_{G_x \mathcal{T}} i\tau^y\}$
3	$\{i\tau^z, i\tau^z, \eta_{\sigma} i\tau^z, i\tau^z\}$	$\{i\tau^y, \eta_{G_x \mathcal{T}} i\tau^y, i\tau^y, \eta_{G_x \mathcal{T}} i\tau^y\}$
4	$\{i\tau^z, i\tau^z, \eta_{\sigma} i\tau^z, i\tau^z\}$	$\{i\tau^z, \eta_{G_x \mathcal{T}} i\tau^z, i\tau^z, \eta_{G_x \mathcal{T}} i\tau^z\}$
5	$\{i\tau^z, i\tau^z, \eta_{\sigma} i\tau^z, i\tau^z\}$	$\{\tau^0, \eta_{G_x \mathcal{T}} \tau^0, \tau^0, \eta_{G_x \mathcal{T}} \tau^0\}$

TABLE III. Different gauge-inequivalent choices of the matrices $\mathcal{W}_{\sigma_{xy}}$ and $\mathcal{W}_{\mathcal{T}}$ appearing in Eqs. (28) and (29). In addition, Eq. (27) features a third such matrix, which is given by $\mathcal{W}_{G_{x,u}} = \{\tau^0, \eta_{G_x \mathcal{T}_x} \tau^0, \tau^0, \eta_{G_x \mathcal{T}_x} \eta_{G_{xy}} \tau^0\}$ for each row.

IV. MEAN-FIELD ANSÄTZE

Having worked out the complete set of PSGs for the Shastry-Sutherland lattice, we are now in a position to derive the different realizable symmetric mean-field *Ansätze* from these PSG solutions. Restricting the mean-field amplitudes to square-lattice bonds (nearest neighbor, NN) and diagonal bonds (next-nearest neighbor, NNN) *only*, we find a total of twelve U(1) and eighteen \mathbb{Z}_2 distinct *Ansätze*. In addition to their PSGs, all the *Ansätze* can be further characterized by defining SU(2) flux operators [56, 69], which are associated with different loops originating from a fixed base point i :

$$P_{\mathcal{C}_i} = u_{ij} u_{jk} \cdots u_{li}, \quad (30)$$

where j, k, l, \dots denote the sites included in the contour \mathcal{C}_i . Under a local SU(2) gauge transformation $W(i)$, the flux operator transforms as $P_{\mathcal{C}_i} \rightarrow W^\dagger(i) P_{\mathcal{C}_i} W(i)$, which affects all loop operators with the same base point only up to a global rotation in Pauli space. This property

provides a powerful tool for diagnosing different QSL *Ansätze*. In general, for a q -sided loop, $P_{\mathcal{C}_i}$ takes the form:

$$P_{\mathcal{C}_i}(\varphi_{\mathcal{C}_i}) \propto g_i e^{i\varphi_{\mathcal{C}_i} \tau^z} (\tau^z)^q g_i^\dagger, \quad g_i \in \text{SU}(2), \quad (31)$$

where the phase $\varphi_{\mathcal{C}_i}$ can be interpreted as a magnetic flux threading the loop \mathcal{C}_i .

Furthermore, note that the IGG of an *Ansatz* may not be obvious if the *Ansatz* is not in the canonical gauge. In that case, the disguised IGG for an *Ansatz* written in a generic gauge can be identified from the condition [69]:

$$[\mathcal{G}, P_{\mathcal{C}_i}] = 0,$$

for $\mathcal{G} \in \text{IGG}$ and all nontrivial flux loops $\{P_{\mathcal{C}_i}\}$. In the context of the Shastry-Sutherland lattice, starting from a base site at the origin, we identify four square loops and three triangular loops as illustrated in Fig. 8(a). The associated gauge fluxes are denoted by $\varphi_{s_1}, \varphi_{s_2}, \varphi_{s_3}, \varphi_{s_4}, \varphi_{t_1}, \varphi_{t_2}$, and φ_{t_3} , respectively.

In the following, we now discuss the QSL mean-field *Ansätze* for different IGGs. All these *Ansätze* are defined by simply considering the reference bonds shown in Fig. 8(b).

A. U(1) *Ansätze* on the Shastry-Sutherland lattice

To begin, we consider the different *Ansätze* realizable with IGG U(1). In this family, we demarcate the U(1) PSG solutions into eight different classes, denoted as U1, U2, \dots , U8, corresponding to the eight rows in Table II. The states are labeled by their respective classes and the parameters of the PSG as ‘‘Class $\xi_{G_{xy}} \bar{\phi}_{\sigma_{xy}}$ ’’, where $\bar{\phi}_{\sigma_{xy}} = p_{\sigma_{xy}} \pi$. The flux patterns of all the U(1) *Ansätze* are depicted in Fig. 9.

The class U1 yields four distinct *Ansätze* labeled as U100, U1 π 0, U10 π , and U1 π π . Notably, for U10 π , the mean-field amplitudes on the diagonal bonds vanish due to symmetry, and a uniform π -flux threads all the plaquettes, corresponding to a QSL with an SU(2) IGG realized on the square lattice [56].

Next, the four *Ansätze*, labeled as U300, U3 π 0, U30 π , and U3 π π , belong to the class U3. The symmetry-allowed mean fields for U30 π and U3 π π are identical to those of U10 π and U1 π π , respectively. However, the U3 class has a staggered chemical potential, whereas the chemical potential is uniform for the U1 class. Both the U1 and U3 classes of *Ansätze* consist of real hopping terms only.

Additionally, we identify a few more classes of U(1) *Ansätze*, labeled as U500, U50 π , U600, U60 π , and U8 $\xi\rho$. In these cases, the mean-field amplitudes vanish on the diagonal bonds, as does the onsite potential, while the square bonds include both real and imaginary hopping terms. Note that for the U5 class *Ansätze*, a nontrivial

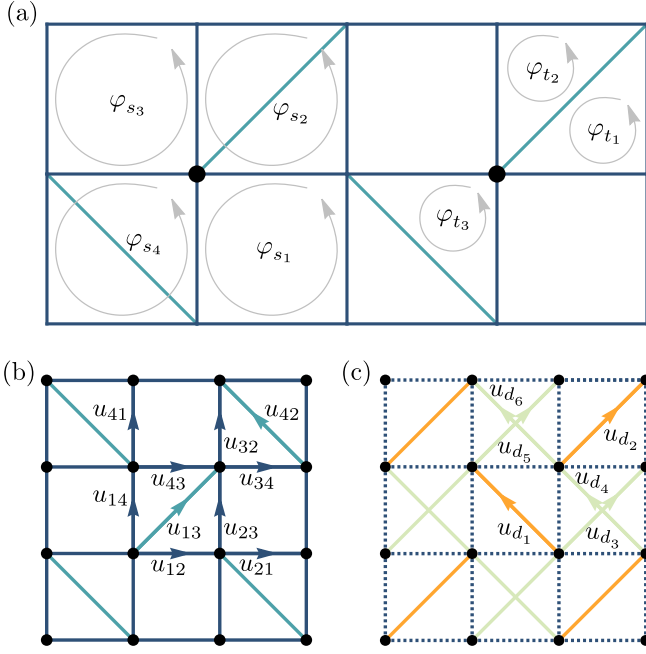


FIG. 8. (a) Illustration of the different SU(2) fluxes which characterize the U(1) *Ansätze*, defined with respect to a “base site” denoted by a black circle. The two such circles shown here are, in fact, equivalent. (b) Definition of mean-field amplitudes on the links of the Shastry-Sutherland lattice within a unit cell, and (c) the labeling convention for the additional diagonal bonds.

flux, i.e., $\neq 0, \pi$ threads the empty squares of the Shastry-Sutherland lattice, while for the U6 class a nontrivial flux threads those squares of the Shastry-Sutherland lattice which would have otherwise featured a diagonal bond. Up to NN bonds, these two classes of *Ansätze* are equivalent.

The U8 ξ 0 class (with $\xi \equiv \xi_{G_{xy}}$), in particular, incorporates a series of mean-field *Ansätze*. The explicit structure of the mean-field amplitudes in this case is given by:

$$\begin{aligned} u_s &= i\chi_s^0\tau^0 + \chi_s^3\tau^z = u_{12} = -u_{14}^\dagger = -u_{23} \\ &= u_{43}^\dagger = -u_{21}^\dagger = u_{41} = F_3(\xi)u_{32}^\dagger = -F_3(\xi)u_{34}. \end{aligned} \quad (32)$$

The bonds u_{41} and u_{32} are modified under a translation T_x , while all other bonds remain invariant:

$$\begin{aligned} u_{41}(x, y) &= u_{(m,n,4),(m,n+1,1)} = F_3(2n\xi)u_{41}, \\ u_{32}(x, y) &= u_{(m,n,3),(m,n+1,2)} = F_3(2n\xi)u_{32}. \end{aligned} \quad (33)$$

To realize such an *Ansatz* on a finite lattice, one must impose the constraint

$$\xi = \xi_{G_{xy}} = \frac{\mathcal{P}}{\mathcal{Q}}\pi, \quad \text{with } \mathcal{P}, \mathcal{Q} \in \mathbb{Z}. \quad (34)$$

Thus, for each choice $\mathcal{P}/\mathcal{Q} \in (0, 1)$, Eq. (34) provides a realization of at least one fully symmetric mean-field

Label	u_s	u_d	Onsite	Parent U(1)
Z2000	$\tau^{z,x}$	$\tau^{z,x}$	τ^z	U100, U300
Z2100	$\tau^{z,x}$	$\tau^{z,x}$	τ^z	U1 π 0, U3 π 0
Z2001	$\tau^{0,y}$	$\tau^{z,x}$	τ^z	U100, U300, U500
Z2101	$\tau^{0,y}$	$\tau^{z,x}$	τ^z	U1 π 0, U3 π 0
Z2011	$\tau^{0,y}$	0	τ^z	U10 π , U30 π , U50 π
Z2111	$\tau^{0,y}$	0	τ^z	U1 π π , U3 π π
Z3000	$\tau^{x,z}$	τ^z	τ^z	U100, U300, U800
Z3100	$\tau^{x,z}$	τ^z	τ^z	U1 π 0, U3 π 0, U8 π 0
Z3010	$\tau^{x,z}$	0	τ^z	U10 π , U30 π , U800
Z3110	$\tau^{x,z}$	0	τ^z	U1 π π , U3 π π , U8 π π
Z3001	$\tau^{0,y}$	τ^z	τ^z	U100, U300, U600
Z3101	$\tau^{0,y}$	τ^z	τ^z	U1 π 0, U3 π 0
Z3011	$\tau^{0,y}$	0	τ^z	U10 π , U30 π , U60 π
Z3111	$\tau^{0,y}$	0	τ^z	U1 π π , U3 π π
Z5001	$\tau^{0,x,z}$	0	0	U500, U600, U800
Z5101	$\tau^{0,x,z}$	0	0	U8 π 0
Z5011	$\tau^{0,x,z}$	0	0	U50 π , U60 π , U800
Z5111	$\tau^{0,x,z}$	0	0	U8 π 0

TABLE IV. Mean-field parameters on the reference bonds, u_s and u_d , for all possible symmetric \mathbb{Z}_2 *Ansätze* on the Shastry-Sutherland lattice.

QSL within this PSG class, and in total, there exist an infinite number of such QSLs [56].

Lastly, we note that U(1) *Ansätze* in classes U2, U4, and U7 cannot be realized with up to only NNN bonds.

B. \mathbb{Z}_2 *Ansätze* on the Shastry-Sutherland lattice

Although there exist a total of 64 projective extensions of the symmetry group with IGG \mathbb{Z}_2 , only 18 of these can be realized when restricting the *Ansätze* to NNN mean-field amplitudes. The symmetric \mathbb{Z}_2 *Ansätze* have the following structure:

$$u_s = i\chi_s^0\tau^0 + \Delta_s^1\tau^x + \Delta_s^2\tau^y + \chi_s^3\tau^z, \quad (35)$$

$$u_{12} = \eta_\sigma u_{43}^\dagger = \eta_{G_x T_x} u_{21} = \eta_{G_x T_x} \eta_\sigma \eta_{G_{xy}} u_{34}^\dagger = u_s, \quad (36)$$

$$u_{14} = u_{23}^\dagger = \eta_{G_x T_x} u_{41} = \eta_{G_x T_x} \eta_{G_{xy}} u_{32}^\dagger = (\tau^z)^p u_s (\tau^z)^p, \quad (37)$$

$$u_{13} = u_{42} = u_d = i\chi_d^0\tau^0 + \Delta_d^1\tau^x + \Delta_d^2\tau^y + \chi_d^3\tau^z, \quad (38)$$

$$a_\gamma(i)\tau^\gamma = a_1\tau^x + a_2\tau^y + a_3\tau^z; \quad (39)$$

here, $p \equiv 0(1)$ for $\mathcal{W}_{\sigma_{xy}, u} \propto \tau^{0(3)}$. In the equations above, the sign parameter $\eta_{G_x T_x}$ is irrelevant because up to NNNs, *Ansätze* with positive and negative $\eta_{G_x T_x}$ are related by a gauge transformation.

We label the *Ansätze* using the scheme

$$\mathbb{Z} \text{ PSG}_{\text{row}} \left(\frac{1 - \eta_{G_{xy}}}{2} \right) \left(\frac{1 - \eta_\sigma}{2} \right) \left(\frac{1 - \eta_{G_x T_x}}{2} \right), \quad (40)$$

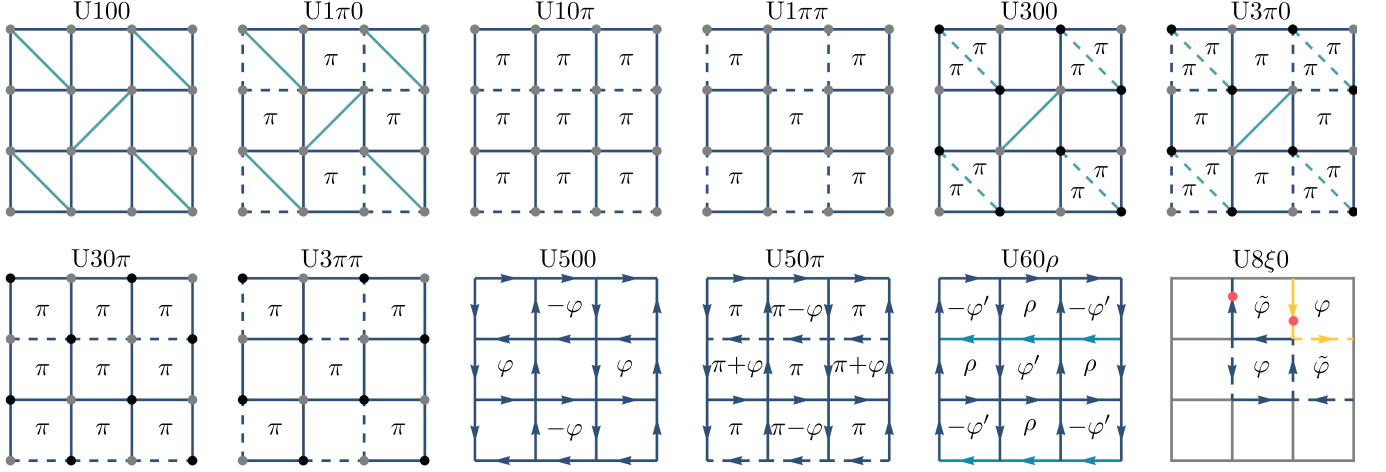


FIG. 9. Sign structure and flux patterns for all U(1) *Ansätze*. Gray (black) dots on the lattice sites denote positive (negative) signs of the onsite chemical potential. The solid (dashed) lines represent an overall positive (negative) signs of the hoppings. Among these *Ansätze*, the ones in the U1 and U3 classes consist of only real hoppings; the U5, U6, and U8 classes feature complex hoppings, so we label the directions of the link fields u_{ij} by arrows. The link fields on dark-blue bonds are defined as $u_s = i\chi_s^0\tau^0 + \chi_s^3\tau^z$. On the light-blue (in U60 ρ) and orange (in U8 ξ_0) bonds, the link fields are given by $F_3(\rho = p_{\sigma_{xy}}\pi)u_s$ and $F_3(\xi = \xi_{G_{xy}})u_s$, respectively, where $F_3(\lambda) \equiv \exp(i\lambda\tau^z)$. For plaquettes with nonzero fluxes, we note the corresponding flux values $\varphi = \text{Arg}[u_s^4]$, $\varphi' = \phi + \text{Arg}[\rho] = \phi + \text{Arg}[p_{\sigma_{xy}}\pi]$, and $\tilde{\varphi} = -\varphi + \xi = -\varphi + \xi_{G_{xy}}$, where $\xi_{G_{xy}} = \mathcal{P}\pi/\mathcal{Q}$, for $\mathcal{P}, \mathcal{Q} \in \mathbb{Z}$. In the U8 ξ_0 *Ansatz*, the two vertical bonds marked by a red dot are modified by a 2×2 U(1) matrix—specified in Eq. (33)—under translations along \hat{x} , while all other bonds are translation invariant.

where PSG_{row} corresponds to the row number in Table III.

Upon restricting ourselves to only J_s and J_d bonds, a total of 18 different symmetric *Ansätze* with IGG \mathbb{Z}_2 can be realized—these are listed in Table IV. They are also graphically represented in Fig. 10(a), omitting the parameter $\eta_{G_x T_x}$ for simplicity. However, this parameter does become important when establishing a connection of our PSGs with those on the square lattice, as discussed in the following section.

C. Mapping to square-lattice \mathbb{Z}_2 *Ansätze*

In this section, we show how the \mathbb{Z}_2 QSL *Ansätze* on the Shastry-Sutherland lattice can be continuously connected to \mathbb{Z}_2 *Ansätze* realizable on the square lattice [56].

The square lattice has a higher symmetry than the Shastry-Sutherland. The wallpaper group of the square lattice is $p4m$, which is generated by two translations $T_1 = a\hat{x}$, $T_2 = a\hat{y}$, and three reflections σ_{xy} , σ_x , and σ_y about the $x = y$, $y = 0$, and $x = 0$ lines, respectively. As we show here, including σ_x transforms the wallpaper group $p4g$ of the Shastry-Sutherland lattice into $p4m$. The reflection σ_x transforms the coordinate (x, y) to $(x, -y)$ and acts on (m, n, u) as

$$\sigma_x : (m, n, u) \rightarrow (m, -n - \delta_{u,3/4}, u). \quad (41)$$

One can verify that the other generators of the square

lattice can be obtained as follows:

$$\begin{aligned} T_1 &= G_x \sigma_x, \\ T_2 &= \sigma_{xy} G_x \sigma_x \sigma_{xy} = \sigma_{xy} T_1 \sigma_{xy}, \\ \sigma_y &= \sigma_{xy} \sigma_x \sigma_{xy}. \end{aligned} \quad (42)$$

Hence, the wallpaper group $p4m$ is generated by $\{G_x, \sigma_{xy}, \sigma_x\}$. Using this symmetry group, we establish a mapping from the Shastry-Sutherland lattice PSGs to the square-lattice PSGs in Appendix E. We find that upon including σ_x , the *Ansätze* belonging to the $\eta_{G_{xy}} = -1$ class have to be excluded as we are incorporating a larger set of symmetries. Note that this class is also the one which yields $(0, \pi, 0, \pi)$ - and $(\pi, 0, \pi, 0)$ -flux phases in the Shastry-Sutherland lattice, while such staggered-flux phases are forbidden on the square lattice [56]. All things considered, we arrive at the 272 PSGs found in Ref. [56].

Next, we discuss how the \mathbb{Z}_2 *Ansätze* in the class $\eta_{G_{xy}} = +1$ can be mapped to those on the square lattice. To do so, we first implement the geometric mapping between the two lattices as illustrated in Fig. 1(c). Beginning with the Shastry-Sutherland lattice, we have to include two additional symmetry-inequivalent diagonal interactions, denoted by orange and light green bonds (with coupling strengths J'_d and J_{\square}), respectively. This introduces six new mean-field amplitudes u_{d_1}, \dots, u_{d_6} , as shown in Fig. 8(c). The full *Ansatz* can, in fact, be defined in terms of four fields: u_s , on the NN square bonds; u_d , on the diagonal bonds already present on the Shastry-Sutherland lattice; $u_{d'}$, on the other diagonal bonds in the same set of plaquettes as u_d ; and u_{\square} , on both the

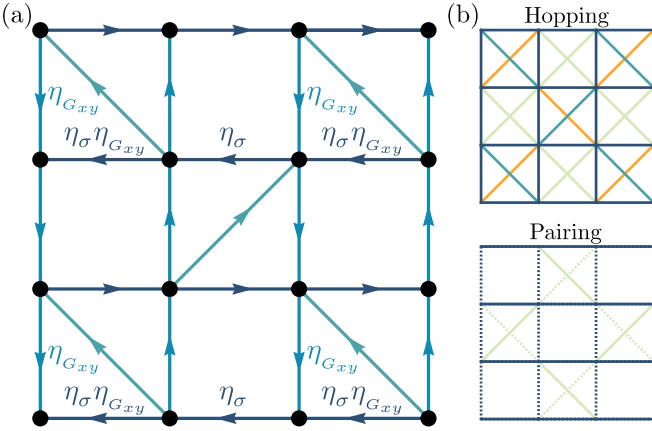


FIG. 10. (a) Graphical representation of \mathbb{Z}_2 *Ansätze*. Here, the link fields on the dark-blue (horizontal) bonds are u_s , and the link fields \tilde{u}_s on the light-blue (vertical) bonds are related to u_s as $\tilde{u}_s = (\tau^z)^p u_s (\tau^z)^p$, where $p=0(1)$ for $\mathcal{W}_{\sigma_{xy},u} \propto \tau^{0(z)}$. The teal (diagonal) bonds carry a link field u_d . All the *Ansätze* are translationally invariant. (b) Structure of the QSL *Ansatz* Z3000. The top figure conveys the signs of the hopping fields with the hopping amplitudes on the blue, teal, orange, and green bonds given by $\chi_s, \chi_d, \chi_{d'}$, and χ_\square , respectively. The bottom figure shows the sign structure of the pairing field, which has d -wave symmetry, and the pairing amplitudes on the blue and green bonds are given by Δ_s and Δ_\square , respectively. Dashed bonds denote a negative sign for the pairing.

diagonal bonds in the empty Shastry-Sutherland plaquettes. The structure of the \mathbb{Z}_2 *Ansätze* with $p4g$ symmetry on these reference bonds are then given by

$$u_{d'} = u_{d_1} = u_{d_2} = i\chi_{d'}^0 \tau^0 + \Delta_{d'}^1 \tau^x + \Delta_{d'}^2 \tau^y + \chi_{d'}^3 \tau^z, \quad (43)$$

$$u_\square = u_{d_3} = (\tau^z)^p u_{d_4} (\tau^z)^p = (\tau^z)^p u_{d_5} (\tau^z)^p = u_{d_6}, \quad (44)$$

where

$$u_\square \equiv i\chi_\square^0 \tau^0 + \Delta_\square^1 \tau^x + \Delta_\square^2 \tau^y + \chi_\square^3 \tau^z. \quad (45)$$

The mean-field parameters $u_s, u_d, u_{d'}$, and u_\square are listed in Table V. Note, that due to the inclusion of *all* diagonal bonds, the different signs of $\eta_{G_x T_x}$ are no longer related by gauge transformations.

In general, $u_d, u_{d'}$, and u_\square are not related by symmetry. However, in the square-lattice limit (after including σ_x), i.e., $J_d = J_{d'} = J_\square$, all diagonal bonds do become symmetry equivalent. This allows us to construct \mathbb{Z}_2 *Ansätze* on the square lattice starting from the ones on the Shastry-Sutherland lattice. For example, consider the *Ansatz* labeled Z3000 and PSG 3(c) with $\eta_{G_x T_x} = -\eta_{\sigma_x G_x} = +1$ in Table XII. After imposing the constraints associated with σ_x , we obtain the following *Ansatz*:

$$u_{12} = u_{21} = u_{43} = u_{34} = \chi_s \tau^z + \Delta_s \tau^x, \quad (46a)$$

$$u_{14} = u_{41} = u_{23} = u_{32} = \chi_s \tau^z - \Delta_s \tau^x, \quad (46b)$$

Label	u_s	u_d	$u_{d'}$	u_\square	Onsite
Z2000	$\tau^{z,x}$	$\tau^{z,x}$	$\tau^{z,x}$	$\tau^{z,x}$	τ^z
Z2100	$\tau^{z,x}$	$\tau^{z,x}$	$\tau^{z,x}$	0	τ^z
Z2001	$\tau^{0,y}$	$\tau^{z,x}$	$\tau^{z,x}$	$\tau^{z,x}$	τ^z
Z2101	$\tau^{0,y}$	$\tau^{z,x}$	$\tau^{z,x}$	0	τ^z
Z2011	$\tau^{0,y}$	0	0	0	τ^z
Z2111	$\tau^{0,y}$	0	0	$\tau^{z,x}$	τ^z
Z3000	$\tau^{x,z}$	τ^z	τ^z	$\tau^{z,x}$	τ^z
Z3100	$\tau^{x,z}$	τ^z	τ^z	0	τ^z
Z3010	$\tau^{x,z}$	0	0	0	τ^z
Z3110	$\tau^{x,z}$	0	0	$\tau^{z,x}$	τ^z
Z3001	$\tau^{0,y}$	τ^z	τ^z	$\tau^{z,x}$	τ^z
Z3101	$\tau^{0,y}$	τ^z	τ^z	0	τ^z
Z3011	$\tau^{0,y}$	0	0	0	τ^z
Z3111	$\tau^{0,y}$	0	0	$\tau^{z,x}$	τ^z
Z5001	$\tau^{0,x,z}$	0	0	0	0
Z5101	$\tau^{0,x,z}$	0	0	0	0
Z5011	$\tau^{0,x,z}$	0	0	0	0
Z5111	$\tau^{0,x,z}$	0	0	0	0

TABLE V. Extension of all the symmetric \mathbb{Z}_2 *Ansätze* listed in Table IV to the other diagonals—that were not originally included in the Shastry-Sutherland lattice—on which the reference bonds are denoted as $u_{d'}$ and u_\square [see Eqs. (43)–(45)]. Here, $u_{d'}$ corresponds to the diagonal bonds in the same set of plaquettes as u_d , and u_\square represents the diagonal bonds in the empty Shastry-Sutherland plaquettes.

$$u_{13} = u_{42} = u_{d_1} = u_{d_2} = \chi_d \tau^z, \quad a_\gamma(u) = 0, \quad (46c)$$

$$u_{d_3} = u_{d_4} = u_{d_5} = u_{d_6} = -\chi_d \tau^z. \quad (46d)$$

It is straightforward to see that after a gauge transformation $W(m, n, u) = \{i\tau^y, -1, -i\tau^y, 1\}$, this can be re-expressed as:

$$u_{12} = u_{21} = u_{43} = u_{34} = \chi_s \tau^z - \Delta_s \tau^x, \quad (47a)$$

$$u_{14} = u_{41} = u_{23} = u_{32} = \chi_s \tau^z + \Delta_s \tau^x, \quad (47b)$$

$$u_{13} = u_{d_2} = u_{d_3} = u_{d_5} = \chi_d \tau^z, \quad a_\gamma(u) = 0, \quad (47c)$$

$$u_{42} = u_{d_1} = u_{d_4} = u_{d_6} = -\chi_d \tau^z. \quad (47d)$$

In the canonical square-lattice Cartesian notation, it can be written as

$$u_{\hat{x}} = \chi_s \tau^z - \Delta_s \tau^x, \quad u_{\hat{y}} = \chi_s \tau^z + \Delta_s \tau^x, \quad (48a)$$

$$u_{-\hat{x}+\hat{y}} = \chi_d \tau^z, \quad u_{-\hat{x}-\hat{y}} = -\chi_d \tau^z, \quad a_\gamma(u) = 0. \quad (48b)$$

This corresponds to the Z2Azz13 *Ansatz* in the PSG classification by Wen [56]. Thus, the \mathbb{Z}_2 *Ansatz* Z3000 on the Shastry-Sutherland lattice can be continuously connected to the \mathbb{Z}_2 *Ansatz* Z2Azz13 on the square lattice. This connection is protected by the projective realization of G_x and σ_{xy} . When considering up to NNN amplitudes, among the \mathbb{Z}_2 *Ansätze* listed in this work, five more can be realized with IGG \mathbb{Z}_2 , which are labeled Z2A0013, Z2B0013, Z2Axx0z, Z2Ax2(12)n, and

\mathbb{Z}_2 Ansatz ($p4g$)	PSG	$(\eta_{G_x T_x}, \eta_{\sigma_x G_x})$	\mathbb{Z}_2 Ansatz ($p4m$)
Z3000	3a	(+, +)	Z2A0013
Z3000	3c	(+, -)	Z2Azz13
Z3010	3a	(+, +)	Z2B0013
Z2000	2b	(+, -)	Z2Axx0z
Z5011	5d	(-, +)	Z2Ax2(12)n
Z5001	5d	(-, +)	Z2Bx2(12)n

TABLE VI. Mapping between the $p4g$ -symmetric \mathbb{Z}_2 Ansätze (left column) and $p4m$ -symmetric \mathbb{Z}_2 Ansätze (right column). The second and third columns tabulate the PSG parameters (see Appendix E) that make the connection between the two sets of Ansätze.

$Z2Bx2(12)n$. Their connections to the square lattice can be established following a procedure similar to that carried out above for the $Z2Azz13$ Ansatz, as summarized in Table VI.

V. NUMERICAL RESULTS

A. \mathbb{Z}_2 Dirac state: Mean-field properties

Given that the gapless Z3000 state serves as the most promising candidate to describe the QSL in the generalized SSM (as we will show below), we now describe its corresponding variational wavefunction in terms of Abrikosov pseudo-fermions [87]. First, we define a mean-field state in the fermionic Hilbert space by taking the ground state $|\phi_{\text{MF}}\rangle$ of the following noninteracting spinon Hamiltonian, which is of the generalized Bardeen-Cooper-Schrieffer form:

$$\begin{aligned}
\hat{H}_{\text{MF}}^{\text{Z3000}} = & \chi_d \sum_{\langle ij \rangle_{\text{teal}}, \alpha} s_{ij}^d \hat{f}_{i,\alpha}^\dagger \hat{f}_{j,\alpha} + \chi_{d'} \sum_{\langle ij \rangle_{\text{orange}}, \alpha} s_{ij}^{d'} \hat{f}_{i,\alpha}^\dagger \hat{f}_{j,\alpha} \\
& + \sum_{\langle ij \rangle_{\text{blue}}} \left[\chi_s \sum_{\alpha} s_{ij}^s \hat{f}_{i,\alpha}^\dagger \hat{f}_{j,\alpha} + \Delta_s \nu_{ij}^s (\hat{f}_{i,\uparrow}^\dagger \hat{f}_{j,\downarrow} + \text{h.c.}) \right] \\
& + \sum_{\langle ij \rangle_{\text{green}}} \left[\chi_{\square} \sum_{\alpha} s_{ij}^{\square} \hat{f}_{i,\alpha}^\dagger \hat{f}_{j,\alpha} + \Delta_{\square} \nu_{ij}^{\square} (\hat{f}_{i,\uparrow}^\dagger \hat{f}_{j,\downarrow} + \text{h.c.}) \right] \\
& + \mu \sum_{i,\alpha} \hat{f}_{i,\alpha}^\dagger \hat{f}_{i,\alpha}. \tag{49}
\end{aligned}$$

Here, s_{ij} and ν_{ij} are sign factors for hoppings and pairings, respectively, which take values $+1(-1)$ for bonds marked as solid (dashed) in Figs. 10(b) and (c). The different colors in Fig. 10(b) label the symmetry-inequivalent bonds, as referenced in Eq. (49). We fix $\chi_s = 1$ as the overall energy scale, and the resulting wavefunction is thus parametrized by six variational parameters: χ_d , $\chi_{d'}$, χ_{\square} , Δ_s , Δ_{\square} , and the onsite chemical potential, μ .

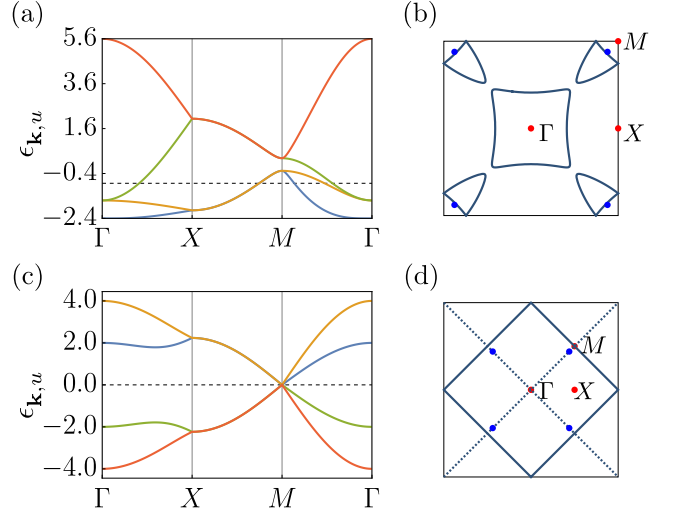


FIG. 11. (a) Dispersion of the parent U100 state and (b) illustration of its Fermi surfaces. The parameters here are chosen to be the VMC-optimized parameters at $J_s/J_d = 0.80$ on a 14×14 cluster, given by $\chi_s = 1.0$, $\chi_d = 0.53$, $\chi_{d'} = 0.13$, and $\chi_{\square} = 0.47$. The dashed line in the band structure marks the Fermi level. The blue dots in (b) are the VMC optimized location of Dirac nodes of the Z3000 state. (c) The dispersion of another parent state of Z3000—namely, U800—in the gauge with uniform hopping $\chi_s = 1.0$ and a $d_{x^2-y^2}$ pairing which is set to $\Delta_s = 0.5$. In (d), solid and dashed lines indicate the zero-energy contours of χ_s and the nodal lines of Δ_s (d -wave pairing) terms, respectively. The crossings at $M(\pm\pi/2, \pm\pi/2)$ give the positions of the Dirac nodes. The blue dots indicate the locations of the Dirac nodes in the Z3000 state resulting from Δ_{\square} pairing and remaining hopping amplitudes.

Although the Z3000 Ansatz can be obtained by lowering the U(1) IGG—via singlet pairing terms—of three distinct U(1) states, namely, U100, U300, and U800 in Table IV, it is most straightforward to view it as a descendant of the parent U100 state (see also App. H). Indeed, due to the linear (nonprojective) realization of symmetries in the U100 state, it allows for uniform real hopping amplitudes on *all* diagonal and square-lattice bonds. Thus, it can be retrieved from the Z3000 Ansatz (49) by setting the pairings $\Delta_s = \Delta_{\square} = 0$. The band structure of the parent U100 state is shown in Fig. 11(a) and at half filling, it features a Fermi surface [Fig. 11(b)]. On adding a nonzero Δ_s , the nearly square-shaped Fermi surface surrounding the Γ point is completely lifted, and the other Fermi surfaces in the vicinity of the M points shrink to isolated points, forming Dirac cones at $M(\pi/2, \pi/2) + (\pm\varepsilon, \pm\varepsilon)$. The Dirac points always reside on the line ΓM . This is illustrated in Fig. 30 [App. F], where we show the contour plot of the energies of the lowest eigenmode of Z3000 in the k_x-k_y plane. The dependence of the magnitude of ε on all the variational parameters is illustrated in Fig. 31 [App. F]. In Fig. 12(a), we plot the dispersion of the Z3000 state for the VMC-optimized parameters at $J_s/J_d = 0.8$ while the four Dirac

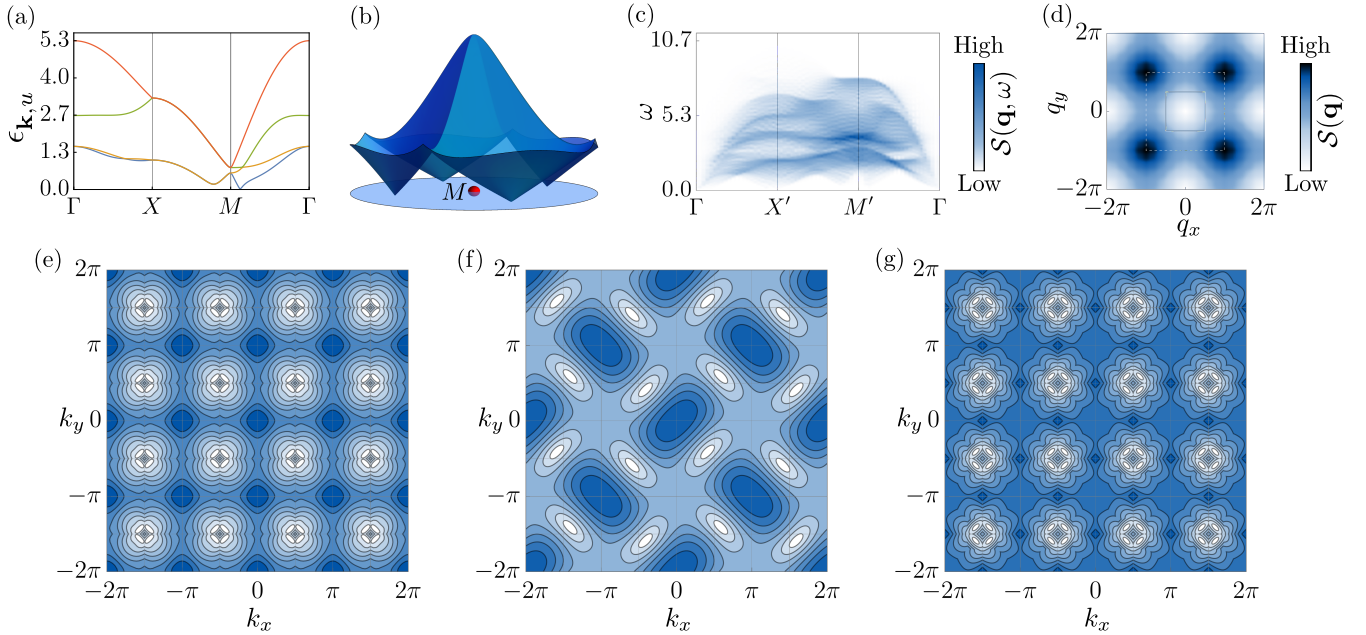


FIG. 12. (a) Spinon band structure of the Z3000 state for the variationally optimized parameters at $J_s/J_d = 0.80$, given by $\chi_s = 1.0$, $\chi_d = 0.46$, $\chi_{d'} = -0.09$, $\chi_\square = 0.14$, $\Delta_s = 0.39$, $\Delta_\square = 0.38$, and $\mu = 0.35$. (b) Spinon dispersion of the optimized Z3000 state, showing the four Dirac cones residing at $M(\pi/2, \pi/2) + (\pm\varepsilon, \pm\varepsilon)$. (c) Dynamical spin structure factor, and (d) equal-time spin structure factor of this state. The solid and dashed squares denote the first Brillouin zone (FBZ) and the extended Brillouin zone (EBZ), respectively. The lower panel demonstrates the equivalence of the Dirac dispersion in Z3000 and Z2Azz13. (e) Contour plot of the lowest eigenenergy for Z3000, yielding the positions of the Dirac points which are located at $(\pm\pi/2 \pm \varepsilon, \pm\pi/2 \pm \varepsilon)$. (f) The same for Z2Azz13, where one can identify the Dirac cones at $\pm(\pi/2 + \varepsilon, \pi/2 + \varepsilon)$ and $\pm(-\pi/2 + \varepsilon, \pi/2 - \varepsilon)$ which lead to C_4 symmetry around $(\pi, 0)$ and $(0, \pi)$, and C_2 symmetry around $(0, 0)$. The correspondence between the Dirac dispersions in Z3000 and Z2Azz13 is manifest upon adopting a gauge for Z2Azz13 with an enlarged (2×2) unit cell (g). Note that the back-folding of the Brillouin zone leads to the similar splitting of Dirac cones around $(\pm\pi/2, \pm\pi/2)$. The color scheme is same as that in panel (c).

cones surrounding the M point are shown in Fig. 12(b). We also present the spin correlations of this mean-field state, as reflected in its dynamical and equal-time spin structure factors, in Figs. 12(c) and (d), respectively.

It is worthwhile to discuss the splitting of the Dirac nodes in the Z3000 *Ansatz*, particularly in comparison with those in the Z2Azz13 state on the square lattice [56]. When one considers only uniform hopping χ_s and $d_{x^2-y^2}$ pairing Δ_s on the nearest-neighbor bonds³, both the square and Shastry–Sutherland lattices exhibit Dirac nodes at the commensurate momenta $M(\pm\pi/2, \pm\pi/2)$ [see Figs. 11(c) and 11(d)]. However, the inclusion of any additional mean-field parameter χ_d , $\chi_{d'}$, χ_\square , Δ_\square , or μ in the Z3000 *Ansatz* splits the Dirac node at each M point into four nodes residing at incommensurate momenta $(\pm\pi/2 \pm \varepsilon, \pm\pi/2 \pm \varepsilon)$, with the nodes always located along ΓM [marked by blue dots in Fig. 11(d)]. Thus, the Z3000 state can also be viewed as descending from the U800 *Ansatz*. We illustrate this behavior

using a contour plot of the lowest-energy eigenmode of the Z3000 state, shown in Fig. 12(e).

A similar phenomenon occurs in the square-lattice Z2Azz13 state: including additional mean-field amplitudes corresponding to d_{xy} pairings on the diagonals of the squares shifts the Dirac nodes from $(\pm\pi/2, \pm\pi/2)$ to $\pm(\pi/2 + \varepsilon, \pi/2 + \varepsilon)$ and $\pm(-\pi/2 + \varepsilon, \pi/2 - \varepsilon)$, as shown in Fig. 12(f). In this case, the band structure exhibits C_4 symmetry about $(\pi, 0)$ and $(0, \pi)$, and C_2 symmetry about $(0, 0)$. Therefore, although the Z3000 and Z2Azz13 *Ansätze* are adiabatically connected, the equivalence of their band structures is not immediately apparent. The origin of this difference lies in the gauge structure: the Z2Azz13 *Ansatz* in Ref. [56] is defined in the geometrical unit cell, whereas the Z3000 *Ansatz* is realized in a 2×2 unit cell. To facilitate a direct comparison, we redefine the Z2Azz13 *Ansatz* in a 2×2 unit cell and back-fold the Brillouin zone accordingly. This procedure leads to an identical splitting of Dirac nodes in the spinon dispersion of the lowest eigenmode [see Fig. 12(g)], as observed for the Z3000 state. Consequently, one expects the gapless points in the spin excitations to appear at $(\pi \pm \delta, \pi \pm \delta)$ (where $\delta = 2\varepsilon$), as well as at $(\pi, \pm\delta)$ and $(\pm\delta, \pi)$, consistent with the two-

³ One can additionally include pairing on the fourth-nearest-neighbor bonds (which are twice the nearest neighbor), i.e., connecting $(0, 0)$ to $(\pm 2, 0)$ and $(0, \pm 2)$.

spinon excitation spectra of the Z2Azz13 state reported in Ref. [56]. Signatures of these gapless excitations are already visible in the mean-field dynamical structure factor shown in Fig. 12(c). They become more pronounced beyond the mean-field level upon including gauge fluctuations, as will be demonstrated in the dynamical structure factor obtained from Keldysh pf-FRG.

It is also instructive to compare these results with previous studies of the Z2Azz13 state on the square lattice, which has been proposed as a candidate QSL ground state of the J_1 - J_2 model in Refs. [48, 49]. In those works, a modified version of the Z2Azz13 *Ansatz* is adopted compared to the original proposal in Ref. [56] in order to realize the \mathbb{Z}_2 gauge structure. Specifically, the d_{xy} pairing is defined on bonds connecting $(0, 0)$ to $(\pm 2, \pm 2)$ —which are twice the length of the diagonals inside the squares, corresponding to the fifth-nearest-neighbor bonds—instead of the bonds connecting $(0, 0)$ to $(\pm 1, \pm 1)$, i.e., the diagonals inside the squares as originally considered in Ref. [56]. Restricting the d_{xy} singlet pairing amplitudes to the $(\pm 2, \pm 2)$ bonds ensures that the Dirac points remain located at the commensurate momenta $(\pm\pi/2, \pm\pi/2)$ in the mean-field spectrum. As a consequence, the two-spinon excitation spectrum contains gapless excitations at (π, π) , $(\pi, 0)$, and $(0, \pi)$, rather than at the incommensurate points $(\pi \pm \delta, \pi \pm \delta)$, $(\pi, \pm\delta)$, and $(\pm\delta, \pi)$ that would arise if the d_{xy} pairings were defined on the $(\pm 1, \pm 1)$ bonds (see Ref. [56]).

On the Shastry–Sutherland lattice, however, we find that it is not possible to define the Z2Azz13 *Ansatz* in an analogous gauge that preserves the Dirac points at $(\pm\pi/2, \pm\pi/2)$. Indeed, even when the singlet pairing Δ_{\square} is restricted to the $(\pm 2, \pm 2)$ diagonals of the empty squares—rather than the $(\pm 1, \pm 1)$ diagonals—each Dirac point at $(\pm\pi/2, \pm\pi/2)$ still splits into four nodes located at $(\pm\pi/2 \pm \varepsilon, \pm\pi/2 \pm \varepsilon)$. As a result, the gapless points in the spin excitation spectrum appear at the same incommensurate momenta $(\pi \pm \delta, \pi \pm \delta)$, $(\pi, \pm\delta)$, and $(\pm\delta, \pi)$ as discussed in Ref. [56]. This behavior is corroborated by the dynamical spin structure factor obtained from both mean-field theory and Keldysh pf-FRG, shown in Figs. 12(a) and 19(a), respectively.

Therefore, in order to construct an *Ansatz* that naturally interpolates between the J_1 - J_2 square lattice and the Shastry–Sutherland lattice, we adopt the gauge structure of the Z2Azz13 state as defined in Ref. [56], with d_{xy} pairings on the $(\pm 1, \pm 1)$ diagonals. This choice leads to Dirac points and gapless spin excitations located at incommensurate momenta and, from an energetic standpoint, also yields the optimal energy for the corresponding Gutzwiller-projected wavefunction.

After performing a particle-hole transformation on the spinons with flavor \downarrow ,

$$\hat{f}_{i,\downarrow}^{\dagger} \rightarrow \hat{f}_{i,\downarrow}, \quad \hat{f}_{i,\uparrow}^{\dagger} \rightarrow \hat{f}_{i,\uparrow}^{\dagger}, \quad (50)$$

the mean-field Hamiltonian (49) commutes with the to-

tal number of particles. Thus, $|\phi_{\text{MF}}\rangle$ is defined by filling suitable single-particle orbitals. In this process, the choice of boundary conditions should be such that they lead to a unique state (by filling *all* orbitals in a shell with the same mean-field energy). Periodic (P) and antiperiodic (A) boundary conditions along the \mathbf{a}_1 and \mathbf{a}_2 lattice-vector directions [see Fig. 1(a)] can be considered, leading to four choices: [P,P], [P,A], [A,P], and [A,A]. Here, we impose antiperiodic and periodic boundary conditions along the \mathbf{a}_1 and \mathbf{a}_2 directions, respectively, i.e., [A,P], which leads to a closed shell (unique state) on $L \times L$ clusters with dimensions $L = 4\ell$ and $L = 4\ell + 2$, where ℓ is a positive integer.

B. Gutzwiller-projected *Ansatz*

A legitimate QSL wavefunction, residing in the correct sector with one fermion per site (corresponding to the physical Hilbert space of the spin-1/2 model), is then obtained by applying the Gutzwiller projector to the mean-field state $|\phi_{\text{MF}}\rangle$:

$$|\Psi_{\text{QSL}}\rangle = \mathcal{P}_{\text{G}}|\phi_{\text{MF}}\rangle, \quad (51)$$

where $\mathcal{P}_{\text{G}} = \prod_i (\hat{n}_{i,\uparrow} - \hat{n}_{i,\downarrow})^2$, $\hat{n}_{i,\alpha} = \hat{f}_{i,\alpha}^{\dagger} \hat{f}_{i,\alpha}$ being the fermionic density of flavor α on site i . The variational energy and correlation functions for $|\Psi_{\text{QSL}}\rangle$ can be computed in a straightforward fashion using Monte Carlo sampling, by virtue of which the constraint is imposed exactly [93]. Furthermore, a stochastic reconfiguration (SR) optimization enables us to obtain accurate estimates of the variational parameters contained in Eq. (49) with small statistical uncertainties [94, 95], even when a large number of parameters are involved [96–100].

A standard technique to systematically improve the accuracy of variational wavefunctions and approach the true ground state involves the application of a few Lánczos steps on a given variational state $|\Psi_{\text{QSL}}\rangle$ [101, 102]:

$$|\Psi_{p\text{-LS}}\rangle = \left(1 + \sum_{k=1}^p \lambda_k \hat{\mathcal{H}}^k \right) |\Psi_{\text{QSL}}\rangle, \quad (52)$$

where the λ_k s are variational parameters. For large enough p , $|\Psi_{p\text{-LS}}\rangle$ is guaranteed to converge to the exact ground state $|\Psi_{\text{ex}}\rangle$ provided the initial trial state $|\Psi_{\text{QSL}}\rangle$ is not orthogonal to $|\Psi_{\text{ex}}\rangle$, i.e., for $\langle \Psi_{\text{ex}} | \Psi_{\text{QSL}} \rangle \neq 0$. However, on large clusters, only a few Lánczos steps can be efficiently executed, and here, we consider the case with $p = 1$ and $p = 2$ ($p = 0$ corresponds to the initial trial wavefunction $|\Psi_{\text{QSL}}\rangle$). Based on this sequence, an estimate of the exact ground-state energy can be obtained by the method of zero-variance extrapolation. In fact, for sufficiently accurate states, $E - E_{\text{ex}} \approx \text{constant} \times \sigma^2$, where $E = \langle \hat{\mathcal{H}} \rangle / N$ and $\sigma^2 = (\langle \hat{\mathcal{H}}^2 \rangle - \langle \hat{\mathcal{H}} \rangle^2) / N$ are the

Label	Energy	BC
Z2000	-0.37500(1)	[P,A]
Z2100	-0.37500(1)	[A,P]
Z2001	-0.37500(1)	[A,A]
Z2101	-0.33509(5)	[A,A]
Z2011	-0.43440(1)	[P,A]
Z2111	-0.43452(5)	[A,P]
Z3000	-0.43728(1)	[A,P]
Z3100	-0.39336(1)	[A,A]
Z3010	-0.42129(1)	[A,A]
Z3110	-0.39340(1)	[A,A]
Z3001	-0.37973(1)	[A,P]
Z3101	-0.43529(2)	[A,A]
Z3011	-0.43436(1)	[P,A]
Z3111	-0.34089(3)	[A,A]
Z5001	-0.43321(1)	[A,A]
Z5101	-0.40872(1)	[A,A]
Z5011	-0.42974(1)	[A,A]
Z5111	-0.43493(1)	[A,A]

TABLE VII. Energies per site E/J_d of all symmetric \mathbb{Z}_2 *Ansätze* listed in Table V computed at $J_s/J_d = 0.80$ on a 14×14 cluster. The wavefunction includes all symmetry-allowed amplitudes on the $u_s, u_d, u_d', u_\square$ bonds and onsite terms. The boundary condition (BC) which gives the lowest energy is mentioned with, e.g., [A,P] indicating antiperiodic BC along the $\mathbf{a}_1 = (1, 0)$ direction and periodic BC along the $\mathbf{a}_2 = (0, 1)$ direction.

energy and variance per site, respectively. Thus, the exact ground-state energy E_{ex} can be extracted by fitting E vs σ^2 for $p = 0, 1$, and 2. The energy, its variance, and the correlation functions after the application of a few Lánczos steps are calculated using the standard variational Monte Carlo method.

L	Δ_s	Δ_\square	χ_d	χ_d'	χ_\square	μ
6	0.256(1)	0.085(1)	0.376(1)	+0.123(1)	0.181(1)	0.931(1)
8	0.355(1)	0.261(1)	0.386(1)	-0.034(2)	0.126(1)	0.605(1)
10	0.371(1)	0.320(1)	0.423(1)	-0.062(1)	0.131(1)	0.475(1)
12	0.381(2)	0.353(2)	0.446(1)	-0.076(2)	0.136(2)	0.399(2)
14	0.387(3)	0.381(2)	0.462(2)	-0.088(2)	0.139(2)	0.345(2)
20	0.400(2)	0.428(2)	0.490(2)	-0.110(2)	0.143(2)	0.254(3)
30	0.414(3)	0.465(2)	0.512(1)	-0.128(3)	0.147(2)	0.187(3)
40	0.422(3)	0.476(3)	0.522(3)	-0.136(3)	0.148(2)	0.155(4)
50	0.426(4)	0.480(4)	0.533(4)	-0.137(3)	0.153(4)	0.135(4)
60	0.425(4)	0.478(4)	0.533(4)	-0.138(4)	0.152(4)	0.126(5)

TABLE VIII. The singlet pairing and hopping amplitudes of the \mathbb{Z}_2 Dirac QSL (Z3000 state) on different cluster sizes obtained after VMC optimization for $J_s/J_d = 0.80$. The hopping on the square bonds χ_s is set to one.

C. Variational Monte Carlo

Our variational calculations are performed on $L \times L$ tori, which respect all symmetries of the $p4g$ wallpaper group, with periodic boundary conditions imposed on the spin Hamiltonian (1). We focus our analysis on the coupling ratio $J_s/J_d = 0.80$ which is located in the middle of the QSL regime seen in Refs. [32, 42, 43, 46], and for which the energy and correlation functions have been reported with different numerical approaches, thereby facilitating detailed comparisons.

1. Energetics

Among the *Ansätze* listed in Table VI, which can be continuously connected to the states on the square lattice, we find that the VMC optimization of the projected Z3000 *Ansatz* consistently yields the lowest variational energy on all clusters, with sizes ranging from $L = 6$ to 40, while the other *Ansätze* (including those which are not connected to the square lattice) have higher energies (see Table VII for energies of all \mathbb{Z}_2 *Ansätze*). For the optimized Z3000 state, crucially, we observe that the singlet pairing amplitudes Δ_s and Δ_\square converge to appreciable values across all cluster sizes, approaching their thermodynamic values (together with the remaining amplitudes) around a cluster size of $L = 50$ (refer to Table VIII). This provides strong evidence for a robust \mathbb{Z}_2 gauge structure in the thermodynamic limit. In particular, the Δ_\square pairing (responsible for the \mathbb{Z}_2 gauge structure) leads to an energy gain $(E_{\mathbb{Z}_2} - E_{U(1)})/E_{U(1)} \sim 0.01$ on top of the parent U(1) state (constructed from uniform χ_s and $d_{x^2-y^2}$ Δ_s amplitudes *only*). This is similar to the J_1 - J_2 square-lattice Heisenberg antiferromagnet where the energy gain of the Z2Azz13 state (due to d_{xy} singlet pairing terms on fifth-neighbor bonds⁴) is $\sim 1\%$ on top of the parent U(1) state (which shares the same parent U(1) state as the

L	0-LS	1-LS	2-LS	Extrapolation
6	-0.439512(1)	-0.448633(1)	-0.450432(1)	-0.451391(7)
8	-0.437955(1)	-0.446537(1)	-0.448619(1)	-0.449735(23)
10	-0.4375346(6)	-0.4454888(6)	-0.447838(3)	-0.449046(33)
12	-0.4373669(5)	-0.444746(1)	-0.447279(4)	-0.44929(21)
14	-0.4372820(6)	-0.444144(1)	-0.446776(4)	-0.44972(11)

TABLE IX. The energies per site E/J_d of the \mathbb{Z}_2 Dirac QSL (Z3000 state) with $p = 0, 1$, and 2 Lánczos steps, and the zero-variance extrapolation estimate on different cluster sizes as obtained by VMC, for $J_s/J_d = 0.80$.

⁴ On the Shastry-Sutherland lattice, a nonzero singlet pairing amplitude on fifth-neighboring bonds—connecting $(0, 0)$ to sites $(\pm 2, \pm 2)$ —does not give any detectable energy gain.

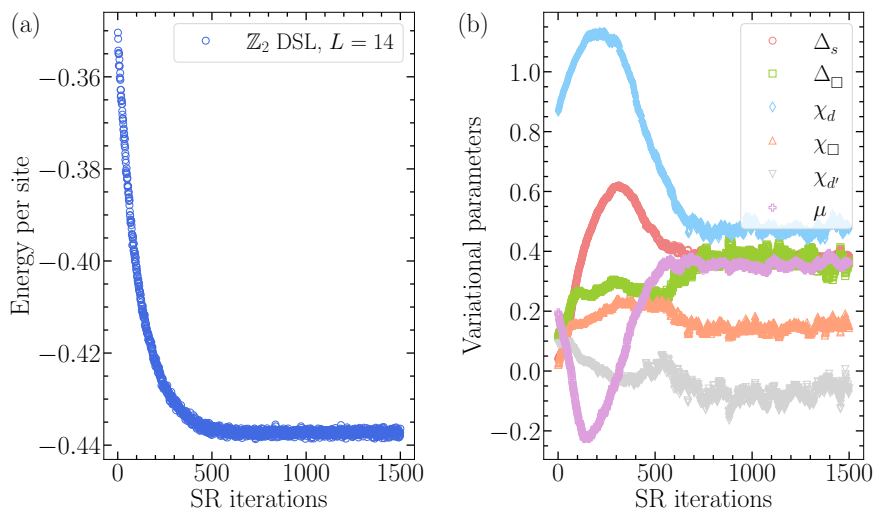


FIG. 13. A typical variational Monte Carlo optimization run for the Z3000 state on a 14×14 site cluster for $J_s/J_d = 0.80$. (a) Energy per site in units of J_d , and (b) variational parameters Δ_s , Δ_\square , χ_d , χ_\square , $\chi_{d'}$, and μ , as a function of the number of stochastic reconfiguration (SR) iterations. In (b), the initial parameters are taken to be $\Delta_s = 0.04$, $\Delta_\square = 0.11$, $\chi_d = 0.87$, $\chi_\square = 0.02$, $\chi_{d'} = 0.09$, $\mu = 0.2$, and we set $\chi_s = 1$ as the reference. The optimized parameter values presented in Table VIII are obtained by averaging over a much larger number of converged SR iterations than shown here. In comparison, the energy per site of the optimal parent U(1) state (defined by uniform χ_s and $d_{x^2-y^2}$ Δ_s pairing) is $E/J_d = -0.43321(1)$.

Z3000 *Ansatz* being likewise composed of uniform χ_s and $d_{x^2-y^2}$ Δ_s amplitudes *only*) [48]. In Fig. 13, we present a typical VMC optimization run showing the evolution of the energy and the parameters of the Z3000 state starting from a generic unbiased starting point. We verify the convergence by initiating many optimization runs with different random initial values, and found that the energy and variational parameters converge neatly to the same value (within error bars) after averaging over a sufficient number of Monte Carlo steps. It is important to note that while the energy converges after ~ 500 iterations, the parameters converge to their final values only after a much larger number of SR iterations (see Fig. 13). This is because in optimizing the former, the steepest-descent forces are calculated using correlated sampling instead of via energy differences [94, 103].

Having established that the Z3000 *Ansatz* represents

L	VMC	ViT	VMC + ViT	DMRG
6	-0.451391(7)	-0.451750	-0.451768(8)	-0.44565886
8	-0.449735(23)	-0.44995	-0.450013(27)	-0.44562053
10	-0.449046(33)	-0.449470	-0.449454(41)	-0.44609839
12	-0.44929(10)	-0.449352	-0.44933(11)	-0.44652433
14	-0.44972(11)	-0.449207	-0.44914(14)	-0.44680369
∞ *		-0.4486(2)	-0.4481(3)	-0.44837(30)

TABLE X. The ground-state energies of the spin-1/2 Heisenberg model at $J_s/J_d = 0.80$ for different cluster sizes, as obtained from zero-variance extrapolation. The extrapolation is performed using data on $L \times L$ tori from VMC, neural-network quantum states (ViT) [46], and combined extrapolation with both VMC and ViT energies (VMC + ViT); or from DMRG [42] on $2L \times L$ cylinders with periodic boundary conditions along the shorter direction. Our most accurate estimate of the ground-state energy on any given cluster is obtained from VMC + ViT extrapolation and is marked in bold. The exact-diagonalization (ED) value for $L = 6$ is -0.4517531 [46].

the lowest-energy variational wavefunction (within the class of Gutzwiller-projected fermionic states) for all the system sizes investigated—and that the singlet pairing amplitudes characterizing it as well as the resulting energy gains remain size-consistent—we consider it as our starting ($p = 0$) state and improve thereupon by applying Lánczos steps. At $J_s/J_d = 0.80$, the effect of two Lánczos steps for different cluster sizes is shown in Fig. 14 (see also Table IX for the actual values of the energies of the Z3000 state). To refine the accuracy of the extrapolation, we also include the smaller-variance ViT data from Ref. [46]. A zero-variance extrapolation is then performed via a quadratic fit of the six points (three VMC and three ViT), $E = E_{\text{ex}} + \mathcal{A} \times \sigma^2 + \mathcal{B} \times (\sigma^2)^2$. The inclusion of the ViT data in the fit proves crucial in curing the apparent nonmonotonic behavior with system size in the zero-variance-extrapolated estimates of the ground-state energies (compare “ \mathbb{Z}_2 DSL extr.” versus “ \mathbb{Z}_2 DSL + ViT extr.” in Fig. 15, and see Table X for the corresponding energies), thus enabling a reliable estimation in the thermodynamic limit. A caveat of energy–variance extrapolation is that the relation between the variational energy E and the variance $\sigma^2 = \langle H^2 \rangle - \langle H \rangle^2$ is not universal across unrelated variational families. In general, both the slope and possible curvature of $E(\sigma^2)$ depend on how the trial state distributes its residual weight over excited eigenstates. As a consequence, different *Ansätze* may exhibit distinct finite-variance behavior even when they target the same ground state. For this reason, combining variational Monte Carlo (VMC) and variational tensor (ViT) data in a single extrapolation is justified only if both datasets populate the same smooth low-variance trend and extrapolate to a consistent zero-variance intercept. To verify this explicitly, we performed separate variance extrapolations for the VMC and ViT data, as well as a constrained fit allowing for method-dependent slopes (and curvature) but enforcing a common intercept E_0 . All procedures yield extrapolated ground-state ener-

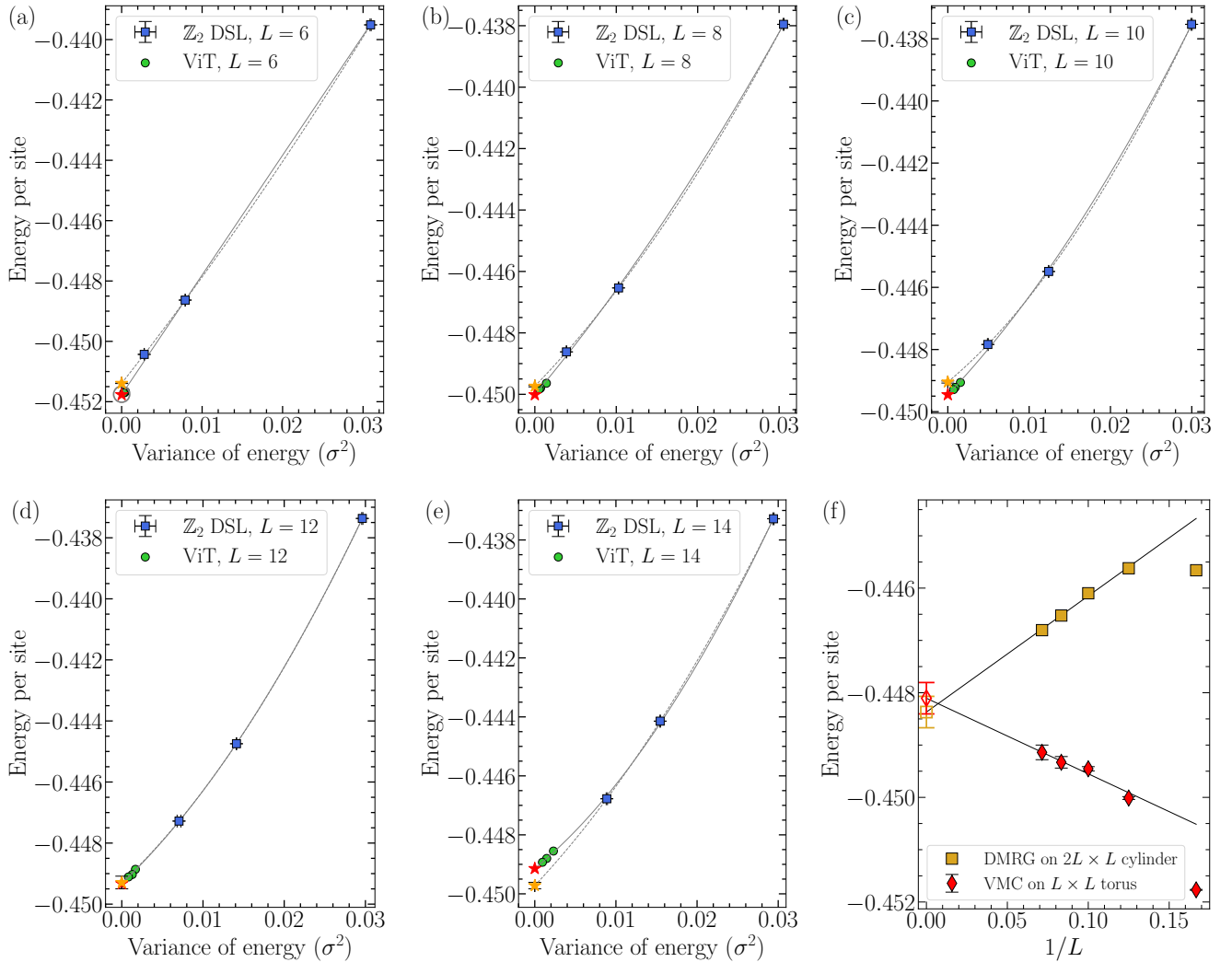


FIG. 14. Variational energies for the \mathbb{Z}_2 Dirac QSL (Z3000 state) at $J_s/J_d = 0.80$, as a function of the variance of energy, for zero, one, and two Lánczos steps. (a)–(e) An accurate estimate of the ground-state energy on the $L = 6, 8, 10, 12$, and 14 clusters is obtained by extrapolating the three variational results from VMC (blue squares) together with the ViT data (green circles) at smaller variance [46] to the zero-variance limit (red star) by a quadratic fit (solid curve). The estimate obtained by employing a quadratic fit (dashed curve) to only the three VMC points (blue squares) leads to less reliable values of the ground-state energy (yellow star), especially for larger system sizes, as seen by the nonmonotonic behavior thereof with respect to system size (see Fig. 15 and Table IX, and the main text for a description of the extrapolation method). For $L = 6$, the ED energy is marked by an empty circle. (f) The thermodynamic estimate of the ground-state energy, as obtained by a finite-size scaling of the estimated energies from VMC + ViT on the $L = 8, 10, 12$ and 14 clusters using a $1/L$ scaling form and a linear fit. The yellow squares provide a comparison with the DMRG estimates from Ref. [42].

gies that agree within uncertainties.

For our present purposes, the computationally demanding $p = 2$ calculations have been performed only for the $L = 6, 8, 10, 12$, and 14 clusters. It is worth emphasizing that this zero-variance extrapolation procedure yields size-consistent estimates of the energy per site for not only the ground state [104, 105] but also excited states [106]. In fact, it is well known that the Lánczos procedure (for a fixed p) becomes progressively inefficient upon increasing the system size, yet, the extrapolation remains accurate [102]. This can be observed from the

gain in the energy and the variance with respect to $p = 0$, which decreases with L (see Fig. 14 and Table IX), but the extrapolation is unaffected since the slope is essentially unchanged [48, 105]. Indeed, our estimate of the ground-state energy on the 6×6 cluster is in excellent agreement with the exact result, and equal (within error bars) to the corresponding estimate from ViT [46] (see Fig. 14(a) and Table X). Similarly, on the 8×8 and larger clusters, the estimate of the ground-state energy from VMC is equal (within error bars) to the ViT estimate (see Figs. 14(b)–(e) and Table X). By using the

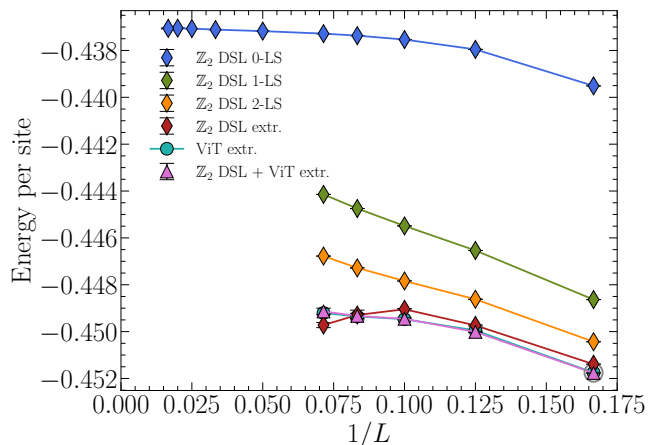


FIG. 15. The dependence on system size of the energies of the \mathbb{Z}_2 Dirac spin liquid (DSL), with $J_s/J_d = 0.8$, for $p = 0, 1, 2$ Lanczos steps and zero-variance extrapolated estimates using (i) only VMC data (\mathbb{Z}_2 DSL extr.), and (ii) combining VMC with lower-variance ViT data (\mathbb{Z}_2 DSL + ViT extr.) [46]. The latter is also consistent with ViT-only extrapolation estimates [46]. Also marked (gray circle) is the ED energy on a 36-site cluster.

ground-state energy estimates on different cluster sizes ($L = 8, 10, 12, 14$), we can also perform a finite-size extrapolation; see Fig. 14(f). At $J_s/J_d = 0.80$, our estimate for the energy per site of the infinite two-dimensional system is

$$E_\infty^{\text{2D}}/J_d = -0.4481(3). \quad (53)$$

This is equal (within error bars) to the ViT [46] and DMRG [43] estimates (see Fig. 14(f) and Table X), and we obtain this competitive value by optimizing *only* eight parameters [six from Eq. (49) and two from the Lanczos procedure in Eq. (52)], as opposed to the very large number of parameters that need to be optimized in the ViT [46] and DMRG [43] approaches. Note, moreover, that our energies are obtained for a state that has all the symmetries of the lattice by construction, while the DMRG states are computed on cylinders with open boundaries.

In summary, our energetic analysis lends support to the scenario of a \mathbb{Z}_2 Dirac state providing a good variational description of the gapless QSL reported in earlier studies [43, 46]. In the next section, based on an analysis of the correlation functions, we bolster the case for a \mathbb{Z}_2 QSL ground state and argue that it is the same phase as the QSL in the J_1 - J_2 square-lattice Heisenberg antiferromagnet [48].

2. Correlations

We begin by comparing the real-space, isotropic, equal-time, spin-spin correlations of the \mathbb{Z}_2 Dirac state (sup-

plemented with 2 LS) with those obtained from the unbiased neural-network ViT wavefunction, which has recently been diagnosed to feature gapless excitations [46]. In Fig. 16(a), for the $L = 14$ cluster, we notice that the Z3000 state correctly reproduces the sign of *all* ViT correlators with their magnitudes also being in excellent agreement. A similar level of concurrence between VMC, ViT, and ED correlators is also observed on the 6×6 cluster [see Fig. 16(b)]. In Fourier space, the equal-time spin structure factor of the projected \mathbb{Z}_2 Dirac state obtained from VMC displays soft maxima at (π, π) [see Fig. 16(c)] with its value on the $L = 14$ cluster being $\mathcal{S}(\pi, \pi) \approx 10.19$; this is to be compared with $\mathcal{S}(\pi, \pi) \approx 9.89$ obtained from ViT on the same cluster⁵. These results are in agreement and provide evidence that the gapless spin liquid found in Refs. [42, 46] is a \mathbb{Z}_2 Dirac QSL described by the Z3000 state.

In Fig. 17, we show the decay of real-space spin-spin correlations $|\langle \hat{\mathbf{S}}_i \cdot \hat{\mathbf{S}}_j \rangle|$ for the $(1, 0)$ direction on a 14×14 cluster at $J_s/J_d = 0.80$. Given the gapless nature of the phase, one expects that $|\langle \hat{\mathbf{S}}_i \cdot \hat{\mathbf{S}}_j \rangle| \propto |\mathbf{r}|^{-(z+\eta)}$, manifesting the critical behavior due to gapless triplet excitations. In fact, we find such a power-law decay with an exponent of $z + \eta = 1.35(3)$ indicating the critical nature of Neel antiferromagnetic correlations in the QSL phase, in accordance with the findings of DMRG and ViT [42, 46]. Since estimates from a single system size alone could have ambiguities, we corroborate our finding by also estimating the exponent from the system size dependence of $m^2(L) = \mathcal{S}(\pi, \pi)/N \approx L^{-(z+\eta)}$ [see Fig. 18(a)], which yields $z + \eta = 1.30(3)$; thus, both our estimates are in agreement with the DMRG and ViT estimate of ~ 1.3 [43, 46]. Given the \mathbb{Z}_2 nature of the QSL, we expect that upon tuning J_s/J_d (and other couplings that interpolate to the square lattice) the critical exponent will vary continuously across the river of liquidity and connect to the exponent of $1.4 \lesssim z + \eta \lesssim 1.6$ reported for the QSL phase in the J_1 - J_2 square lattice antiferromagnet. These findings provide evidence that the QSL region in the Shastry-Sutherland antiferromagnet is described by a \mathbb{Z}_2 Dirac QSL and could putatively be in the same phase as the QSL in the square-lattice Heisenberg antiferromagnet. Furthermore, this suggests a mechanism common to both lattices whereby Neel order melts due to frustration to give way to a gapless spin liquid [48].

Going beyond such equal-time correlations, next, we discuss the *dynamical* spin structure factors obtained using the Keldysh pseudo-fermion functional renormalization group (pf-FRG).

⁵ The VMC result is the zero-variance extrapolated estimate for the ground state which is obtained by supplementing the projected \mathbb{Z}_2 Dirac state with one and two Lanczos steps followed by a zero-variance extrapolation of $\mathcal{S}(\pi, \pi)$ via a quadratic fit, while the ViT result is extrapolated with the number of layers.

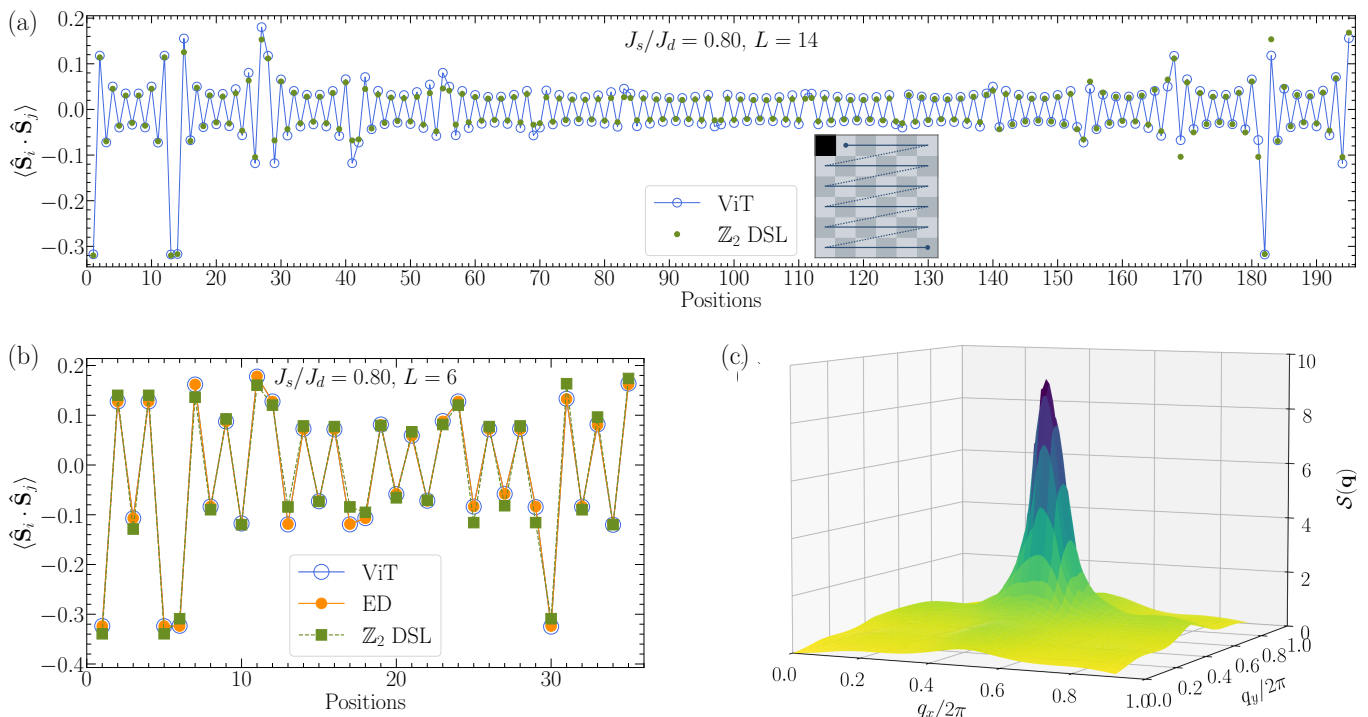


FIG. 16. (a) The equal-time isotropic spin-spin correlations $\langle \hat{S}_i \cdot \hat{S}_j \rangle$ in real space for the projected \mathbb{Z}_2 DSL (Z3000 state) supplemented with 2 LS, as computed using VMC (full green dots) and compared with the ViT wavefunction (empty blue circles) from Ref. [46] on a 14×14 lattice at $J_s/J_d = 0.80$. The error bars in VMC are $\sim \mathcal{O}(10^{-4})$. Inset: the blue line schematically illustrates the path on the $L = 14$ and $L = 6$ clusters along which the spin-spin correlations (with respect to the site marked in black) are ordered in the panel. Note that the ViT wavefunction explicitly breaks $SU(2)$ spin-rotation symmetry and the quantity plotted is $\langle \hat{S}^x \hat{S}^x + \hat{S}^y \hat{S}^y + \hat{S}^z \hat{S}^z \rangle$; our wavefunction is manifestly $SU(2)$ symmetric, and we thus plot $3 \times \langle \hat{S}^z \hat{S}^z \rangle$. (b) The same on an $L = 6$ cluster, now including a comparison with ED (orange circles). (c) The equal-time spin structure factor for the \mathbb{Z}_2 DSL (supplemented by 2 LS) obtained with VMC on a 14×14 lattice.

D. Keldysh pf-FRG

To compare the proposed *Ansätze* with numerical results, we employ a novel methodological approach: the pseudo-fermion functional renormalization group (pf-FRG) within the Keldysh formalism. This allows for direct computation of the dynamical spin structure factor for the Heisenberg model⁶. The pf-FRG is already a well-established method for investigating the ground-state properties of Heisenberg systems, especially for frustrated and higher-dimensional lattices, where conventional techniques such as DMRG, quantum Monte Carlo (QMC), and VMC face difficulties, e.g., the sign problem or challenges due to dimensionality [108].

The use of the Keldysh formalism makes it possible to calculate dynamical properties directly on the real-frequency axis, avoiding the need for analytical continuation associated with Matsubara frequencies (which is

known to be flawed due to numerical inaccuracies and is thus unreliable [109]). The drawback of the Keldysh pf-FRG is that we have to resort to a finite temperature for the calculations, which, in this case, is given by $T/J_d = 0.1$. This is because the FRG flow shows nonmonotonic features below this temperature scale—possibly due to the numerical integration schemes involved—which then induce artifacts in the structure factor. The Keldysh formalism also increases the computational cost, restricting our analysis to a 9×9 lattice. Furthermore, the starting point for the FRG is a quantum paramagnetic state, which, together with the finite temperature, suppresses effects around $(0, 0)$ that other techniques might predict more reliably. Thus, we cannot exclude a spectral branch emanating from the $\Gamma(0, 0)$ point at small frequencies, as obtained at the mean-field level [see Fig. 12(c)]. All details concerning the Keldysh pf-FRG are discussed in a companion publication [110].

In practice, we use the Keldysh pf-FRG to calculate the retarded dynamical spin susceptibility $\chi^{\text{ret}}(\mathbf{q}, \omega)$, which can be related to the spin structure factor by

$$\mathcal{S}^{\text{ret}}(\mathbf{q}, \omega) = \frac{1}{\pi} (1 - e^{-\beta\omega})^{-1} \text{Im}(\chi^{\text{ret}}(\mathbf{q}, \omega)). \quad (54)$$

⁶ Some early attempts have been made at obtaining $\mathcal{S}(\mathbf{q}, \omega)$ within the dimer phase of the SSM based on variants of perturbative approaches [107].

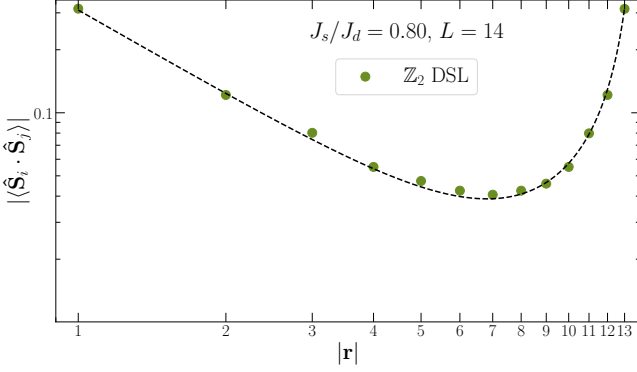


FIG. 17. The magnitude of (equal-time) isotropic real-space spin-spin correlations for the \mathbb{Z}_2 DSL plotted on a log-log scale for the $\mathbf{a}_1 = (1,0)$ direction on a 14×14 lattice for $J_s/J_d = 0.80$. The values of the spin-spin correlations are obtained by extrapolating the values of $\langle \hat{\mathbf{S}}_i \cdot \hat{\mathbf{S}}_j \rangle$ at zero, one, and two Lanczos steps to zero-variance employing a quadratic fit. To account for the periodic boundary conditions (which leads to the eventual upturn), the fit is to a power law [50, 51] $|\langle \hat{\mathbf{S}}_i \cdot \hat{\mathbf{S}}_j \rangle| \propto |\mathbf{r}|^{-z-\eta} + \sum_{\mathbf{R} \neq (0,0)} [(|\mathbf{r} - \mathbf{LR}|^{-z-\eta}) - (|\mathbf{LR}|^{-z-\eta})]$ with $z + \eta = 1.35(3)$, where $\mathbf{R} \equiv (R_x, R_y)$; here, $\mathbf{R} = R\mathbf{a}_1$ for $R = 1, \dots, L$. The error bars on $\langle \hat{\mathbf{S}}_i \cdot \hat{\mathbf{S}}_j \rangle$ are $\sim 10^{-4}$.

Naturally, we exclude small frequencies for which numerical artifacts would be artificially enhanced. Our results for the dynamical spin structure factor are presented in Fig. 19(a). Due to the finite temperature, we see very broadened branches but still, two distinct lobes of maximal intensity around (π, π) [at $(\pi \pm 0.4, \pi \pm 0.4)$] are discernible, while the (π, π) point itself also features appreciable intensity. This matches the expectation for the scenario of a \mathbb{Z}_2 Dirac QSL with nodal points at $M(\pi/2, \pi/2) + (\pm\varepsilon, \pm\varepsilon)$ [see Fig. 12(b)]. Indeed, scattering from thus-situated Dirac cones would result in the principal intensity at low energy being observed at $(\pi, \pi) \pm (2\varepsilon, 2\varepsilon)$ with relatively lesser intensity at (π, π) due to the presence of a larger number of scattering channels (wavevectors connecting different Dirac cones) for the former. Furthermore, we see a gradual decrease in intensity with increasing ω and a broad continuum consistent with deconfined fractionalized excitations, as expected for a \mathbb{Z}_2 QSL.

To facilitate a direct comparison with future neutron-scattering measurements on $\text{Pr}_2\text{Ga}_2\text{BeO}_7$ [7], we evaluate the dynamical structure factor $\mathcal{S}(\mathbf{q}, \omega)$ at $J_s/J_d = 0.80$ in the presence of XXZ anisotropy $J_{zz}/J_{xy} = 2.5$ on both J_s and J_d bonds, which has been proposed in Ref. [7] as a candidate minimal effective Hamiltonian. In Fig. 19(c), the calculated $\mathcal{S}(\mathbf{q}, \omega)$ exhibits two prominent lobes of spectral weight characteristic of the Dirac spin liquid. We further predict enhanced spectral intensity extending to higher ω , including a relative enhancement at the M' point compared to neighboring maxima [see Fig. 19(d)], together with vertical fountain-like streaks of scattering. The presence or absence of these features provides

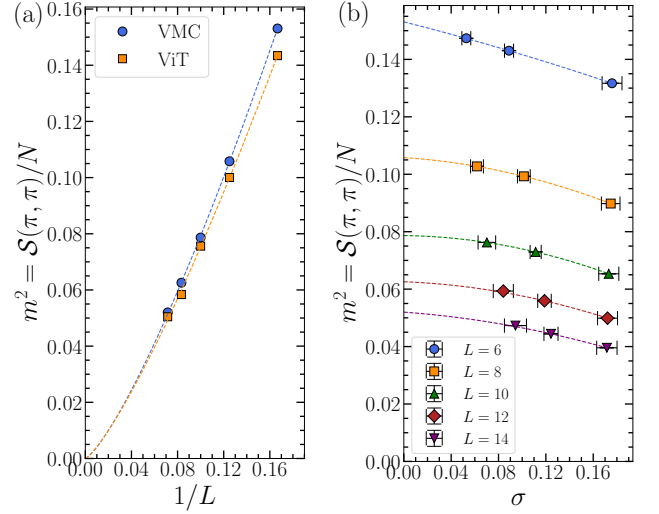


FIG. 18. (a) Finite-size scaling of the squared magnetization $m^2 = \mathcal{S}(\pi, \pi)/N$ (where $N = L \times L$) as a function of $1/L$ from $L = 6$ up to $L = 14$ obtained from VMC, and compared to ViT data from Ref. [46]. The values reported for each size L are obtained by extrapolating the values of m^2 at zero, one, and two Lanczos steps to zero-variance via a quadratic fit [see panel (b)], which yields their estimates in the ground state. The error bars of the extrapolated values in the thermodynamic limit are estimated via a resampling technique with Gaussian noise. The fits in (a) associated to dashed curves are obtained using the critical form $m^2 = aL^{-(z+\eta)}$, giving $z + \eta = 1.30(3)$.

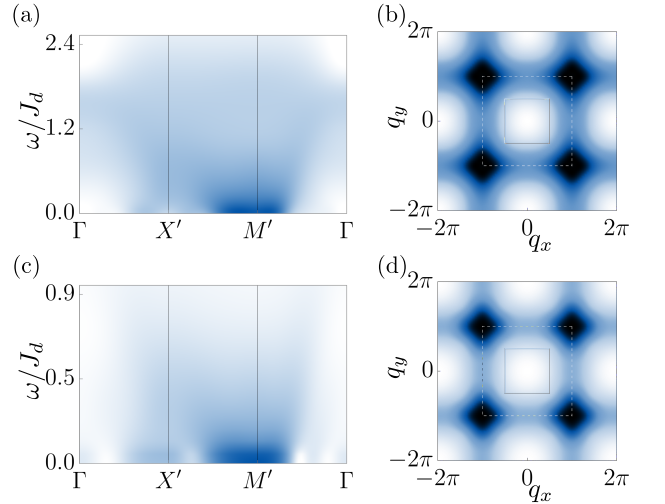


FIG. 19. (a) Dynamical and (b) equal-time spin structure factors obtained from Keldysh pf-FRG for $J_s/J_d = 0.80$ at $T/J_d = 0.1$ on a 9×9 lattice. (c, d) The corresponding structure factors upon introduction of an XXZ anisotropy of $J_{zz}/J_{xy} = 2.5$ relevant for $\text{Pr}_2\text{Ga}_2\text{BeO}_7$. The conventions for the color maps are adopted from those used in Figs. 12(c) and (d), respectively.

a direct and falsifiable benchmark for future neutron-scattering measurements probing the $(hk0)$ plane.

It is important to note that the corresponding classical ($S \rightarrow \infty$) model hosts an incommensurate spiral ground state for $J_s/J_d < 1$ [1, 111, 112]. The corresponding equal-time spin structure factor would show Bragg peaks at the incommensurate wave vectors (π, Θ) or (Θ, π) [25] with $\Theta = \pi \pm \arccos(J_s/J_d)$ (in the limit $S \rightarrow \infty$). Indeed, one of the double-maxima observed along the segment $\overline{X'M'}$ (at a shifted value of Θ due to quantum fluctuations [113]) reflects the underlying spiral correlations⁷, while the additional maxima along the segment $\overline{\Gamma M'}$ at points $(\pi \pm \varepsilon, \pi \pm \varepsilon)$, reflects the presence of Dirac cones and is not expected classically. Given that the Keldysh pf-FRG results have been obtained without any assumptions on the wavefunction or symmetry constraints and, in this sense, represent unbiased results from a correlator-based approach, they further corroborate the picture of a \mathbb{Z}_2 Dirac QSL ground state.

Unlike its dynamical counterpart, the equal-time spin structure factor provided by Keldysh pf-FRG instead shows broad diffuse maxima centered around (π, π) . This is due to the similar cumulative spectral weights obtained at and around (π, π) when $\mathcal{S}(\mathbf{q}, \omega)$ is integrated over ω , which washes out the underlying distribution of intensities at small ω . Moreover, this is consistent with the $\mathcal{S}(\mathbf{q})$ computed using VMC, which also shows a single broadened maxima at (π, π) [see Fig. 16(c)]. It is interesting to note that the equal-time $\mathcal{S}(\mathbf{q})$ obtained from both VMC [Fig. 16(c)] and Keldysh pf-FRG [Fig. 19(b)] do not qualitatively differ from the mean-field profile [see Fig. 12(d)]. This is likely due to the fact that the \mathbb{Z}_2 gauge field is gapped, mediating only short-range interactions between spinons, and it does not significantly alter the mean-field expectation [57]. In contrast, for gapless states with a U(1) IGG, gauge fluctuations can lead to drastic differences between the mean-field and projected $\mathcal{S}(\mathbf{q})$ (cf. Ref. [114] for the kagome U(1) Dirac QSL).

VI. PHASE DIAGRAM

Having identified the nature of the QSL, we now investigate its energetic competition with the neighboring Néel antiferromagnetic and plaquette VBC phases that flank the spin-liquid regime. Since the QSL wavefunction is obtained as the ground state of a spin-rotation-invariant mean-field Hamiltonian [Eq. (49)], it is, by construction, incapable of developing magnetic order; in particular, the AFM order parameter vanishes identically. Consequently, to address the transition between

Method	$(J_s/J_d)_{\text{PVBC}}$	$(J_s/J_d)_{\text{Néel}}$
VMC	≈ 0.78	≈ 0.83
DMRG (Yang <i>et al.</i> [42])	0.788(2)	0.820(2)
ED (Wang <i>et al.</i> [43])	0.789(4)	0.824(8)
pf-FRG (Keleş <i>et al.</i> [32])	≈ 0.77	≈ 0.82
ViT (Viteritti <i>et al.</i> [46])	0.775(5)	0.815(5)
iPEPS (Corboz <i>et al.</i> [116])	0.785(5)	0.82(1)

TABLE XI. Critical coupling ratios for the transitions between the QSL and the plaquette VBC, $(J_s/J_d)_{\text{PVBC}}$, and between the QSL and the Néel antiferromagnet, $(J_s/J_d)_{\text{Néel}}$, as obtained from variational Monte Carlo (VMC), and compared against results from other numerical methods.

the QSL and the Néel AFM phase, it is necessary to construct a variational wavefunction that explicitly supports magnetic order. By employing two restricted classes of wavefunctions—one constrained to describe the QSL and the other to capture AFM order—we can independently evaluate the corresponding variational energies and locate the phase transition from the intersection of these energy curves.

A simple yet accurate variational wavefunction for magnetically ordered phases can be constructed directly in terms of the spin degrees of freedom [115]:

$$|\Psi_{\text{Magnetic}}\rangle = \mathcal{J}_z \mathcal{P}_{S_{\text{tot}}^z=0} |\text{SW}\rangle, \quad (55)$$

where $|\text{SW}\rangle$ is a spin-wave state characterized by a wavevector \mathbf{q} and a set of phase shifts $\{\eta_i\}$, one for each site in the unit cell,

$$|\text{SW}\rangle = \prod_i \left(|\downarrow\rangle_i + e^{i(\mathbf{q}\cdot\mathbf{R}_i + \eta_i)} |\uparrow\rangle_i \right). \quad (56)$$

The state $|\text{SW}\rangle$ is equivalent to a classical configuration in which each spin points along a fixed direction in the XY-plane. The operator $\mathcal{P}_{S_{\text{tot}}^z=0}$ projects onto the subspace with vanishing total magnetization along the z -axis. Quantum fluctuations beyond the classical spin configuration are incorporated through a long-range Jastrow factor,

$$\mathcal{J}_z = \exp\left(\frac{1}{2} \sum_{ij} v_{ij} \hat{S}_i^z \hat{S}_j^z\right), \quad (57)$$

where, in a translationally invariant system, the pseudopotential v_{ij} depends only on the distance $|\mathbf{R}_i - \mathbf{R}_j|$ between sites. In the following, we focus on the Néel ordering vector $\mathbf{q} = (\pi, \pi)$, for which the four spins in the unit cell form an antiparallel arrangement. All independent parameters entering the pseudopotential v_{ij} are optimized using variational Monte Carlo simulations.

We perform VMC calculations to determine the optimized energies of the Z3000 quantum spin liquid and the Néel antiferromagnetic state using the wavefunctions

⁷ Such a spiral phase was also shown to have a higher energy within the coupled-cluster approach [19].

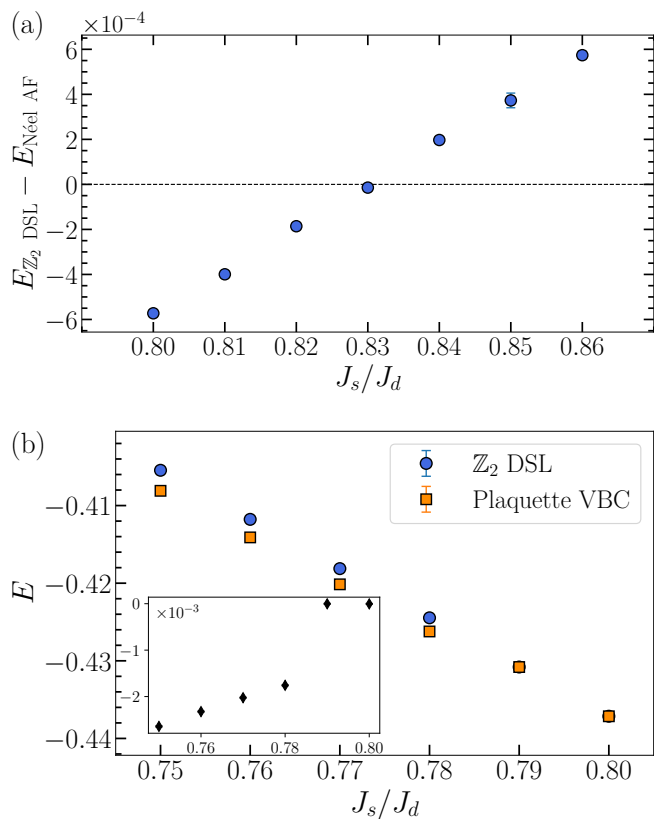


FIG. 20. (a) The net energy difference per site, $(E_{Z_2 \text{ DSL}} - E_{\text{Néel AFM}})/J_d$, on an $L = 30$ (900 sites) cluster as a function of J_s/J_d . The transition point is identified from the intersection with the dashed line corresponding to zero difference in energies, yielding an estimate of $J_s/J_d \approx 0.83$. No systematic shift of this crossing is observed within numerical error upon increasing the system size. The resulting energy difference, of order 10^{-4} , is consistent with previous findings [116]. (b) Evolution with J_s/J_d of the energy per site, E/J_d , of the Z_2 Dirac QSL and plaquette VBC states on the same $L = 30$ cluster. Inset: energy difference $E_{\text{PVBC}} - E_{Z_2 \text{ DSL}}$. For $J_s/J_d \lesssim 0.78$, the plaquette VBC has a lower variational energy than the $Z_2 \text{ DSL}$, with an energy gain that increases as J_s/J_d is further reduced. In both panels, the statistical error bars are of order 10^{-6} .

introduced above. The energy difference between these two competing states on an $L = 30$ cluster is shown in Fig. 20(a). The crossing with the dashed line defined by $E_{Z_2 \text{ DSL}} - E_{\text{Néel AFM}} = 0$ yields an estimate of the transition point $(J_s/J_d)_{\text{Néel}} \approx 0.83$, in excellent agreement with results obtained from other numerical approaches (see Table XI). Upon increasing the system size, we observe no systematic shift of the crossing within statistical error bars, indicating that this estimate provides a reliable determination of the QSL–Néel AFM transition in the thermodynamic limit.

To construct variational wavefunctions for the plaquette VBC—a phase that preserves translational symmetry while breaking glide G_x and mirror σ_{xy} symmetries—we classify projective symmetry groups compatible with

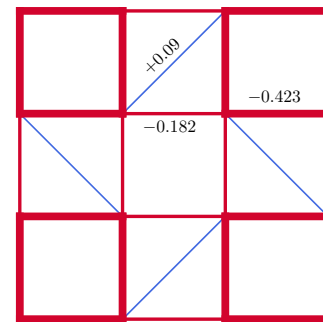


FIG. 21. Real-space spin-spin correlations $\langle \hat{S}_i \cdot \hat{S}_j \rangle$ obtained from a representative VMC snapshot taken from the center of an $L = 30$ cluster at $J_s/J_d = 0.76$. The width of each bond is proportional to the magnitude of $\langle \hat{S}_i \cdot \hat{S}_j \rangle$, while red (blue) bonds indicate antiferromagnetic (ferromagnetic) correlations. The numerical values of the correlations are indicated on the corresponding bonds. Clear singlet formation is observed on the empty square plaquettes, characteristic of the plaquette VBC phase. Statistical error bars are of order 10^{-5} .

this reduced symmetry set (see Appendix G). We identify the PSG of the plaquette VBC that continuously descends from the Z3000 QSL and construct the corresponding fermionic mean-field Hamiltonian [Eq. (G12) and Fig. 33]. Importantly, this Hamiltonian is smoothly connected to that of the fully symmetric Z3000 QSL [Eq. (49)], which is recovered when symmetry-inequivalent hopping and pairing amplitudes are tuned to be equal.

Starting from this mean-field description, we generate the ground state and optimize the corresponding Gutzwiller-projected variational wavefunction within VMC. We find that for $J_s/J_d \lesssim 0.78$, the optimized plaquette VBC wavefunction attains a lower energy than the Z3000 QSL on the largest system sizes studied ($L = 30$), with an energy gain that remains finite upon increasing system size [see Fig. 20(b)]. The associated real-space spin-spin correlations, shown in Fig. 21 for $J_s/J_d = 0.76$, clearly reveal singlet formation on the empty square plaquettes. By contrast, for $J_s/J_d \gtrsim 0.78$, the plaquette VBC wavefunction flows back to the fully symmetric QSL upon variational optimization. These results offer an estimate of the QSL–plaquette VBC transition at $(J_s/J_d)_{\text{PVBC}} \approx 0.78$, consistent with other numerical studies (Table XI), and establish the stability of the plaquette VBC phase in the thermodynamic limit.

VII. CONCLUSIONS AND OUTLOOK

A central pillar of our identification of the quantum spin liquid on the Shastry-Sutherland lattice is provided by symmetry-resolved exact diagonalization. By tracking the evolution of low-energy states across total-spin, reflection, and glide symmetry sectors, we identify a finite

intermediate regime in which neither the Anderson tower of states associated with Néel order nor the quasidegenerate singlet manifold characteristic of plaquette or columnar symmetry breaking is present. The composite gap crossings introduced in Ref. [43] remain well separated under finite-size scaling, demonstrating that this regime is not a fine-tuned point but a finite-width phase.

Importantly, as the Hamiltonian is continuously deformed from the Shastry-Sutherland limit to the square-lattice J_1 - J_2 model, the symmetry-resolved spectrum evolves smoothly without qualitative reorganization. The resulting river of liquidity establishes adiabatic continuity between the two models. Wavefunction overlap diagnostics independently confirm that the same ground-state manifold persists throughout this interpolation. Taken together, these exact-diagonalization results provide controlled spectral evidence that the intermediate phase is a genuine quantum-disordered state extending across distinct frustrated Hamiltonians.

To identify the precise nature of the QSL, our work charts out an atlas of QSLs on the Shastry-Sutherland lattice along with their spectroscopic signatures. This is accomplished using the framework of projective symmetry groups, which, for fermionic spinons, yields 46 $U(1)$ and 80 \mathbb{Z}_2 QSL states. Using this information, we investigate the QSL regime of the generalized spin-1/2 Shastry-Sutherland Heisenberg antiferromagnet and its interpolation to the square-lattice limit. We identify the subset of PSGs which can be continuously connected to the ones on the square lattice. In particular, we pinpoint the counterpart of the \mathbb{Z}_2 Dirac QSL on the square lattice (more precisely, the d -wave pairing Z2Azz13 state in Ref. [56]), which is a prime candidate for the QSL ground state of the $S=1/2$ J_1 - J_2 square-lattice Heisenberg antiferromagnet. Our equivalent \mathbb{Z}_2 Dirac QSL (called the Z3000 state in this work) upon Gutzwiller projection and optimization over only a few parameters—using variational Monte Carlo—produces energies which are equal, within error bars, to those obtained from ViT, for all cluster sizes [46], and from DMRG [42], in the thermodynamic limit. Similarly, the equal-time correlators computed with VMC for this \mathbb{Z}_2 Dirac QSL show remarkable qualitative and *quantitative* agreement across system sizes with those found from unconstrained ViT wavefunctions. The long-distance decay of the real-space spin-spin correlators follows a power law with a critical exponent $z+\eta = 1.30(3)$, which is in agreement with that obtained from DMRG and ViT [42, 46], thus providing compelling evidence for the \mathbb{Z}_2 Dirac QSL as the prime candidate for the gapless QSLs reported in these studies. We also apply the newly developed Keldysh pseudo-fermion functional renormalization group to evaluate the dynamical spin structure factor, which shows a maxima along the segment connecting $(0,0)$ and (π,π) and subdominant intensity at (π,π) , as would be expected from scattering by Dirac cones at $(\pi/2, \pi/2) + (\pm\varepsilon, \pm\varepsilon)$. This

observation adds to the evidence for a \mathbb{Z}_2 Dirac QSL from an independent correlator-based approach, which is blind to specific *Ansätze* and is not dictated by symmetry constraints. Further, given the rapid experimental and theoretical developments in exploring putative QSL behavior on the Shastry-Sutherland lattice, these predictions for the dynamical structure factors set the stage for directly identifying such exotic states in materials and models from spectroscopic signatures.

Our classification of QSLs compatible with the reduced symmetry of the proximate plaquette VBC order, i.e., preserving C_4 but breaking glide and mirror symmetries (see Appendix G), allows us to study the phase transitions of fully symmetric QSLs to their descendent plaquette VBC orders. In particular, we demonstrate an instability of the Z3000 state to its plaquette VBC counterpart at $J_s/J_d \approx 0.78$, in agreement with estimates from other studies. Notably, a different class of gapped lattice-nematic \mathbb{Z}_2 QSLs, which instead break 90° rotational symmetry, have previously been identified within the Schwinger-boson formalism [25]. Such a nematic state has also been studied with Abrikosov fermions but for the square lattice [117]; it would be interesting to extend this classification to the Shastry-Sutherland lattice in future work. To investigate the transition from the \mathbb{Z}_2 Dirac QSL to the Néel phase, we construct Jastrow wavefunctions and find that their energies intersect at $J_s/J_d \approx 0.83$, yielding an accurate estimate of the transition point.

While the microscopic mean-field representation of the optimal state on the Shastry-Sutherland lattice involves several symmetry-inequivalent hopping and pairing amplitudes, its long-wavelength content is much simpler [41]: it realizes a gapless \mathbb{Z}_2 Dirac spin liquid (Z3000) that can be viewed as a Higgs descendant of the $SU(2)$ π -flux parent via an intermediate $U(1)$ staggered-flux state. In this sense, the role of the PSG is not primarily to provide “insight by nomenclature”, but to uniquely determine the projective action of lattice symmetries on the fractionalized spinons and Higgs fields, thereby fixing the symmetry-allowed structure of the continuum gauge theory. In this way, the PSG framework encodes the quantum order of the spin liquid and establishes its universality class. In a companion work [41], we exploited this PSG analysis to construct an explicit continuum description on the Shastry-Sutherland lattice and showed that—despite the reduced microscopic symmetry relative to the square lattice—the leading Dirac-spinon Lagrangian and the Higgs potential governing the mean-field phase diagram are identical to the square-lattice theory [118] up to additional irrelevant operators. This provides a unified field-theoretic framework for Dirac spin liquids on both lattices and motivates interpreting the proximate Néel- \mathbb{Z}_2 -VBC phase structure through the lens of fermionic deconfined quantum criticality. The agreement between the two lattices extends to critical exponents and the

mechanism of pseudocriticality (via the relevant Yukawa coupling between spinons and Higgs fields), offering a controlled theoretical setting for the numerical signatures observed in both square-lattice and Shastry-Sutherland models.

Given the rather narrow region of stability for the Shastry-Sutherland QSL along the Heisenberg axis, it would also be interesting to identify directions in Hamiltonian parameter space which possibly widen this regime. To this end, there is evidence from DMRG [7] that the introduction of an XY-type anisotropy enlarges the window of stability of the QSL, and it is worth examining whether the same \mathbb{Z}_2 Dirac QSL as the one on the Heisenberg axis remains stable upon the introduction of XXZ anisotropy or whether a new QSL phase occupies this region. Moreover, the inclusion of an explicit scalar spin-chirality term in the Hamiltonian has recently been shown to induce a chiral spin liquid (CSL) of the Kalmeyer-Laughlin type [119]. Since there exist myriad distinct Kalmeyer-Laughlin CSLs—differing in their anyon content—within parton constructions, in order to uncover the microscopic nature of the CSL, it would be necessary to obtain the chiral representation classes for the algebraic PSGs [69] of the Shastry-Sutherland lattice. Assessing the energetics and correlation functions of the corresponding Gutzwiller-projected chiral *Ansätze* would then help pin down the precise CSL that provides the best variational description of the ground state. Closely tied to this is the issue of identifying, within this classification scheme, the CSLs which serve as natural candidates for continuous transitions out of our \mathbb{Z}_2 Dirac QSL. These could include the rare class of gapless CSLs [120, 121] (such as Dirac [122] and spinon Fermi surface [66] chiral QSLs), or conventional gapped CSLs.

Unlike gapped spin liquids, gapless spin liquids support low-energy quasiparticle branches with degrees of freedom that exist arbitrarily close to the ground state. This can lead to rather peculiar low-temperature behavior. It would, for instance, imply a nonvanishing thermal conductivity κ_{xx}/T at an arbitrarily low temperature. If time-reversal symmetry is broken (either intrinsically or by an external perturbation), a chiral gapless spin liquid will likewise produce a finite thermal Hall response. Doping a gapless spin liquid also leads to a subtle intertwining of charge and spin degrees of freedom. Finally, from a thermodynamic stability standpoint, gapless spin liquids could, in principle, be preferentially favored at finite temperature because their low-energy excitations contribute additional entropy. Consider a *Gedankenexperiment* with a gapped and a gapless spin liquid that have the same internal energy at $T = 0$. At finite temperature, the gapless phase acquires a larger entropy, so its free energy is entropically reduced relative to the gapped phase, making the gapless state thermodynamically preferred. Such entropy-driven stabilization of gapless behavior has indeed been reported in recent experimental

studies of candidate quantum spin-liquid materials.

With regard to experimental realizations of the Shastry-Sutherland lattice, the field of quantum materials is currently witnessing the arrival of several new candidates whose magnetic lattices are based on rare-earth ions of Ce^{3+} [6], Pr^{3+} [7], Yb^{3+} [9], and Er^{3+} [10]. Some of these compounds offer tantalizing evidence of nonmagnetic behaviors at low temperatures and could thus potentially host exotic QSL phases, including in the presence of magnetic fields. Recent works [123, 124] have shown that these spin-orbit-coupled systems are effectively described by generalized XYZ models. In particular, $\text{Pr}_2\text{Ga}_2\text{BeO}_7$ has been argued to be described by an XXZ model to a first approximation [7]. In light of thermodynamic measurements observing a T^2 dependence of the specific heat, a finite κ_0/T (and an associated T -linear term in the specific heat) from a residual density of states ascribed to disorder, and gapless inelastic neutron spectra, the likely scenario is that of a gapless QSL being realized. Indeed, it has been speculated [7] that a d -wave pairing \mathbb{Z}_2 QSL would be consistent with these experimental findings. Our \mathbb{Z}_2 QSL Z3000 is, in fact, a d -wave pairing state, and evidence from our Keldysh pf-FRG calculations indicates that it persists upon the introduction of XXZ anisotropy (similar to the kagome U(1) QSL, which is stable to XXZ anisotropy in the Hamiltonian [125]). Furthermore, our $\mathcal{S}(\mathbf{q}, \omega)$ obtained by Keldysh pf-FRG for the XXZ model description of $\text{Pr}_2\text{Ga}_2\text{BeO}_7$ reproduce all the principal features of the neutron scattering profile. Therefore, our work sheds light on the precise microscopic character of the suspected QSL phase in $\text{Pr}_2\text{Ga}_2\text{BeO}_7$ as well. The methodological development we present together with the dynamical spin structure factors of candidate quantum spin liquids on the Shastry-Sutherland lattice will serve as a valuable guide to identifying the nature of spin liquids in a variety of candidate QSL materials which are currently being investigated experimentally.

From symmetry considerations alone, a Dzyaloshinskii-Moriya interaction is also allowed [126, 127] and likely plays an important role in modeling the behavior of Shastry-Sutherland materials. Hence, to expand the applicability of our approach to these spin-orbit-coupled rare-earth systems, one has to extend the *Ansätze* described herein by incorporating triplet amplitudes and evaluating their energetic competitiveness for the relevant anisotropic models [128]. Finally, QSL behavior has also been observed in a magnetic field, e.g., in $\text{Yb}_2\text{Be}_2\text{GeO}_7$ [9], so it would be important to determine the stability of the proposed \mathbb{Z}_2 Dirac QSL in a magnetic field, along the lines of the analysis performed for the kagome U(1) Dirac QSL in Ref. [129].

ACKNOWLEDGMENTS

We thank Federico Becca, Bryan Clark, Chunxiao Liu, Yukitoshi Motome, Yusuke Nomura, Rico Pohle, Mingpu Qin, Subir Sachdev, Anders Sandvik, Leyna Shackleton, Yanting Teng, Chandra Varma, and Luciano Viteritti for helpful discussions. Y.I. thanks Luciano Viteritti and Federico Becca for providing us with the data from Ref. [46] and discussing the detailed comparison between ViT and VMC results. R.S. was supported by the Princeton Quantum Initiative Fellowship. The work of Y.I., J.Y.L., K.P., and R.S. was performed, in part, at the Aspen Center for Physics, which is supported by National Science Foundation Grant No. PHY-2210452 and a grant from the Simons Foundation (1161654, Troyer). This research was supported in part by grant NSF PHY-2309135 to the Kavli Institute for Theoretical Physics (KITP). Y.I. acknowledges support from the ICTP through the Associates Programme, from the Simons Foundation through Grant No. 284558FY19, IIT Madras through the Institute of Eminence (IoE) program for establishing QuCenDiEM (Project No. SP22231244CPETWOQCDHOC), and the International Centre for Theoretical Sciences (ICTS), Bengaluru during a visit for participating in the program: Kagome off-scale (ICTS/KAGOFF2024/08). Y.I. also acknowledges the use of the computing resources at HPCE, IIT Madras. SC thanks CALMIP (grant 2025-P0677) and GENCI (project A0190500225) for computing resources. The work in Würzburg is supported by the Deutsche Forschungsgemeinschaft (DFG, German Research Foundation) through Project-ID 258499086 - SFB 1170 and through the Würzburg-Dresden Cluster of Excellence on Complexity, Topology and Dynamics in Quantum Matter - ctd.qmat Project-ID 390858490 - EXC 2147. R.T., F.F., and K.P. thank IIT Madras for a IoE Visiting Scientist position which enabled the completion of this work.

DATA AVAILABILITY STATEMENT

The data generated during the current study are available from the corresponding author upon reasonable request.

Appendix A: Exact diagonalization for 20-, 24-, 28-, and 40-site clusters

Here, we provide additional details on our exact diagonalization simulations performed on finite-size periodic clusters of up to $N = 40$ sites. We refer to standard reviews, e.g., Ref. [130], for additional technical details about the implementation of symmetries and the diagonalization of low-energy states using the Lánczos algorithm. Exploiting lattice symmetries is useful not only to reduce the size of the Hilbert space but also to provide crucial information about quantum numbers of each eigenstate, which allowed us to discuss specific level crossings in the main text.

Due to the four-site unit cell of the Shastry-Sutherland lattice, as well as the interpolation, one can only use $N/4$ translations for a periodic N -site cluster. As noted in the analysis by Wang *et al.* [43], the relevant low-energy levels are all located at the Γ point of the Shastry-Sutherland lattice. Concerning point-group symmetries, among the accessible finite-size clusters, only $N = 16, 32,$ and 36 possess the full D_4 symmetry group, which includes a fourfold rotation axis about the center of a fully crossed plaquette with \mathcal{J} Heisenberg couplings, together with an additional mirror symmetry; we exclude the $N = 16$ cluster because of its small size. Some other clusters have smaller point groups: C_4 for $N = 20$ and $N = 40$, and only C_2 for $N = 24$ and $N = 28$. Additional details can be found in Fig. 2 of Ref. [43] and Table I.

For the largest cluster considered ($N = 40$), the Hilbert-space dimension exceeds 3×10^9 states in the zero-magnetization sector when spin-reversal symmetry is used, and 5×10^9 states in the $S_z^{\text{tot}} = 2$ sector used to target quintuplet excitations. For such large matrices, we have obtained quicker results using only the C_2 subgroup of its C_4 point group, thanks to a sublattice coding algorithm [131]. Since this does not allow one to fully reconstruct all quantum numbers, we have also performed more expensive simulations for few parameters using the full C_4 point group. As shown in Fig. 25, both sets of data agree very well, when available, and the slightly larger discrepancies observed for some excited states originate from their slower convergence, which is a well-known feature of the Lánczos method. We also note that spurious eigenstates, commonly referred to as *ghosts*, could also appear during the simulations.

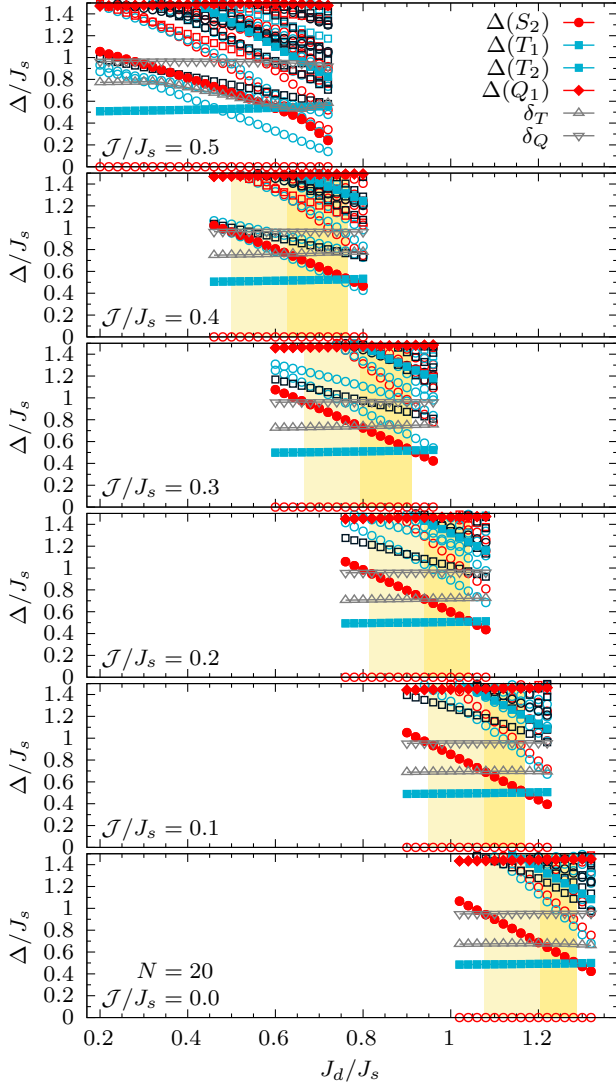


FIG. 22. Symmetry-resolved low-energy excitation spectrum obtained from Lanczos exact diagonalization for the $N = 20$ cluster as the Hamiltonian is interpolated from the Shastry-Sutherland limit toward the J_1 - J_2 model. The notation and symmetry labeling conventions are the same as in Fig. 3.

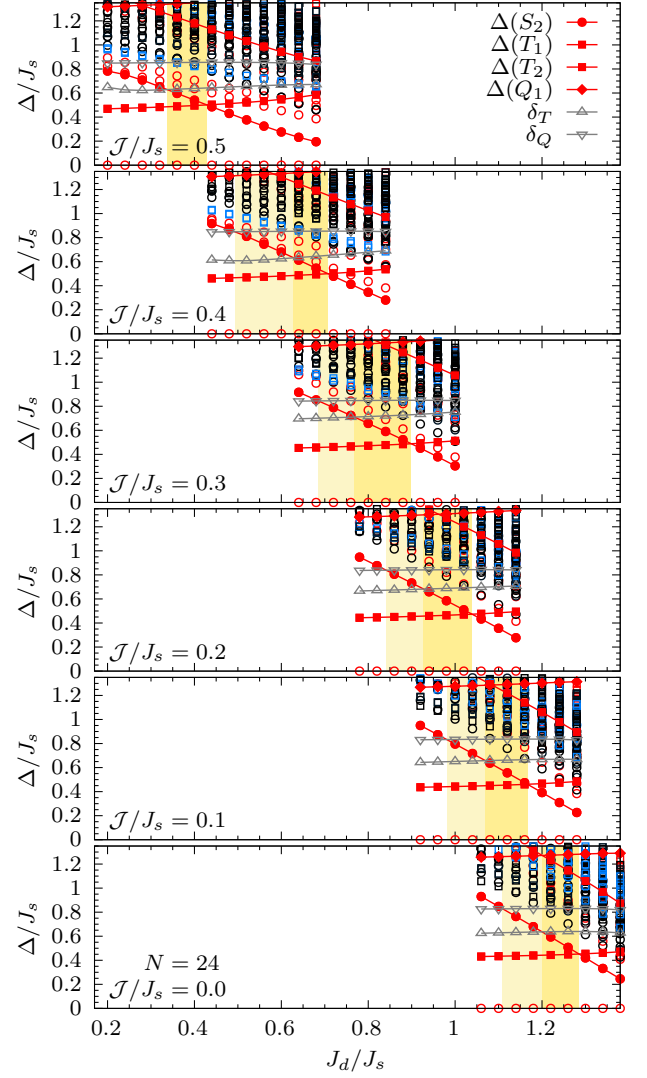


FIG. 23. Symmetry-resolved low-energy excitation spectrum obtained from Lanczos exact diagonalization for the $N = 24$ cluster as the Hamiltonian is interpolated from the Shastry-Sutherland limit toward the J_1 - J_2 model. The notation and symmetry labeling conventions are the same as in Fig. 3.

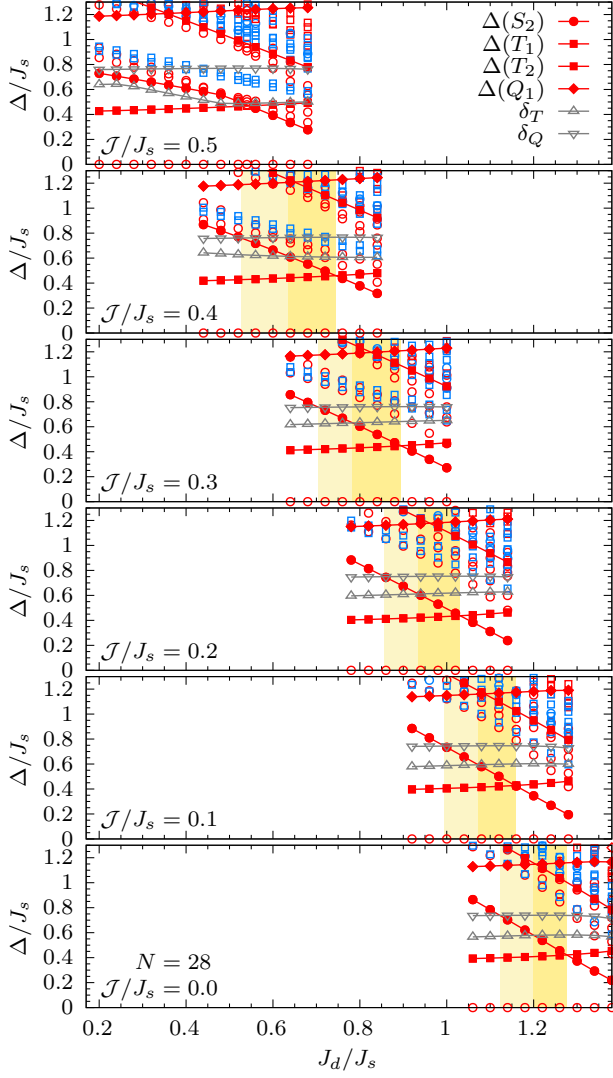


FIG. 24. Symmetry-resolved low-energy excitation spectrum obtained from Lanczos exact diagonalization for the $N = 28$ cluster as the Hamiltonian is interpolated from the Shastry-Sutherland limit toward the J_1 - J_2 model. The notation and symmetry labeling conventions are the same as in Fig. 3.

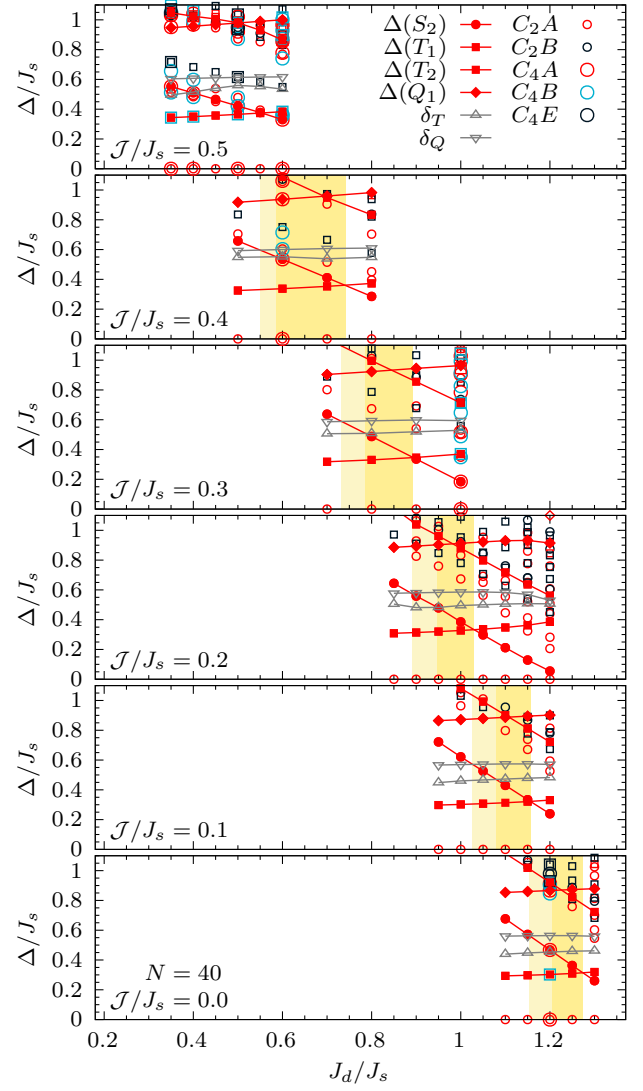


FIG. 25. Symmetry-resolved low-energy excitation spectra obtained from Lanczos exact diagonalization for the $N = 40$ cluster as the Hamiltonian is interpolated from the Shastry-Sutherland limit toward the J_1 - J_2 model. The notation and symmetry labeling conventions are the same as in Fig. 3. Most calculations exploit only the C_2 symmetry. Due to their higher computational cost, calculations implementing the C_4 symmetry of the cluster were only performed at selected points (larger symbols) to identify the corresponding irreducible representations.

Appendix B: Gauge-enriched symmetry relations

The relations between the different symmetry elements of the Shastry-Sutherland lattice are specified by the identities listed in Eq. (18). The projective extensions of these symmetries, $W_{\mathcal{O}}$, necessarily follow the same algebraic relations, which read as:

$$W_{T_x}^{-1}(T_x(\mathbf{r}))W_{T_y}^{-1}(T_x T_y(\mathbf{r}))W_{T_x}(T_x T_y(\mathbf{r}))W_{T_y}(T_y(\mathbf{r})) = F_3(\xi_y) \quad \text{or} \quad \eta_y \tau^0, \quad (\text{B1a})$$

$$W_{G_x}^{-1}(G_x(\mathbf{r}))W_{T_x}^{-1}(G_x T_x(\mathbf{r}))W_{G_x}(G_x T_x(\mathbf{r}))W_{T_x}(T_x(\mathbf{r})) = F_3(\xi_{G_{xx}}) \quad \text{or} \quad \eta_{G_{xx}} \tau^0, \quad (\text{B1b})$$

$$W_{G_x}^{-1}(G_x(\mathbf{r}))W_{T_y}^{-1}(G_x T_y(\mathbf{r}))W_{G_x}(G_x T_y(\mathbf{r}))W_{T_y}(T_y(\mathbf{r})) = F_3(\xi_{G_{xy}}) \quad \text{or} \quad \eta_{G_{xy}} \tau^0, \quad (\text{B1c})$$

$$W_{T_x}^{-1}(T_x(\mathbf{r}))W_{G_x}(T_x(\mathbf{r}))W_{G_x}(G_x(\mathbf{r})) = F_3(\xi_{G_x T_x}) \quad \text{or} \quad \eta_{G_x T_x} \tau^0, \quad (\text{B1d})$$

$$W_{T_y}^{-1}(T_y(\mathbf{r}))W_{\sigma_{xy}}^{-1}(T_x \sigma_{xy}(\mathbf{r}))W_{T_x}(T_x \sigma_{xy}(\mathbf{r}))W_{\sigma_{xy}}(\sigma_{xy}(\mathbf{r})) = F_3(\xi_{\sigma_{xy} T_x}) \quad \text{or} \quad \eta_{\sigma_{xy} T_x} \tau^0, \quad (\text{B1e})$$

$$W_{T_x}^{-1}(T_x(\mathbf{r}))W_{\sigma_{xy}}^{-1}(T_y \sigma_{xy}(\mathbf{r}))W_{T_y}(T_y \sigma_{xy}(\mathbf{r}))W_{\sigma_{xy}}(\sigma_{xy}(\mathbf{r})) = F_3(\xi_{\sigma_{xy} T_y}) \quad \text{or} \quad \eta_{\sigma_{xy} T_y} \tau^0, \quad (\text{B1f})$$

$$\begin{aligned} W_{\sigma_{xy}}(\mathbf{r})W_{G_x}(\sigma_{xy}^{-1}(\mathbf{r}))W_{\sigma_{xy}}((\sigma_{xy} G_x)^3(\mathbf{r}))W_{G_x}(G_x(\sigma_{xy} G_x)^2(\mathbf{r}))W_{\sigma_{xy}}((\sigma_{xy} G_x)^2(\mathbf{r})) \\ \times W_{G_x}(G_x \sigma_{xy} G_x(\mathbf{r}))W_{\sigma_{xy}}(\sigma_{xy} G_x(\mathbf{r}))W_{G_x}(G_x(\mathbf{r})) = F_3(\xi_{\sigma_{xy} G_x}) \quad \text{or} \quad \eta_{\sigma_{xy} G_x} \tau^0, \end{aligned} \quad (\text{B1g})$$

$$W_{\sigma_{xy}}(\sigma_{xy}(\mathbf{r}))W_{\sigma_{xy}}(\mathbf{r}) = F_3(\xi_{\sigma_{xy}}) \quad \text{or} \quad \eta_{\sigma_{xy}} \tau^0, \quad (\text{B1h})$$

$$W_{\mathcal{T}}(\mathbf{r})W_{\mathcal{T}}(\mathbf{r}) = F_3(\xi_{\mathcal{T}}) \quad \text{or} \quad \eta_{\mathcal{T}} \tau^0, \quad (\text{B1i})$$

$$W_{\mathcal{T}}(\mathbf{r})W_{\mathcal{O}}(\mathbf{r})W_{\mathcal{T}}^{-1}(\mathcal{O}^{-1}(\mathbf{r}))W_{\mathcal{O}}^{-1}(\mathbf{r}) = F_3(\xi_{\mathcal{T}\mathcal{O}}) \quad \text{or} \quad \eta_{\mathcal{T}\mathcal{O}} \tau^0. \quad (\text{B1j})$$

On the right-hand side of the equations above, the first expression defines the relations for the case of a U(1) IGG, where $0 \leq \xi_{\dots} < 2\pi$ is a global U(1) phase and, as defined in the main text, $F_3(\xi) \equiv \exp(i\xi\tau^z)$. The second set of expressions, following the ‘‘or’’, corresponds to a \mathbb{Z}_2 IGG, with $\eta_{\dots} = \pm 1$ being a global \mathbb{Z}_2 sign. As they stand, the different ξ and η are free parameters for now, but in the next two sections, we will see how different symmetry-related constraints fix their values, leading to distinct PSG solutions.

Appendix C: U(1) PSG classification

The canonical form of a U(1) *Ansatz* is given by

$$u_{ij} = i\chi_{ij}^0 \tau^0 + \chi_{ij}^3 \tau^z. \quad (\text{C1})$$

The structure of the gauge transformations that keep this canonical form intact is given by

$$W_{\mathcal{O}}(\mathbf{r}, u) = F_3(\phi_{\mathcal{O}}(m, n, u))(i\tau^x)^{w_{\mathcal{O}}}, \quad (\text{C2})$$

where $\mathcal{O} \in \{T_x, T_y, G_x, \sigma_{xy}, \mathcal{T}\}$, and $w_{\mathcal{O}}$ can take values 0 or 1. Now, we will systematically work out the possibilities for $w_{\mathcal{O}}$ and $\phi_{\mathcal{O}}$ one by one for the different symmetries.

1. Space-group symmetries

First, let us analyze the solutions for the space-group symmetries of the Shastry-Sutherland lattice. Starting with translations, the relations (C2) for $\mathcal{O} \in \{T_x, T_y\}$ can be explicitly written as :

$$W_{T_x}(m, n, u) = F_3(\phi_{T_x}(m, n, u))(i\tau^x)^{w_{T_x}}, \quad (\text{C3})$$

$$W_{T_y}(m, n, u) = F_3(\phi_{T_y}(m, n, u))(i\tau^x)^{w_{T_y}}.$$

According as the values of $w_{T_x/y}$, three cases may arise :

$$1. w_{T_x} = 0, w_{T_y} = 0,$$

$$2. w_{T_x} = 1, w_{T_y} = 0,$$

$$3. w_{T_x} = 1, w_{T_y} = 1.$$

It is readily seen that cases 2 and 3 can be excluded as these do not satisfy the conditions (B1)(d-f). Hence, we need to only consider the first, and we call this choice the ‘‘uniform gauge’’. Now, we can always choose a gauge transformation with the form $W(m, n, u) = F_3(\theta(m, n, u))$ such that we end up with:

$$W_{T_x}(m, 0, u) = W_{T_y}(m, n, u) = \tau^0. \quad (\text{C4})$$

With these settings, inserting Eq. (C4) into the symmetry condition (B1)(a) leads to the solutions for *all* \mathbf{r} :

$$\begin{aligned} W_{T_x}(m, n, u) &= F_3(n\xi_y), \\ W_{T_y}(m, n, u) &= \tau^0. \end{aligned} \quad (\text{C5})$$

These two equations define the allowed projective actions of translational symmetries.

Next, we consider the glide symmetry. With the notation $\Delta_i\phi_{\mathcal{O}}(m, n, u) \equiv \phi_{\mathcal{O}}(m, n, u) - \phi_{\mathcal{O}}[T_i^{-1}(m, n, u)]$ for $i = x, y$, Eqs. (B1)(b, c) tell us that

$$\begin{aligned} \Delta_i\phi_{G_x}(m, n, u) &= \phi_{T_i}(m, n, u) \\ &+ (-1)^{w_{G_x}}(\xi_{G_x} - \phi_{T_i}[G_x^{-1}(m, n, u)]), \end{aligned} \quad (\text{C6})$$

which, upon substitution of ϕ_{T_i} from Eq. (C5), yields

$$\begin{aligned} \Delta_x\phi_{G_x}(m, n, u) &= (-1)^{w_{G_x}}\xi_{G_{xx}} + [n(1 + (-1)^{w_{G_x}})]\xi_y \\ &+ [(-1)^{w_{G_x}}(\delta_{u,3} + \delta_{u,4})]\xi_y, \\ \Delta_y\phi_{G_x}(m, n, u) &= (-1)^{w_{G_x}}\xi_{G_{xy}}. \end{aligned} \quad (\text{C7})$$

We also have to satisfy the additional consistency condition:

$$\begin{aligned} \Delta_x\phi_{G_x}(m, n, u) + \Delta_y\phi_{G_x}[T_x^{-1}(m, n, u)] \\ = \Delta_y\phi_{G_x}(m, n, u) + \Delta_x\phi_{G_x}[T_y^{-1}(m, n, u)], \end{aligned} \quad (\text{C8})$$

which enforces that

$$[1 + (-1)^{w_{G_x}}]\xi_y = 0. \quad (\text{C9})$$

Thus, $w_{G_x} = 0$ implies that $2\xi_y = 0$, while there is no restriction if $w_{G_x} = 1$. Consequently, we obtain the general solution

$$\begin{aligned} \phi_{G_x}(m, n, u) &= (-1)^{w_{G_x}}(m\xi_{G_{xx}} + n\xi_{G_{xy}}) \\ &+ (-1)^{w_{G_x}}m\xi_y(\delta_{u,3} + \delta_{u,4}) + \bar{\phi}_{G_x,u}, \end{aligned} \quad (\text{C10})$$

using the shorthand $\bar{\phi}_{G_x,u} \equiv \phi_{G_x}(0, 0, u)$. Once ϕ_{G_x} is determined, we can plug it back into Eq. (C2), together with the associated value of w_{G_x} , to obtain the set of PSG elements.

Having dealt with translation and glide symmetries, we now turn to the mirror symmetry σ_{xy} . The gauge transformations accompanying reflections once again have the general form

$$W_{\sigma_{xy}} = F_3(\phi_{\sigma_{xy}}(m, n, u))(i\tau^x)^{w_{\sigma_{xy}}}. \quad (\text{C11})$$

Using Eqs. (B1)(i) and (B1)(j), the relations analogous to Eq. (C7) above read as:

$$\begin{aligned} \Delta_x\phi_{\sigma_{xy}}(m, n, u) &= -(-1)^{w_{\sigma_{xy}}}\xi_{\sigma_{xy}T_x} + n\xi_y \\ \Delta_y\phi_{\sigma_{xy}}(m, n, u) &= -(-1)^{w_{\sigma_{xy}}}(\xi_{\sigma_{xy}T_y} + m\xi_y). \end{aligned} \quad (\text{C12})$$

However, unlike Eq. (C8), the corresponding consistency condition for σ_{xy} does not impose any further restrictions on ξ_y . The final solution for $W_{\phi_{\sigma_{xy}}}$ is given by

$$\begin{aligned} \phi_{\sigma_{xy}}(m, n, u) &= -(-1)^{w_{\sigma_{xy}}}(m\xi_{\sigma_{xy}T_x} + n\xi_{\sigma_{xy}T_y}) \\ &+ mn\xi_y + \bar{\phi}_{\sigma_{xy},u}, \end{aligned} \quad (\text{C13})$$

which we can put back into Eq. (C11) to determine $W_{\sigma_{xy}}$.

While Eqs. (C5), (C10), and (C13) provide the general solutions for $\phi_{\mathcal{O}}$, these may not be gauge independent. In fact, the U(1) phases derived above can be greatly simplified or fixed by the use of a local gauge transformation $W(m, n, u)$ under which

$$W_{\mathcal{O}}(m, n, u) \rightarrow W^\dagger(m, n, u)W_{\mathcal{O}}(m, n, u)W[\mathcal{O}^{-1}(m, n, u)].$$

To demonstrate this, let us choose a gauge transformation (which is independent of the sublattice index),

$$W(m, n, u) = F_3(m\theta_x + n\theta_y). \quad (\text{C14})$$

With the proper choices of θ_x and θ_y , one can then set

$$\begin{aligned} \xi_{\sigma_{xy}T_x} &= 0, \\ \text{for } w_{G_x} = 0: \xi_{G_{xy}} &= 0, \\ \text{for } w_{G_x} = 1: \xi_{G_{xx}} &= 0. \end{aligned} \quad (\text{C15})$$

Thereafter, using a sublattice-dependent gauge transformation $W(m, n, u) = F_3(\theta_u)$ with $\theta_2 = (-1)^{w_{G_x}}(\theta_1 - \bar{\phi}_{G_x,1})$, $\theta_3 = \bar{\phi}_{G_x,3} + (-1)^{w_{G_x}}\theta_4$, $\theta_4 = (-1)^{w_{\sigma_{xy}}}(\theta_2 - \bar{\phi}_{\sigma_{xy},2})$, we can fix the following:

$$\bar{\phi}_{G_x,1} = \bar{\phi}_{G_x,3} = \bar{\phi}_{\sigma_{xy},2} = 0 = \bar{\phi}_{\sigma_{xy},1}\delta_{w_{\sigma_{xy}},1}, \quad (\text{C16})$$

which drastically simplifies Eqs. (C10) and (C13).

Continuing in this spirit, we shall exploit the remaining conditions from Eq. (B1) to further fix the free parameters. For instance, using Eqs. (C15) and (C16), Eq. (B1)(d) yields

$$\begin{aligned} \text{for } w_{G_x} = 0: \xi_y &= \xi_{G_{xx}} = \xi_{G_{xy}} = 0, \\ \bar{\phi}_{G_x,2} &= \bar{\phi}_{G_x,4} = \xi_{G_xT_x}; \\ \text{for } w_{G_x} = 1: \xi_{G_{xx}} &= \xi_y + 2\xi_{G_{xy}} = 0, \\ \bar{\phi}_{G_x,2} &= n_{G_xT_x}\pi = \bar{\phi}_{G_x,4} + \xi_{G_{xy}}. \end{aligned} \quad (\text{C17})$$

Likewise, Eq. (B1)(h) asserts that

$$\xi_{\sigma_{xy}T_y} = 0, [1 + (-1)^{w_{\sigma_{xy}}}] \xi_y = 0, \quad (\text{C18})$$

$$\bar{\phi}_{\sigma_{xy},u} + (-1)^{w_{\sigma_{xy}}}\bar{\phi}_{\sigma_{xy},\sigma_{xy}(u)} = \xi_{\sigma_{xy}}. \quad (\text{C19})$$

Then, putting the content of Eq. (C16) into Eq. (C19), one arrives at the following result for $\bar{\phi}_{\sigma_{xy},u}$:

$$w_{\sigma_{xy}} = 0: \bar{\phi}_{\sigma_{xy},u} = \{\bar{\phi}_{\sigma_{xy}}, 0, \bar{\phi}_{\sigma_{xy}} + n_{\sigma_{xy}}\pi, 2\bar{\phi}_{\sigma_{xy}}\},$$

$$w_{\sigma_{xy}} = 1 : \bar{\phi}_{\sigma_{xy},u} = \{0, 0, \bar{\phi}_{\sigma_{xy}}, 0\}. \quad (\text{C20})$$

We are still left with one more lattice symmetry condition given by Eq. (B1)(g), which imposes further constraints in two cases:

$$(w_{G_x}, w_{\sigma_{xy}}) = (1, 0) : 2\xi_{G_{xy}} = 0 \implies \xi_y = 0, \quad (\text{C21})$$

$$(w_{G_x}, w_{\sigma_{xy}}) = (0, 1) : \bar{\phi}_{\sigma_{xy}} = 2\xi_{G_x T_x} + n_{\sigma_{xy}} \pi. \quad (\text{C22})$$

A simple gauge choice is possible for the case with $w_{G_x} = 0$ as follows⁸. Employing a gauge transformation of the form $W(m, n, u) = F_3(\theta_u)$ with $\theta_2 = \theta_1 + \xi_{G_x T_x}/2$ and $\theta_4 = \theta_3 + \xi_{G_x T_x}/2$, one can set

$$\bar{\phi}_{G_x, u} = \xi_{G_x T_x}/2 \implies \bar{\phi}_{G_x, u} = 0. \quad (\text{C23})$$

On the right-hand side above, we have used the gauge freedom which allows us to set a global U(1) phase to zero. Due to this gauge transformation, $\bar{\phi}_{\sigma_{xy}, u}$ will also necessarily be modified, but we can still exploit the freedom to choose θ_1 and θ_3 . For $w_{\sigma_{xy}} = 0$, choosing $\theta_3 = \theta_1 + \bar{\phi}_{\sigma_{xy}}$, we obtain

$$\begin{aligned} \bar{\phi}_{\sigma_{xy}, u} &= \{\bar{\phi}_{\sigma_{xy}}, \bar{\phi}_{\sigma_{xy}}, \bar{\phi}_{\sigma_{xy}} + n_{\sigma_{xy}} \pi, \bar{\phi}_{\sigma_{xy}}\}, \\ \implies \bar{\phi}_{\sigma_{xy}, u} &= \{0, 0, n_{\sigma_{xy}} \pi, 0\}. \end{aligned} \quad (\text{C24})$$

On the other hand, for $w_{\sigma_{xy}} = 1$, we choose $\theta_1 = 0$, $\theta_3 = -\xi_{G_x T_x}$, which leads to

$$\bar{\phi}_{\sigma_{xy}, u} = \{0, 0, \bar{\phi}_{\sigma_{xy}} + 2\xi_{G_x T_x}, 0\},$$

and, for simplicity, we will redefine $\bar{\phi}_{\sigma_{xy}} + 2\xi_{G_x T_x} \rightarrow \bar{\phi}_{\sigma_{xy}}$.

The upshot of this sequence of operations is that we have now specified all the values of $\bar{\phi}_{\mathcal{O}}$ and ξ_{\dots} that determine $\phi_{\mathcal{O}}$ for all space-group symmetries \mathcal{O} . In turn, $\phi_{\mathcal{O}}$ —together with different combinations of $w_{\mathcal{O}}$ —then feeds into Eq. (C2) and defines the PSGs.

2. Time-reversal symmetry

Per Eq. (C2), the gauge transformation associated with time reversal takes the form

$$W_{\mathcal{T}}(\mathbf{r}, u) = F_3(\phi_{\mathcal{T}}(m, n, u))(i\tau^x)^{w_{\mathcal{T}}}. \quad (\text{C25})$$

Following Eq. (B1)(j) for $\mathcal{O} \in \{T_x, T_y\}$, we find (for both $w_{\mathcal{T}} = 0$ and $w_{\mathcal{T}} = 1$) that

$$\phi_{\mathcal{T}}(m, n, u) = m \xi_{\mathcal{T}_x} + n \xi_{\mathcal{T}_y} + \bar{\phi}_{\mathcal{T}, u}. \quad (\text{C26})$$

As for Eq. (C8) earlier, the consistency condition yields

$$[1 - (-1)^{w_{\mathcal{T}}}] \xi_y = 0, \quad (\text{C27})$$

which implies that for $w_{\mathcal{T}} = 1$, $2\xi_y = 0$.

To fix the rest of the parameters, it is convenient to consider the two possible values of $w_{\mathcal{T}}$ separately.

⁸ No such uniform choice of $\bar{\phi}_{G_x, u}$ is possible for $w_{G_x} = 1$, so we will continue to use the existing gauge choice in that case.

$$a. \quad w_{\mathcal{T}} = 0$$

In this case, the symmetry relation (B1)(i) gives

$$2\xi_{\mathcal{T}_x} = 2\xi_{\mathcal{T}_y} = 0, \quad \bar{\phi}_{\mathcal{T}, u} = \bar{\phi}_{\mathcal{T}} + n_u \pi = n_u \pi, \quad (\text{C28})$$

where the gauge freedom can be utilized to set $\bar{\phi}_{\mathcal{T}} = 0$. Now, using the equation above and Eq. (B1)(j) for $\mathcal{O} = G_x, \sigma_{xy}$, one can fix:

$$\xi_{\mathcal{T}_x} = \xi_{\mathcal{T}_y} = 0. \quad (\text{C29})$$

Note that having an *Ansatz* with nonvanishing amplitudes on NN bonds requires that

$$\bar{\phi}_{\mathcal{T}, u} = u \pi. \quad (\text{C30})$$

However, since diagonal bonds connect sites with both even or odd values of the sublattice index u , this also implies that choosing such a gauge for time reversal results in vanishing *Ansätze* on the NNN bonds.

$$b. \quad w_{\mathcal{T}} = 1$$

When $w_{\mathcal{T}} = 1$, it is always possible to choose a gauge such that $\phi_{\mathcal{T}}(m, n, u) = 0$. The advantage of such a choice is that the mean-field parameters on all the bonds then comprise only real hopping terms.

Here, we demonstrate this process for the case of $w_{G_x} = w_{\sigma_{xy}} = 0$. First, we perform a gauge transformation given by,

$$W_{\mathcal{T}}(m, n, u) = F_3 \left(m \frac{\xi_{\mathcal{T}_x}}{2} + n \frac{\xi_{\mathcal{T}_y}}{2} + \frac{\bar{\phi}_{\mathcal{T}, u}}{2} \right). \quad (\text{C31})$$

This immediately sets

$$\phi_{\mathcal{T}}(m, n, u) \rightarrow \tilde{\phi}_{\mathcal{T}}(m, n, u) = 0. \quad (\text{C32})$$

The price we pay for this is that ϕ_{G_x} and ϕ_{σ} will also be modified simultaneously to

$$\begin{aligned} \tilde{\phi}_{G_x} &= -n \xi_{\mathcal{T}_y} + \frac{\bar{\phi}_{\mathcal{T}, 2} - \bar{\phi}_{\mathcal{T}, 1}}{2} (\delta_{u, 1} - \delta_{u, 2}) \\ &\quad + \frac{\bar{\phi}_{\mathcal{T}, 4} - \bar{\phi}_{\mathcal{T}, 3}}{2} (\delta_{u, 3} - \delta_{u, 4}) \\ &\quad - \frac{\xi_{\mathcal{T}_x}}{2} (\delta_{u, 1} + \delta_{u, 4}) - \frac{\xi_{\mathcal{T}_y}}{2} (\delta_{u, 3} + \delta_{u, 4}), \end{aligned} \quad (\text{C33})$$

$$\begin{aligned} \tilde{\phi}_{\sigma_{xy}} &= (n - m) \frac{\xi_{\mathcal{T}_x} - \xi_{\mathcal{T}_y}}{2} + p_{\sigma_{xy}} \pi \delta_{u, 3} \\ &\quad + \frac{\bar{\phi}_{\mathcal{T}, 4} - \bar{\phi}_{\mathcal{T}, 2}}{2} (\delta_{u, 2} - \delta_{u, 4}), \end{aligned} \quad (\text{C34})$$

with $p_{\sigma_{xy}} = 0, 1$. For notational convenience, we drop the tilde on ϕ hereafter.

Lastly, making use of Eq. (B1)(j) produces two other constraints:

$$\xi_{\mathcal{T}G_x} = -2\phi_{G_x}(m, n, u), \quad (\text{C35})$$

$$\xi_{\mathcal{T}\sigma_{xy}} = -2\phi_{\sigma_{xy}}(m, n, u), \quad (\text{C36})$$

leading to the relations:

$$2\xi_{\mathcal{T}y} = 0 \Rightarrow \xi_{\mathcal{T}y} = p_{G_{xy}}\pi, \quad (\text{C37})$$

$$\xi_{\mathcal{T}x} = \xi_{\mathcal{T}y} = p_{G_{xy}}\pi, \quad (\text{C38})$$

$$\bar{\phi}_{\mathcal{T},2} = \bar{\phi}_{\mathcal{T},4}, \quad \bar{\phi}_{\mathcal{T},1} = \bar{\phi}_{\mathcal{T},3}, \quad (\text{C39})$$

$$2(\bar{\phi}_{\mathcal{T},2} - \bar{\phi}_{\mathcal{T},1}) = p_{G_{xy}}\pi, \quad (\text{C40})$$

$$\Rightarrow \bar{\phi}_{\mathcal{T},2} = \bar{\phi}_{\mathcal{T},1} + \frac{p_{G_{xy}}\pi}{2} + p_{G_x T_x}\pi,$$

where both $p_{G_{xy}}$ and $p_{G_x T_x}$ take values 0 or 1. Combining these equations and performing an appropriate global phase shift, the end result is

$$\phi_{G_x}(m, n, u) = p_{G_{xy}}\pi(n + \delta_{u,4}) + p_{G_x T_x}\pi(\delta_{u,2} + \delta_{u,4}), \quad (\text{C41})$$

$$\phi_{\sigma_{xy}}(m, n, u) = p_{\sigma_{xy}}\pi\delta_{u,3}, \quad (\text{C42})$$

for the class $w_{G_x} = w_{\sigma_{xy}} = 0, w_{\mathcal{T}} = +1$.

The PSGs for the other classes can be straightforwardly worked out in the same manner. We summarize all the U(1) PSGs thus obtained in Eqs. (22)–(25) and Table II.

Appendix D: \mathbb{Z}_2 PSG classification

The PSGs for a \mathbb{Z}_2 IGG can be derived in similar fashion to the U(1) case. We proceed, as before, by considering the spatial and time-reversal symmetries separately.

1. Space-group symmetries

Exploiting the local gauge redundancy, we first fix:

$$W_{T_x}(m, 0, u) = W_{T_y}(m, n, u) = \tau^0. \quad (\text{D1})$$

With these settings, the symmetry condition (B1)(a) directly leads to the following solutions for the translational PSGs:

$$\begin{aligned} W_{T_x}(m, n, u) &= \eta_y^y \tau^0, \\ W_{T_y}(m, n, u) &= \tau^0, \end{aligned} \quad (\text{D2})$$

where η_y (and all other parameters η_{\dots} introduced hereafter) can be ± 1 .

Let us introduce the notation $\Omega_i[W_{\mathcal{O}}(m, n, u)] \equiv W_{\mathcal{O}}(m, n, u)W_{\mathcal{O}}[T_i^{-1}(m, n, u)]$ for $i = x, y$. In this language, after substituting Eq. (D2) into Eqs. (B1)(b, c),

we find

$$\begin{aligned} \Omega_x[W_{G_x}(m, n, u)] &= \eta_{G_{xx}}\eta_y^{-(\delta_{u,3}+\delta_{u,4})}\tau^0, \\ \Omega_y[W_{G_x}(m, n, u)] &= \eta_{G_{xy}}\tau^0. \end{aligned} \quad (\text{D3})$$

Akin to the U(1) case, we can identify a consistency equation as

$$\begin{aligned} \Omega_x[W_{G_x}(m, n, u)]\Omega_y[W_{G_x}[T_x^{-1}(m, n, u)]] &= \\ \Omega_y[W_{G_x}(m, n, u)]\Omega_x[W_{G_x}[T_y^{-1}(m, n, u)]]; \end{aligned} \quad (\text{D4})$$

however, this does not impose any new constraints. Relevantly, the solution for W_{G_x} takes the generic form:

$$W_{G_x}(m, n, u) = \eta_{G_{xx}}^m \eta_{G_{xy}}^n \eta_y^{-m(\delta_{u,3}+\delta_{u,4})} \mathcal{W}_{G_x, u}, \quad (\text{D5})$$

where $\mathcal{W}_{G_x, u}$ is a sublattice-dependent Pauli matrix in pseudospin space.

Likewise the solution for $W_{\sigma_{xy}}$ can be directly obtained from Eqs. (B1)(e, f) as

$$W_{\sigma_{xy}}(m, n, u) = \eta_{\sigma_{xy} T_x}^m \eta_{\sigma_{xy} T_y}^n \eta_y^{mn} \mathcal{W}_{\sigma_{xy}, u}. \quad (\text{D6})$$

Once again, we can try to simplify the PSG solutions by a clever choice of gauge transformations. Note that a local transformation of the form $W(m, n, u) = \eta_M^m \eta_N^n \tau^0$ does not impact the projective operation of translations. However, they do modify the spatial dependencies of $W_{\sigma_{xy}}$ and W_{G_x} . On choosing η_M and η_N appropriately, one can set

$$\eta_{\sigma_{xy} T_x} = +1. \quad (\text{D7})$$

Combining this with a sublattice-dependent gauge transformation of the form $W(m, n, u) = W_u$, we fix

$$\mathcal{W}_{G_x,1} = \mathcal{W}_{G_x,3} = \mathcal{W}_{\sigma_{xy},2} = \tau^0. \quad (\text{D8})$$

Then, using Eq. (D8) in Eq. (B1)(c), we find

$$\begin{aligned} \eta_y &= \eta_{G_{xx}} = 0, \\ \mathcal{W}_{G_x,2} &= \eta_{G_{xy}} \mathcal{W}_{G_x,4} = \eta_{G_x T_x}. \end{aligned} \quad (\text{D9})$$

At the same time, Eq. (B1)(h) gives

$$\eta_{\sigma_{xy} T_y} = +1, \quad \mathcal{W}_{\sigma_{xy}, u} \mathcal{W}_{\sigma_{xy}, \sigma_{xy}(u)} = \eta_{\sigma_{xy}} \tau^0. \quad (\text{D10})$$

In addition, we are left with one more lattice symmetry condition given by Eq. (B1). Using this together with the information from Eqs. (D8) and (D10), we obtain

$$\mathcal{W}_{\sigma_{xy}, u} = \begin{cases} \{\eta_{\sigma_{xy},1}\tau^0, \tau^0, \eta_{\sigma_{xy},3}\tau^0, \tau^0\}; & \text{for } \eta_{\sigma_{xy}} = +1 \\ \{i\tau^z, \tau^0, \eta_{\sigma_{xy},3}i\tau^z, -\tau^0\}; & \text{for } \eta_{\sigma_{xy}} = -1 \end{cases}. \quad (\text{D11})$$

At this point, yet another set of gauge transformations, defined by $W(m, n, u) = (\eta_{\sigma_{xy},1})^{(\delta_{u,1}+\delta_{u,2})}$ for $\eta_{\sigma_{xy}} = +1$ and $W(m, n, u) = (i\tau^z)^{(\delta_{u,3}+\delta_{u,4})}$ for $\eta_{\sigma_{xy}} = -1$, lead to

$$\mathcal{W}_{\sigma_{xy}, u} = \begin{cases} \{1, 1, \eta_{\sigma_{xy},3}\eta_{\sigma_{xy},1}, 1\}\eta_{\sigma_{xy},1}\tau^0; & \text{for } \eta_{\sigma_{xy}} = +1 \\ \{1, 1, \eta_{\sigma_{xy},3}, 1\}i\tau^z; & \text{for } \eta_{\sigma_{xy}} = -1 \end{cases}. \quad (\text{D12})$$

Now, by virtue of the IGG freedom, we can drop the global sign parameter $\eta_{\sigma_{xy},1}$ in the first case above. Furthermore, we define a new parameter $\eta_\sigma \equiv \eta_{\sigma_{xy},3}\eta_{\sigma_{xy},1}$ and $\eta_\sigma \equiv \eta_{\sigma_{xy},3}$ for $\eta_{\sigma_{xy}} = +1$ and $\eta_{\sigma_{xy}} = -1$, respectively. This results in the compact expression

$$\mathcal{W}_{\sigma_{xy},u} = (\eta_\sigma)^{\delta_{u,3}} \mathcal{W}_\sigma, \quad (\text{D13})$$

where $\mathcal{W}_\sigma = \tau^0 (i\tau^z)$ for positive (negative) $\eta_{\sigma_{xy}}$.

2. Time-reversal symmetry

To compute the PSG solutions for time reversal, we can again use Eq. (B1)(j) for $\mathcal{O} \in \{T_x, T_y\}$, which directly yields

$$W_{\mathcal{T}}(m, n, u) = \eta_{\mathcal{T}T_x}^m \eta_{\mathcal{T}T_y}^n \mathcal{W}_{\mathcal{T},u}. \quad (\text{D14})$$

It is easy to see that Eqs. (B1)(i,j) with $\mathcal{O} \in \{G_x, \sigma_{xy}\}$ will now introduce four extra conditions, namely,

$$\eta_{\mathcal{T}T_x} = \eta_{\mathcal{T}T_y}, \quad (\text{D15a})$$

$$\mathcal{W}_{\mathcal{T},u}^2 = \eta_{\mathcal{T}}, \quad (\text{D15b})$$

$$\mathcal{W}_{\mathcal{T},u} \mathcal{W}_{\sigma_{xy},u} = \eta_{\sigma_{xy}} \mathcal{T} \mathcal{W}_{\sigma_{xy},u} \mathcal{W}_{\mathcal{T},\sigma_{xy}^{-1}(u)}, \quad (\text{D15c})$$

$$\mathcal{W}_{\mathcal{T},u} \mathcal{W}_{G_x,u} = \eta_{G_x} \mathcal{T} \eta_{\mathcal{T}T_x}^{(u \bmod 2)} \mathcal{W}_{G_x,u} \mathcal{W}_{\mathcal{T},G_x^{-1}(u)}. \quad (\text{D15d})$$

A summary of all the \mathbb{Z}_2 PSGs constructed from these relations is provided by Eqs. (26)–(29) and Table III.

Appendix E: Mapping to square-lattice PSGs

As discussed in Sec. IV C, the square-lattice wallpaper group, $p4m$, can be generated from that of the Shastry-Sutherland lattice, $p4g$, by incorporating the symmetry σ_x of reflections about the x -axis. This imposes certain additional symmetry relations, which are as follows:

$$\sigma_x^{-1} T_x^{-1} \sigma_x T_x = \mathbb{1}, \quad (\text{E1a})$$

$$\sigma_x^{-1} T_y^{-1} \sigma_x T_y = \mathbb{1}, \quad (\text{E1b})$$

$$G_x^{-1} \sigma_x G_x \sigma_x = \mathbb{1}, \quad (\text{E1c})$$

$$(\sigma_x \sigma_{xy})^4 = \mathbb{1}, \quad (\text{E1d})$$

$$\sigma_x^2 = \mathbb{1}, \quad (\text{E1e})$$

$$(\sigma_{xy} \sigma_x^{-1} G_x^{-1})^2 (\sigma_{xy} G_x \sigma_x)^2 = \mathbb{1}, \quad (\text{E1f})$$

$$(\sigma_x G_x \sigma_{xy} \sigma_x \sigma_{xy})^2 = \mathbb{1}, \quad (\text{E1g})$$

$$\mathcal{T} \sigma_x \mathcal{T}^{-1} \sigma_x^{-1} = \mathbb{1}. \quad (\text{E1h})$$

Using this information, we can now deduce the PSGs for the enlarged space group which includes σ_x . For example, from Eqs. (E1a) and (E1b), we find the projective implementation

$$W_{\sigma_x}(m, n, u) = \eta_{\sigma_x T_x}^m \eta_{\sigma_x T_y}^n \mathcal{W}_{\sigma_x,u}. \quad (\text{E2})$$

Similarly, the rest of the relations in Eq. (E1) can be harnessed to impose further constraints such as $\eta_{\sigma_x T_x} = \eta_{\sigma_x T_y} = +1$ in the solution above, as well as $\eta_{G_{xy}} = +1$ in Eq. (27). Systematically considering all the gauge-equivalent choices of $\mathcal{W}_{\sigma_x,u}$ that satisfy these symmetry constraints, we are led from the PSGs listed in Table III to the set in Table XII. Note that there are four η parameters and a total of 17 rows in the table. Thus, the total number of PSGs for the $p4m$ symmetry group is $2^4 \times 17 = 272$; this is indeed the number of PSGs enumerated in the square-lattice classification by Wen [56].

To illustrate the one-to-one mapping between each row of Table XII and the PSG structure obtained in Ref. [56], we need to rewrite the PSGs in terms of the projective realization of $\{T_1, T_2, \sigma_x, \sigma_y, \sigma_{xy}\}$ ⁹ and \mathcal{T} . As T_1, T_2 , and σ_y can be generated using only G_x, σ_x , and σ_{xy} , the projective extensions $W_{T_1}(m, n, u)$, $W_{T_2}(m, n, u)$ and $W_{\sigma_y}(m, n, u)$ can be derived using $W_{G_x}(m, n, u)$, $W_{\sigma_x}(m, n, u)$, and $W_{\sigma_{xy}}(m, n, u)$. Recalling the relations compiled in Eq. (42), we write the corresponding projective realizations as

$$W_{T_1}(m, n, u) = \eta_{T_1} W_{G_x}(m, n, u) W_{\sigma_x} [G_x^{-1}(m, n, u)], \quad (\text{E3})$$

$$W_{T_2}(m, n, u) = \eta_{T_2} W_{\sigma_{xy}}(m, n, u) W_{T_1} [\sigma_{xy}(m, n, u)] W_{\sigma_{xy}} [T_1^{-1} \sigma_{xy}(m, n, u)], \quad (\text{E4})$$

$$W_{\sigma_y}(m, n, u) = \eta_{\sigma_y} W_{\sigma_{xy}}(m, n, u) W_{\sigma_x} [\sigma_{xy}(m, n, u)] W_{\sigma_{xy}} [\sigma_x^{-1} \sigma_{xy}(m, n, u)]. \quad (\text{E5})$$

Note that the global sign parameters η_{T_1} , η_{T_2} , and η_{σ_y} can be set to +1 using the gauge freedom. This results in the solution:

$$W_{T_1}(m, n, u) = \{\eta_{\sigma_x G_x}, \eta_{G_x T_x}, \eta_{\sigma_x G_x}, \eta_{G_x T_x}\} \mathcal{W}_{T_1}, \quad (\text{E6})$$

$$W_{T_2}(m, n, u) = \{\eta_{\sigma_x G_x}, \eta_\sigma \eta_{G_x T_x}, \eta_\sigma \eta_{\sigma_x G_x}, \eta_{G_x T_x}\} \mathcal{W}_{T_2}, \quad (\text{E7})$$

$$W_{\sigma_y}(m, n, u) = \{1, \eta_{\sigma_x G_x}, 1, \eta_{\sigma_x G_x}\} \mathcal{W}_{\sigma_y}, \quad (\text{E8})$$

$$W_{\sigma_x}(m, n, u) = \{1, \eta_{\sigma_x G_x}, 1, \eta_{\sigma_x G_x}\} \mathcal{W}_{\sigma_x}, \quad (\text{E9})$$

$$W_{\sigma_{xy}}(m, n, u) = \{1, 1, \eta_\sigma, 1\} \mathcal{W}_{\sigma_{xy}}, \quad (\text{E10})$$

$$W_{\mathcal{T}}(m, n, u) = \{1, \eta_{G_x \mathcal{T}}, 1, \eta_{G_x \mathcal{T}}\} \mathcal{W}_{\mathcal{T}}. \quad (\text{E11})$$

The associated matrices \mathcal{W} are listed in Table XIII.

To simplify these expressions even further, we can now implement a gauge transformation with $W(m, n, u) = (\eta_{\sigma_x G_x} \eta_{G_x T_x})^{m+n} \{\eta_{\sigma_x G_x} \eta_{G_x T_x}, \eta_{\sigma_x G_x}, \eta_\sigma, \eta_{\sigma_x G_x}\}$, which brings us to

$$W_{T_1}(m, n, u) = \{1, 1, \eta_\sigma, \eta_\sigma\} \mathcal{W}_{T_1}, \quad (\text{E12})$$

⁹ In Ref. [56], $\sigma_x, \sigma_y, \sigma_{xy}$ are denoted as P_y, P_x and P_{xy} , respectively.

PSG No.	$\mathcal{W}_{\sigma_{xy},u}$	$\mathcal{W}_{\mathcal{T},u}$	$\mathcal{W}_{\sigma_x,u}$
1(a)	$\{\tau^0, \tau^0, \eta_\sigma \tau^0, \tau^0\}$	$\{\tau^0, \eta_{G_x} \tau \tau^0, \tau^0, \eta_{G_x} \tau \tau^0\}$	$\{\tau^0, \eta_{\sigma_x G_x} \tau^0, \tau^0, \eta_{\sigma_x G_x} \tau^0\}$
1(b)	$\{\tau^0, \tau^0, \eta_\sigma \tau^0, \tau^0\}$	$\{\tau^0, \eta_{G_x} \tau \tau^0, \tau^0, \eta_{G_x} \tau \tau^0\}$	$\{i\tau^z, \eta_{\sigma_x G_x} i\tau^z, i\tau^z, \eta_{\sigma_x G_x} i\tau^z\}$
2(a)	$\{\tau^0, \tau^0, \eta_\sigma \tau^0, \tau^0\}$	$\{i\tau^y, \eta_{G_x} \tau i\tau^y, i\tau^y, \eta_{G_x} \tau i\tau^y\}$	$\{\tau^0, \eta_{\sigma_x G_x} \tau^0, \tau^0, \eta_{\sigma_x G_x} \tau^0\}$
2(b)	$\{\tau^0, \tau^0, \eta_\sigma \tau^0, \tau^0\}$	$\{i\tau^y, \eta_{G_x} \tau i\tau^y, i\tau^y, \eta_{G_x} \tau i\tau^y\}$	$\{i\tau^z, \eta_{\sigma_x G_x} i\tau^z, i\tau^z, \eta_{\sigma_x G_x} i\tau^z\}$
2(c)	$\{\tau^0, \tau^0, \eta_\sigma \tau^0, \tau^0\}$	$\{i\tau^y, \eta_{G_x} \tau i\tau^y, i\tau^y, \eta_{G_x} \tau i\tau^y\}$	$\{i\tau^y, \eta_{\sigma_x G_x} i\tau^y, i\tau^y, \eta_{\sigma_x G_x} i\tau^y\}$
3(a)	$\{i\tau^z, i\tau^z, \eta_\sigma i\tau^z, i\tau^z\}$	$\{i\tau^y, \eta_{G_x} \tau i\tau^y, i\tau^y, \eta_{G_x} \tau i\tau^y\}$	$\{\tau^0, \eta_{\sigma_x G_x} \tau^0, \tau^0, \eta_{\sigma_x G_x} \tau^0\}$
3(b)	$\{i\tau^z, i\tau^z, \eta_\sigma i\tau^z, i\tau^z\}$	$\{i\tau^y, \eta_{G_x} \tau i\tau^y, i\tau^y, \eta_{G_x} \tau i\tau^y\}$	$\{i\tau^z, \eta_{\sigma_x G_x} i\tau^z, i\tau^z, \eta_{\sigma_x G_x} i\tau^z\}$
3(c)	$\{i\tau^z, i\tau^z, \eta_\sigma i\tau^z, i\tau^z\}$	$\{i\tau^y, \eta_{G_x} \tau i\tau^y, i\tau^y, \eta_{G_x} \tau i\tau^y\}$	$\{i\tau^y, \eta_{\sigma_x G_x} i\tau^y, i\tau^y, \eta_{\sigma_x G_x} i\tau^y\}$
3(d)	$\{i\tau^z, i\tau^z, \eta_\sigma i\tau^z, i\tau^z\}$	$\{i\tau^y, \eta_{G_x} \tau i\tau^y, i\tau^y, \eta_{G_x} \tau i\tau^y\}$	$\{i\tau^x, \eta_{\sigma_x G_x} i\tau^x, i\tau^x, \eta_{\sigma_x G_x} i\tau^x\}$
3(e)	$\{i\tau^z, i\tau^z, \eta_\sigma i\tau^z, i\tau^z\}$	$\{i\tau^y, \eta_{G_x} \tau i\tau^y, i\tau^y, \eta_{G_x} \tau i\tau^y\}$	$\{i\tau^{zx}, \eta_{\sigma_x G_x} i\tau^{zx}, i\tau^{zx}, \eta_{\sigma_x G_x} i\tau^{zx}\}$
4(a)	$\{i\tau^z, i\tau^z, \eta_\sigma i\tau^z, i\tau^z\}$	$\{i\tau^z, \eta_{G_x} \tau i\tau^z, i\tau^z, \eta_{G_x} \tau i\tau^z\}$	$\{\tau^0, \eta_{\sigma_x G_x} \tau^0, \tau^0, \eta_{\sigma_x G_x} \tau^0\}$
4(b)	$\{i\tau^z, i\tau^z, \eta_\sigma i\tau^z, i\tau^z\}$	$\{i\tau^z, \eta_{G_x} \tau i\tau^z, i\tau^z, \eta_{G_x} \tau i\tau^z\}$	$\{i\tau^z, \eta_{\sigma_x G_x} i\tau^z, i\tau^z, \eta_{\sigma_x G_x} i\tau^z\}$
4(c)	$\{i\tau^z, i\tau^z, \eta_\sigma i\tau^z, i\tau^z\}$	$\{i\tau^z, \eta_{G_x} \tau i\tau^z, i\tau^z, \eta_{G_x} \tau i\tau^z\}$	$\{i\tau^y, \eta_{\sigma_x G_x} i\tau^y, i\tau^y, \eta_{\sigma_x G_x} i\tau^y\}$
5(a)	$\{i\tau^z, i\tau^z, \eta_\sigma i\tau^z, i\tau^z\}$	$\{\tau^0, \eta_{G_x} \tau \tau^0, \tau^0, \eta_{G_x} \tau \tau^0\}$	$\{\tau^0, \eta_{\sigma_x G_x} \tau^0, \tau^0, \eta_{\sigma_x G_x} \tau^0\}$
5(b)	$\{i\tau^z, i\tau^z, \eta_\sigma i\tau^z, i\tau^z\}$	$\{\tau^0, \eta_{G_x} \tau \tau^0, \tau^0, \eta_{G_x} \tau \tau^0\}$	$\{i\tau^z, \eta_{\sigma_x G_x} i\tau^z, i\tau^z, \eta_{\sigma_x G_x} i\tau^z\}$
5(c)	$\{i\tau^z, i\tau^z, \eta_\sigma i\tau^z, i\tau^z\}$	$\{\tau^0, \eta_{G_x} \tau \tau^0, \tau^0, \eta_{G_x} \tau \tau^0\}$	$\{i\tau^y, \eta_{\sigma_x G_x} i\tau^y, i\tau^y, \eta_{\sigma_x G_x} i\tau^y\}$
5(d)	$\{i\tau^z, i\tau^z, \eta_\sigma i\tau^z, i\tau^z\}$	$\{\tau^0, \eta_{G_x} \tau \tau^0, \tau^0, \eta_{G_x} \tau \tau^0\}$	$\{i\tau^{zx}, \eta_{\sigma_x G_x} i\tau^{zx}, i\tau^{zx}, \eta_{\sigma_x G_x} i\tau^{zx}\}$

TABLE XII. All gauge-inequivalent PSGs corresponding to the full $p4m$ space-group symmetry. The choices of $\mathcal{W}_{G_x,u}$ are the same for each row and are given by $\mathcal{W}_{G_x,u} = \{\tau^0, \eta_{G_x T_x} \tau^0, \tau^0, \eta_{G_x T_x} \tau^0\}$. Here, τ^{zx} is to be read as $\tau^{zx} \equiv (\tau^z + \tau^x)/\sqrt{2}$.

PSG No.	\mathcal{W}_{T_1}	\mathcal{W}_{T_2}	\mathcal{W}_{σ_y}	\mathcal{W}_{σ_x}	$\mathcal{W}_{\sigma_{xy}}$	$\mathcal{W}_{\mathcal{T}}$
1(a)	τ^0	τ^0	τ^0	τ^0	τ^0	τ^0
1(b)	$i\tau^z$	$i\tau^z$	$i\tau^z$	$i\tau^z$	τ^0	τ^0
2(a)	τ^0	τ^0	τ^0	τ^0	τ^0	$i\tau^y$
2(b)	$i\tau^z$	$i\tau^z$	$i\tau^z$	$i\tau^z$	τ^0	$i\tau^y$
2(c)	$i\tau^y$	$i\tau^y$	$i\tau^y$	$i\tau^y$	τ^0	$i\tau^y$
3(a)	τ^0	τ^0	τ^0	τ^0	$i\tau^z$	$i\tau^y$
3(b)	$i\tau^z$	$i\tau^z$	$i\tau^z$	$i\tau^z$	$i\tau^z$	$i\tau^y$
3(c)	$i\tau^y$	$i\tau^y$	$i\tau^y$	$i\tau^y$	$i\tau^z$	$i\tau^y$
3(d)	$i\tau^x$	$i\tau^x$	$i\tau^x$	$i\tau^x$	$i\tau^z$	$i\tau^y$
3(e)	$i\tau^{zx}$	$i\tau^{z\bar{x}}$	$i\tau^{z\bar{x}}$	$i\tau^{zx}$	$i\tau^z$	$i\tau^y$
4(a)	τ^0	τ^0	τ^0	τ^0	$i\tau^z$	$i\tau^z$
4(b)	$i\tau^z$	$i\tau^z$	$i\tau^z$	$i\tau^z$	$i\tau^z$	$i\tau^z$
4(c)	$i\tau^y$	$i\tau^y$	$i\tau^y$	$i\tau^y$	$i\tau^z$	$i\tau^z$
5(a)	τ^0	τ^0	τ^0	τ^0	$i\tau^z$	τ^0
5(b)	$i\tau^z$	$i\tau^z$	$i\tau^z$	$i\tau^z$	$i\tau^z$	τ^0
5(c)	$i\tau^y$	$i\tau^y$	$i\tau^y$	$i\tau^y$	$i\tau^z$	τ^0
5(d)	$i\tau^{zx}$	$i\tau^{z\bar{x}}$	$i\tau^{z\bar{x}}$	$i\tau^{zx}$	$i\tau^z$	τ^0

TABLE XIII. The same PSGs as enlisted in Table XII, but recast in terms of the symmetry group $\{T_1, T_2, \sigma_x, \sigma_y, \sigma_{xy}, \mathcal{T}\}$ [see Eqs. (E6)-(E11)]. $\tau^{z\bar{x}}$ is to be read as $\tau^{z\bar{x}} \equiv (\tau^z - \tau^x)/\sqrt{2}$.

$$W_{T_2}(m, n, u) = \mathcal{W}_{T_2}, \quad (\text{E13})$$

$$W_{\sigma_y}(m, n, u) = \{1, \eta_{G_x T_x}, \eta_{G_x T_x} \eta_{\sigma_x G_x}, \eta_{\sigma_x G_x}\} \mathcal{W}_{\sigma_y}, \quad (\text{E14})$$

PSG No.	\mathcal{W}_{σ_y}	\mathcal{W}_{σ_x}	$\mathcal{W}_{\sigma_{xy}}$	$\mathcal{W}_{\mathcal{T}}$	\mathcal{W}_{σ_y}	\mathcal{W}_{σ_x}	$\mathcal{W}_{\sigma_{xy}}$	$\mathcal{W}_{\mathcal{T}}$
1(a)	τ^0	τ^0	τ^0	τ^0	τ^0	τ^0	τ^0	τ^0
1(b)	$i\tau^z$	$i\tau^z$	τ^0	τ^0	$i\tau^z$	$i\tau^z$	τ^0	τ^0
2(a)	τ^0	τ^0	τ^0	$i\tau^y$	τ^0	τ^0	τ^0	$i\tau^z$
2(b)	$i\tau^z$	$i\tau^z$	τ^0	$i\tau^y$	$i\tau^x$	$i\tau^x$	τ^0	$i\tau^z$
2(c)	$i\tau^y$	$i\tau^y$	τ^0	$i\tau^y$	$i\tau^z$	$i\tau^z$	τ^0	$i\tau^z$
3(a)	τ^0	τ^0	$i\tau^z$	$i\tau^y$	τ^0	τ^0	$i\tau^x$	$i\tau^z$
3(b)	$i\tau^z$	$i\tau^z$	$i\tau^z$	$i\tau^y$	$i\tau^x$	$i\tau^x$	$i\tau^x$	$i\tau^z$
3(c)	$i\tau^y$	$i\tau^y$	$i\tau^z$	$i\tau^y$	$i\tau^z$	$i\tau^z$	$i\tau^x$	$i\tau^z$
3(d)	$i\tau^x$	$i\tau^x$	$i\tau^z$	$i\tau^y$	$i\tau^y$	$i\tau^y$	$i\tau^x$	$i\tau^z$
3(e)	$i\tau^{z\bar{x}}$	$i\tau^{zx}$	$i\tau^z$	$i\tau^y$	$i\tau^1$	$i\tau^y$	$i\tau^{xy}$	$i\tau^z$
4(a)	τ^0	τ^0	$i\tau^z$	$i\tau^z$	τ^0	τ^0	$i\tau^z$	$i\tau^z$
4(b)	$i\tau^z$	$i\tau^z$	$i\tau^z$	$i\tau^z$	$i\tau^z$	$i\tau^z$	$i\tau^z$	$i\tau^z$
4(c)	$i\tau^y$	$i\tau^y$	$i\tau^z$	$i\tau^z$	$i\tau^x$	$i\tau^x$	$i\tau^z$	$i\tau^z$
5(a)	τ^0	τ^0	$i\tau^z$	τ^0	τ^0	τ^0	$i\tau^z$	τ^0
5(b)	$i\tau^z$	$i\tau^z$	$i\tau^z$	τ^0	$i\tau^z$	$i\tau^z$	$i\tau^z$	τ^0
5(c)	$i\tau^y$	$i\tau^y$	$i\tau^z$	τ^0	$i\tau^x$	$i\tau^x$	$i\tau^z$	τ^0
5(d)	$i\tau^{z\bar{x}}$	$i\tau^{zx}$	$i\tau^z$	τ^0	$i\tau^1$	$i\tau^y$	$i\tau^{xy}$	τ^0

TABLE XIV. List of PSGs written in the square-lattice notation of Eq. (E24). We define $\tau^{xy} \equiv (\tau^x + \tau^y)/\sqrt{2}$ and $\tau^{x\bar{y}} \equiv (\tau^x - \tau^y)/\sqrt{2}$. On the right side, we present the solutions in a different gauge, which is the same as the one used in Ref. [56].

$$W_{\sigma_x}(m, n, u) = \{1, \eta_{\sigma_x G_x}, \eta_{G_x T_x} \eta_{\sigma_x G_x}, \eta_{G_x T_x}\} \mathcal{W}_{\sigma_x}, \quad (\text{E15})$$

$$W_{\sigma_{xy}}(m, n, u) = \{1, 1, \eta_\sigma, 1\} \mathcal{W}_{\sigma_{xy}}, \quad (\text{E16})$$

$$W_{\mathcal{T}}(m, n, u) = \{1, \eta_{G_x \mathcal{T}}, 1, \eta_{G_x \mathcal{T}}\} \mathcal{W}_{\mathcal{T}}. \quad (\text{E17})$$

The square lattice, of course, has only one site per unit cell, so the solutions above can be reformulated in the simple (x, y) coordinate system as

$$W_{T_1}(x, y) = \eta_{\sigma}^y \mathcal{W}_{T_1}, \quad (\text{E18})$$

$$W_{T_2}(x, y) = \mathcal{W}_{T_2}, \quad (\text{E19})$$

$$W_{\sigma_y}(x, y) = \eta_{G_x T_x}^x \eta_{\sigma_x G_x}^y \mathcal{W}_{\sigma_y}, \quad (\text{E20})$$

$$W_{\sigma_x}(x, y) = \eta_{\sigma_x G_x}^x \eta_{G_x T_x}^y \mathcal{W}_{\sigma_x}, \quad (\text{E21})$$

$$W_{\sigma_{xy}}(x, y) = \eta_{\sigma}^{xy} \mathcal{W}_{\sigma_{xy}}, \quad (\text{E22})$$

$$W_{\mathcal{T}}(x, y) = \eta_{G_x \mathcal{T}}^{x+y} \mathcal{W}_{\mathcal{T}}. \quad (\text{E23})$$

Additionally, one can conveniently set $\mathcal{W}_{T_1} = \mathcal{W}_{T_2} = \tau^0$ by applying a gauge transformation of the form $W(x, y) = \mathcal{W}_{T_2}^y \mathcal{W}_{T_1}^x$. This will not change the overall structure of the solutions in Table XIII up to a sign factor, which can be absorbed either using the gauge freedom (if it is global) or by redefining the parameters η . As an example, for $\mathcal{W}_{T_1} = i\tau^{zx} = i(\tau^z + \tau^1)/\sqrt{2}$, $W_{T_1}(x, y)$ and $W_{\sigma_{xy}}(x, y)$ in Eqs. (E18) and (E22), respectively, become $\mathcal{W}_{T_1} = (-\eta_{\sigma})^y$ and $W_{\sigma_{xy}}(x, y) = (-\eta_{\sigma})^{xy} \mathcal{W}_{\sigma_{xy}}$. The original x, y dependence can be recovered by the redefinition $\eta_{\sigma} \rightarrow -\eta_{\sigma}$.

After all these steps, we arrive at the full solution for the square-lattice PSGs, which read

$$W_{T_1}(x, y) = \eta_{\sigma}^y, \quad (\text{E24a})$$

$$W_{T_2}(x, y) = \tau^0, \quad (\text{E24b})$$

$$W_{\sigma_y}(x, y) = \eta_{G_x T_x}^x \eta_{\sigma_x G_x}^y \mathcal{W}_{\sigma_y}, \quad (\text{E24c})$$

$$W_{\sigma_x}(x, y) = \eta_{\sigma_x G_x}^x \eta_{G_x T_x}^y \mathcal{W}_{\sigma_x}, \quad (\text{E24d})$$

$$W_{\sigma_{xy}}(x, y) = \eta_{\sigma}^{xy} \mathcal{W}_{\sigma_{xy}}, \quad (\text{E24e})$$

$$W_{\mathcal{T}}(x, y) = \eta_{G_x \mathcal{T}}^{x+y} \mathcal{W}_{\mathcal{T}}, \quad (\text{E24f})$$

with the \mathcal{W} matrices noted on the left side in Table XIV. On the right side of the same table, we write these matrices in a different gauge, used in Ref. [56]. This completes the mapping of projective realizations of the symmetries from the SSM to those of the square lattice.

Appendix F: Properties of U(1) and \mathbb{Z}_2 *Ansätze*

The properties of an *Ansatz*—such as its spinon excitation spectrum, the dynamical structure factor, and the equal-time structure factor—depend on the choices of the mean-field parameters, which, in principle, should be evaluated self-consistently based on specific models. Here, we take a different approach and concentrate on more generic properties rather than focusing on a particular model.

In the canonical gauge, any U(1) *Ansatz* consists of solely hopping terms, so the pseudospin \uparrow and \downarrow sectors

are decoupled. Working in the basis defined by $\hat{f}_{\mathbf{k},\alpha} = (\hat{f}_{\mathbf{k},1,\alpha}, \hat{f}_{\mathbf{k},2,\alpha}, \hat{f}_{\mathbf{k},3,\alpha}, \hat{f}_{\mathbf{k},4,\alpha})^T$, the quadratic Hamiltonian in \mathbf{k} -space reads

$$\hat{H}(\mathbf{k}) = \sum_{\alpha=\uparrow,\downarrow} \hat{f}_{\mathbf{k},\alpha}^{\dagger} \hat{H}_{\mathbf{k}}^{\text{U}(1)} \hat{f}_{\mathbf{k},\alpha}. \quad (\text{F1})$$

Owing to spinon number conservation, the chemical potential does not need to be explicitly considered and can be ignored here. The one-particle-per-site constraint (on average) is enforced by setting the Fermi energy such that we are at half filling.

In the following, we summarize the generic spinon excitation characteristics of different U(1) *Ansätze*, which are illustrated in the top panel of Fig. 26. The band structures are plotted along the path $\Gamma \rightarrow X \rightarrow M \rightarrow \Gamma$, where the high-symmetry points are $\Gamma(0, 0)$, $X(\pi/2, 0)$, and $M(\pi/2, \pi/2)$ in the first Brillouin zone.

- The excitation spectrum for U100 is quadratic and gapless at the Γ point, while U1 π 0 exhibits quadratic gapless excitations at isolated \mathbf{k} -points. The spectrum of U10 π consists of Dirac cones located at $(\pm\pi/2, \pm\pi/2)$, as also seen for the SU(2) Dirac spin liquid labeled as SU2B n 0 on the square lattice [56]. U1 $\pi\pi$ features a Fermi surface with linear gapless excitations along $(k_x, -k_x)$ and $(k_x, k_x \pm \pi/2)$, forming Dirac nodal lines.
- The spectrum of U300 is gapless with a linear dispersion, and Dirac cones are observed along the \overline{XM} and \overline{YM} lines. A Fermi surface is seen for $\chi_d < 1.5\chi_s$. U3 π 0 has a gapped spinon spectrum. The link fields of U30 π and U3 $\pi\pi$ are the same as those of U10 π and U1 $\pi\pi$, respectively. However, the former states include a staggered chemical potential that opens up a gap. Notably, the staggered chemical potential also opens a gap for U300.
- The excitation spectrum of U500 is quadratic and gapless along $(k_x, \pm k_x)$, forming nodal lines. For U50 π , the spectrum is also gapless but linearly dispersing, forming a Dirac nodal loop surrounding the Γ or M point.
- The U8 ξ 0 family encompasses a series of *Ansätze* corresponding to different choices of $\xi = \mathcal{P}\pi/\mathcal{Q}$, for $\mathcal{P}, \mathcal{Q} \in \mathbb{Z}$. Here, we limit our analysis to states realizable within a single unit cell, which includes $\xi = 0$ and $\xi = \pi$. Both cases exhibit a Dirac dispersion. For $\xi = 0$, the Dirac cones are anchored at the Γ point, while for $\xi = \pi$, they reside at all high-symmetry points.

Next, we discuss the excitation spectra of the \mathbb{Z}_2 *Ansätze*. In this case, the interpretation of the quasiparticles is quite different from that for a U(1) IGG because spinon number conservation is lost due to the presence of

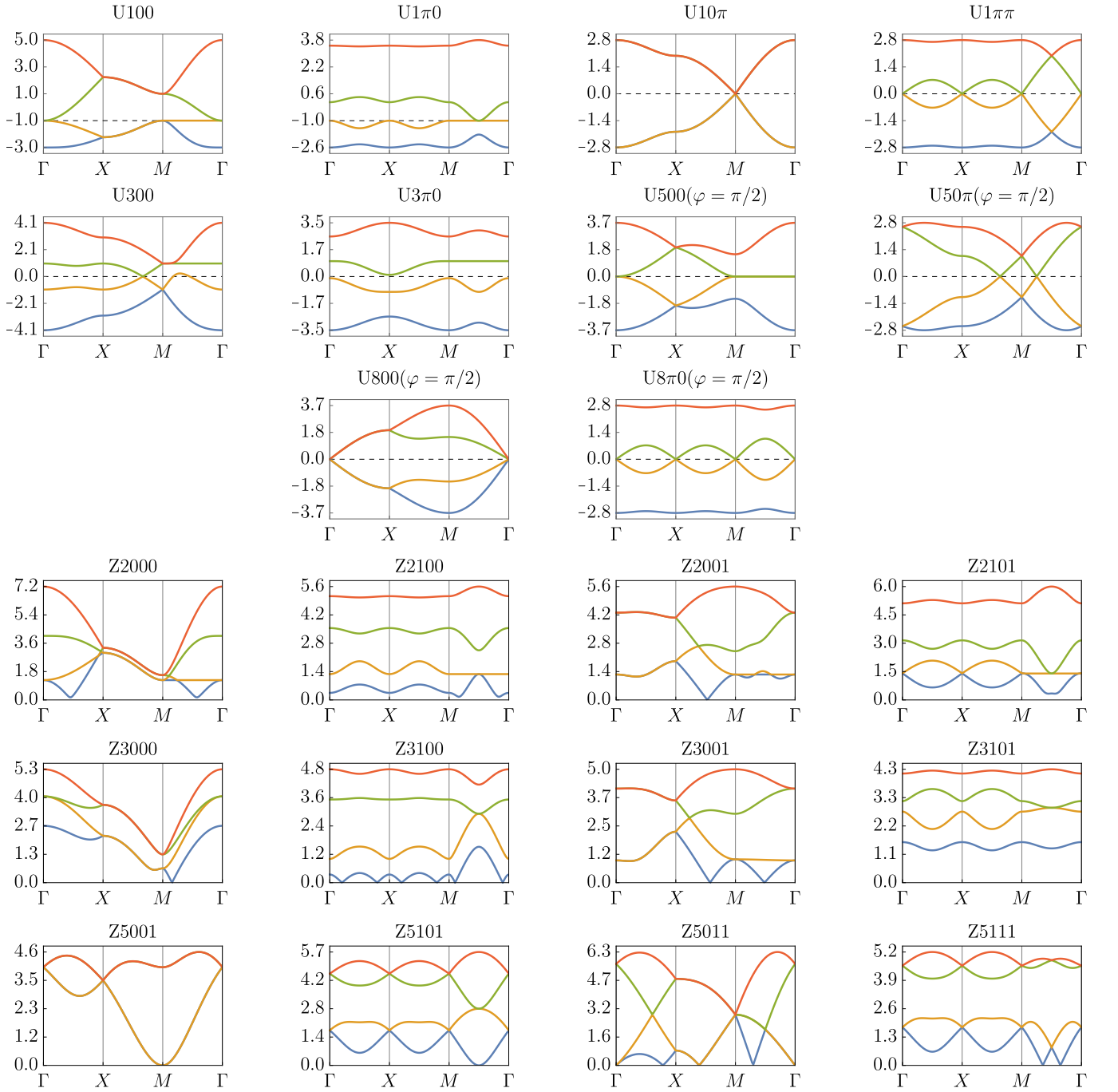


FIG. 26. Spinon band structures for all the U(1) *Ansätze* illustrated in Fig. 9 (top), and for the Z_2 *Ansätze* listed in Table IV (bottom). In both cases, we pick the mean-field parameters such that the magnitude of the symmetry-allowed hoppings is set to one. The dashed black line marks the Fermi level. For the U(1) *Ansätze* with both imaginary and real hoppings, we define a parameter $\varphi = \text{Arg}[u_s^4]$, which is related to the flux threading the square plaquettes (see Fig. 9).

pairing terms. We begin with the generic Bogoliubov-de Gennes (BdG) basis

$$\hat{\Psi}_{\mathbf{k}}^\dagger = (\hat{f}_{\mathbf{k},\uparrow}^\dagger, (\hat{f}_{-\mathbf{k},\downarrow})^T), \quad (\text{F2})$$

using which, any general mean-field Hamiltonian in \mathbf{k} -

space can be expressed as

$$\hat{H}(\mathbf{k}) = \hat{\Psi}_{\mathbf{k}}^\dagger \hat{H}_{\mathbf{k}}^{\text{BdG}} \hat{\Psi}_{\mathbf{k}}; \quad \hat{H}_{\mathbf{k}}^{\text{BdG}} = \begin{bmatrix} \hat{H}_{\mathbf{k}}^{\text{U}(1)} & \hat{H}_{\mathbf{k}}^{\text{Z}_2} \\ (\hat{H}_{\mathbf{k}}^{\text{Z}_2})^\dagger & -\hat{H}_{-\mathbf{k}}^{\text{U}(1)} \end{bmatrix}, \quad (\text{F3})$$

where $\hat{H}_{\mathbf{k}}^{\text{U}(1)}$ and $\hat{H}_{\mathbf{k}}^{\text{Z}_2}$ denote the hopping and pairing

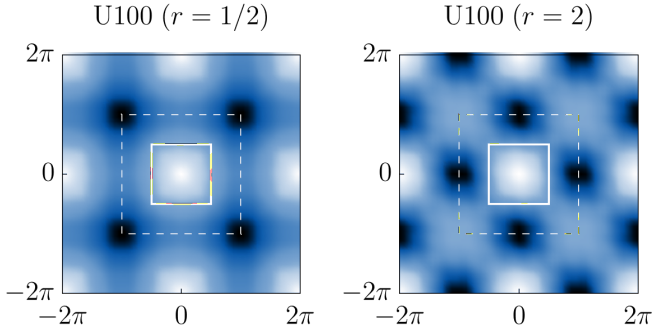


FIG. 27. Equal-time structure factor for the U100 state. r denotes the ratio of the hopping amplitude on the diagonals to that on the square bonds. Note that the structure factors for $r = 1/2$ and $r = 2$ show the same signatures as for Néel and stripe magnetic ordering on the square lattice, respectively. This property holds for all the U(1) and \mathbb{Z}_2 *Ansätze* with nonvanishing parameters on both the square and diagonal bonds. The solid (dashed) white square marks the first (extended) Brillouin zone.

terms in the *Ansatz*, respectively. The superscript \mathbb{Z}_2 indicates that these terms are the ones responsible for breaking the IGG down to \mathbb{Z}_2 .

Upon diagonalization, $\hat{H}_{\mathbf{k}}^{\text{BdG}}$ yields eigenvalues in positive and negative pairs, i.e., $\pm\epsilon_{\mathbf{k},u}$. In the diagonalized basis, $\hat{f}_{\mathbf{k},u,\alpha} \rightarrow \hat{\zeta}_{\mathbf{k},u,\alpha}$, the Hamiltonian can be rewritten as

$$\begin{aligned} \hat{H}(\mathbf{k}) &= \sum_{u=1}^4 \epsilon_{\mathbf{k},u} (\hat{\zeta}_{\mathbf{k},u,\uparrow}^\dagger \hat{\zeta}_{\mathbf{k},u,\uparrow} - \hat{\zeta}_{\mathbf{k},u,\downarrow} \hat{\zeta}_{\mathbf{k},u,\downarrow}^\dagger) \\ &= \sum_{u=1}^4 \sum_{\alpha=\uparrow,\downarrow} \epsilon_{\mathbf{k},u} (\hat{\zeta}_{\mathbf{k},u,\alpha}^\dagger \hat{\zeta}_{\mathbf{k},u,\alpha} - 1). \end{aligned} \quad (\text{F4})$$

This formulation allows us to interpret the spinon excitations of a generic symmetric \mathbb{Z}_2 mean-field *Ansatz* as Bogoliubov quasiparticles that always have a positive energy. In other words, the Fermi level lies at zero energy, leaving the quasiparticle-free ground state as the vacuum. In this case, the explicit inclusion of Lagrange multipliers is required to enforce the one-particle-per-site constraint on average.

In the second half of Fig. 26, we showcase the spinon dispersion spectra for the \mathbb{Z}_2 *Ansätze* listed in Table IV. For purposes of illustration, all mean-field parameters are set to unity. The general properties of these states are as follows:

- For Z2000, the chemical potential $\mu \neq 0$ (required to satisfy the constraint) opens up a small gap in general. Both Z2100 and Z2101 are also generically gapped. The spectrum of Z2001 always exhibits a Dirac dispersion with a Dirac cone positioned between the X and M points.
- Similarly to Z2001, Z3000 hosts a Dirac dispersion, with a Dirac cone located between Γ and M . Z3100

shows a gapless spectrum with either a Fermi surface or Dirac cones, depending on the mean-field parameters. The spectrum of Z3001 generally features a Fermi surface surrounding the M points, or a Dirac dispersion for specific parameter choices. Z3101 can exhibit gapped, Dirac, or Fermi-surface states.

- Within the Z5 class, Z5101, Z5011, and Z5111 exhibit gapless dispersions with a Fermi surface, while Z5001 has a quadratic dispersion that becomes gapless at the M point.
- For the remaining six *Ansätze* (Z2011, Z2111, Z3010, Z3110, Z3011, Z3111), the term breaking the IGG from U(1) to \mathbb{Z}_2 is the onsite piece $\mu\tau^z$. The link fields retain the original U(1) flux structures, leading these *Ansätze* to qualitatively resemble their parent U(1) states.

To distinguish and further characterize these states, we can calculate their respective structure factors, which are also of utility for comparisons to neutron scattering experiments. The longitudinal component (which suffices due to spin-rotation symmetry) of the equal-time spin-spin correlation defines the equal-time spin structure factor as

$$\mathcal{S}(\mathbf{q}) = \frac{1}{\mathcal{N}} \sum_{i,j} e^{i\mathbf{q}\cdot\mathbf{r}_{ij}} \langle \hat{S}_i^z \hat{S}_j^z \rangle, \quad (\text{F5})$$

where $\sqrt{\mathcal{N}}$ is the number of lattice sites. In Fig. 27, we show the equal-time structure factor of the U(1) state labeled U100 for two choices of parameters: $r = 1/2$ and $r = 2$, where r is the ratio of mean-field amplitudes on the diagonal and square bonds. With stronger square bonds, maxima appear at the $M'(\pi, \pi)$ points in the extended Brillouin zone (EBZ), while for dominant diagonal bonds, the maxima occur at $X'(\pi, 0)$. These maxima are not sharp Bragg peaks due to spin-rotational symmetry but instead form a continuum. This qualitative behavior persists across all U(1) and \mathbb{Z}_2 *Ansätze* with nonzero mean-field parameters on both square and diagonal bonds. For *Ansätze* with vanishing diagonal parameters, the maxima always appear at M' .

For representative parameter choices (consistent with the dispersion plots in Fig. 26), the equal-time structure factors of all the U(1) and \mathbb{Z}_2 *Ansätze* are shown in Fig. 28. While most states exhibit minimal qualitative differences in their equal-time structure factor, the distinctions are clearer in the dynamical structure factor (DSF), defined as

$$\mathcal{S}(\mathbf{q}, \omega) = \int_{-\infty}^{+\infty} \frac{d\tau e^{i\omega\tau}}{2\pi\mathcal{N}} \sum_{i,j} e^{i\mathbf{q}\cdot\mathbf{r}_{ij}} \langle \hat{S}_i^z(\tau) \hat{S}_j^z(0) \rangle. \quad (\text{F6})$$

The DSFs are plotted for the various *Ansätze* along the high-symmetry path $\Gamma(0,0) \rightarrow X'(\pi,0) \rightarrow M'(\pi,\pi) \rightarrow \Gamma$ in the EBZ in Fig. 29.

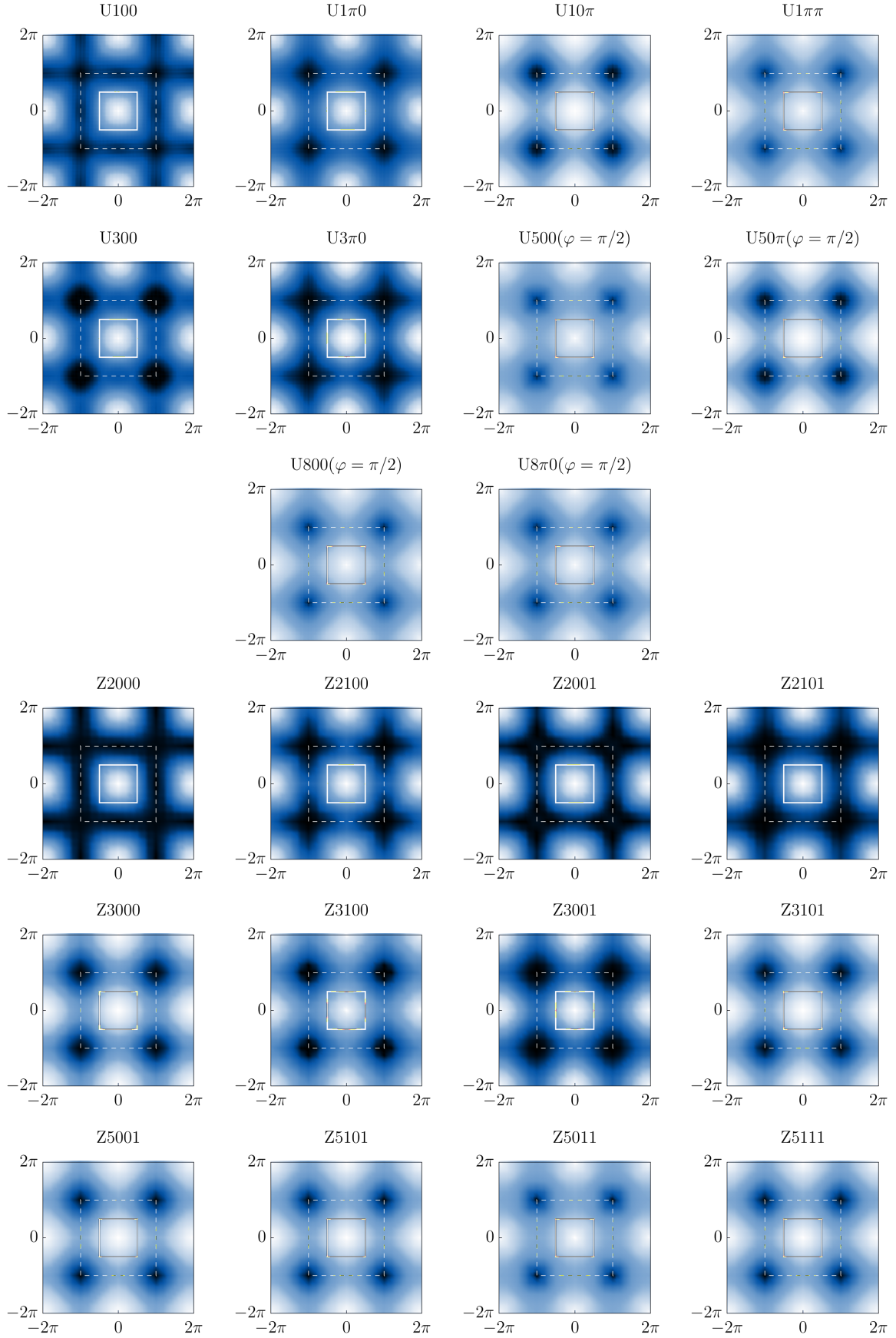


FIG. 28. Equal-time structure factors for all the $U(1)$ *Ansätze* illustrated in Fig. 9 (top), and for the Z_2 *Ansätze* listed in Table IV (bottom), following the same conventions for the color map as in Fig. 27. The mean-field parameters are the same as those used for Fig. 26.

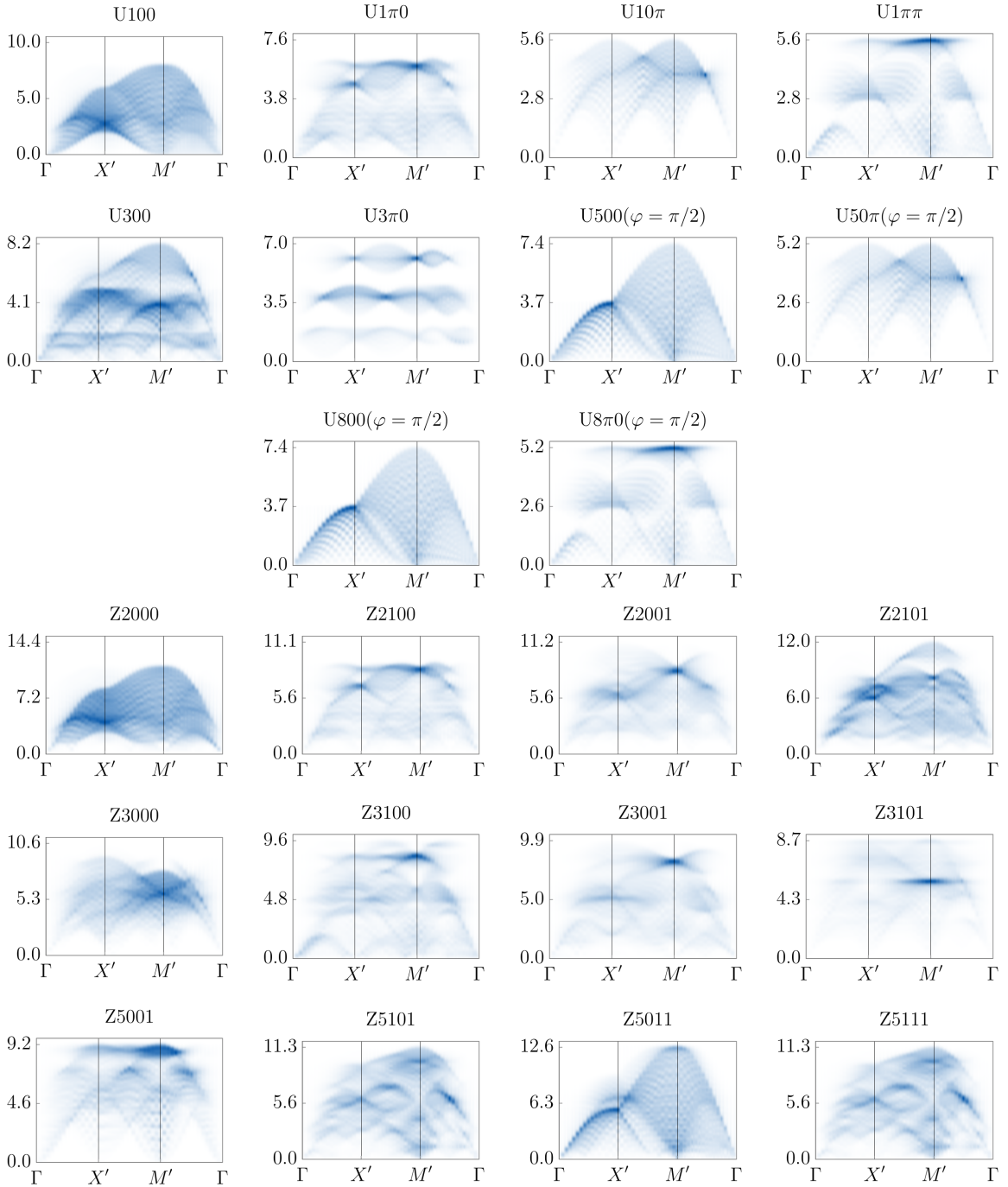


FIG. 29. Dynamical structure factors for all the $U(1)$ *Ansätze* illustrated in Fig. 9 (top), and for the Z_2 *Ansätze* listed in Table IV (bottom). The variation in intensity from low to high is conveyed by the gradient of the color, from white to blue (similar to Fig. 19). The mean-field parameters are the same as those used for Fig. 26.

In addition, it is also instructive to comment on the dispersion of the Z3000 state when all diagonal terms are included, namely χ_d , $\chi_{d'}$, χ_\square , and Δ_\square , since this is the key *Ansatz* considered in the present study. As discussed in the main text, the inclusion of any of these terms leads to a splitting of the Dirac nodes. In Fig. 30, we present contour plots of the lowest-energy eigenmode

of the Z3000 state as a function of the variational parameters. Notably, for all parameter choices explored, the Dirac nodes remain located along the $\overline{\Gamma M}$ line in momentum space. Moreover, the dependence of the Dirac-node positions on the variational parameters is illustrated explicitly in Fig. 31.

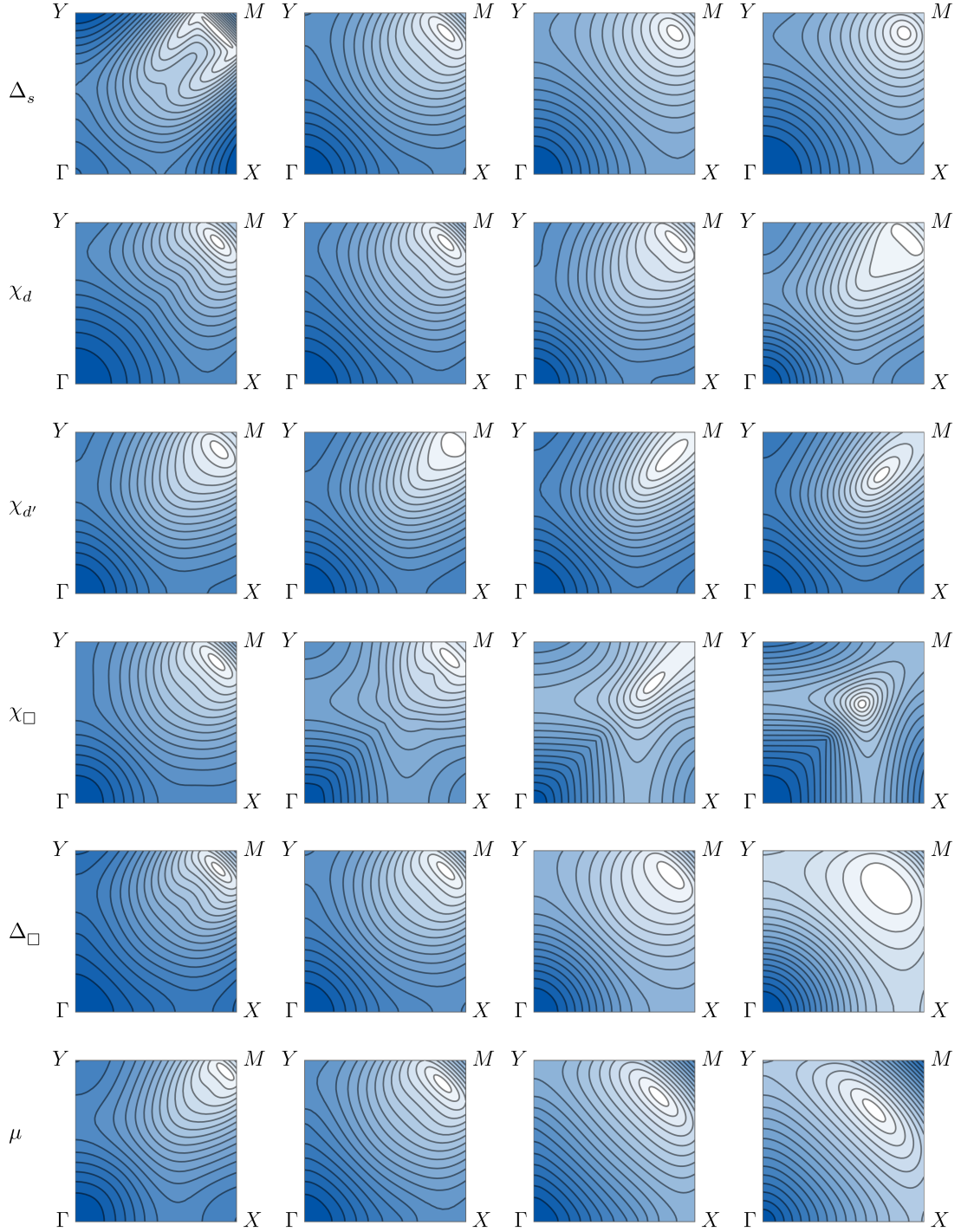


FIG. 30. Contour plots of the lowest-energy mode of the Z3000 *Ansatz*, illustrating the positions of the Dirac points as the variational parameters are varied. In each row, the parameter indicated on the left (Δ_s , χ_d , $\chi_{d'}$, χ_{\square} , Δ_{\square} , and μ) is varied, while the remaining parameters are fixed at their optimized VMC values. The four columns correspond to parameter values 0.2, 0.4, 0.6, and 0.8, respectively. The hopping amplitude χ_s is fixed to $\chi_s = 1.0$ throughout. The color scheme is the same as that used in Fig. 12. The corresponding dispersion curves along the $\Gamma \rightarrow M$ direction are shown in Fig. 31.

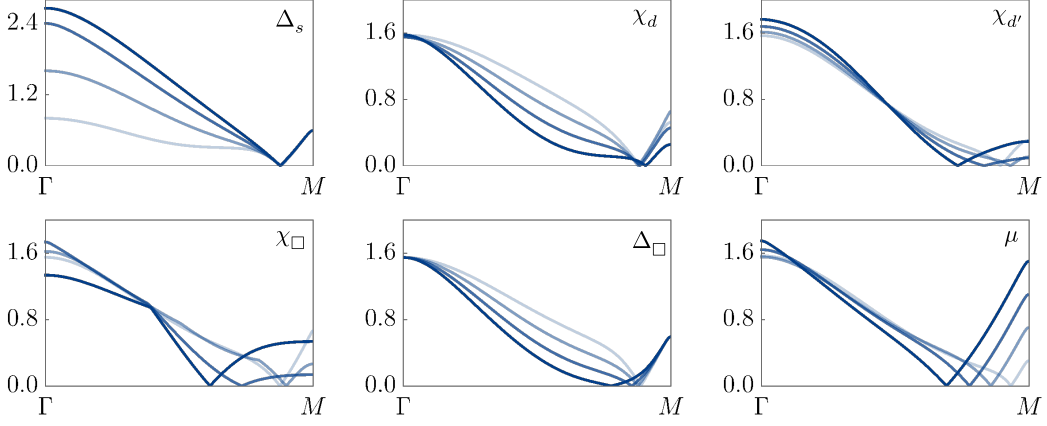


FIG. 31. Dispersion of the lowest-energy mode of the Z3000 *Ansatz*, illustrating the positions of the Dirac points as the variational parameters are varied. The initial parameters are set by the optimized values obtained from VMC, and small variations are introduced around these values for Δ_s , χ_d , $\chi_{d'}$, χ_{\square} , Δ_{\square} , and μ . The hopping amplitude χ_s is fixed to $\chi_s = 1.0$ throughout. In each panel, the opacity of the curves encodes the magnitude of the corresponding parameter, with lower (higher) opacity representing smaller (larger) parameter values.

Appendix G: PSGs for plaquette VBCs

So far, we have focused exclusively on symmetric QSLs in our discussion. However, in order to describe the dimerization of our fully symmetric QSLs into the neighboring plaquette VBC phase reported for $J_s/J_d \lesssim 0.78$ [32, 42, 43, 46, 116, 132, 133], we now also perform a classification of QSLs with a lower symmetry, namely, that of the plaquette VBC. This enables us to construct fermionic mean-field states for plaquette VBCs that descend from their parent fully symmetric QSLs thereby allowing us to describe transitions between QSLs and plaquette VBCs. In particular, our goal is to identify the plaquette VBC *Ansatz* that is continuously connected to the Z3000 state.

Realizing a plaquette VBC on the empty squares of the Shastry-Sutherland lattice (as observed in numerical studies) imprints a different symmetry group on the system: this order requires breaking both G_x and σ_{xy} , but preserving the fourfold rotational, C_4 , symmetry. Hence, the modified symmetry group is given by $\{T_x, T_y, C_4, \mathcal{T}\}$. The symmetry relations analogous to Eq. (18) are

$$T_x^{-1} T_y^{-1} T_x T_y = \mathbb{1}, \quad (\text{G1})$$

$$T_y C_4^{-1} T_x C_4 = \mathbb{1}, \quad (\text{G2})$$

$$T_x^{-1} C_4^{-1} T_y C_4 = \mathbb{1}, \quad (\text{G3})$$

$$C_4^4 = \mathcal{T}^2 = \mathbb{1}, \quad (\text{G4})$$

$$\mathcal{T} \mathcal{O} \mathcal{T}^{-1} \mathcal{O}^{-1} = \mathbb{1}. \quad (\text{G5})$$

For concreteness, we consider the center of an empty square (which the C_4 axis passes through) as the origin of the coordinate system, and the square itself is taken to be the new reference unit cell; see Fig. 32. The coordinates of the four sites (indexed by u) within the unit cell are given by $1(-a/2, a/2)$, $2(-a/2, -a/2)$, $3(a/2, -a/2)$, and

$4(a/2, a/2)$. Now, we introduce the sublattice-dependent coordinate system (X, Y, u) , akin to Eq. (15) earlier. Under the present symmetry group elements, (X, Y, u) transforms as

$$T_x : (X, Y, u) \rightarrow (X + 1, Y, u), \quad (\text{G6})$$

$$T_y : (X, Y, u) \rightarrow (X, Y + 1, u), \quad (\text{G7})$$

$$C_4 : (X, Y, u) \rightarrow (-Y, X, C_4(u)), \quad (\text{G8})$$

where $C_4(\{1, 2, 3, 4\}) = \{2, 3, 4, 1\}$.

Following the same prescription as in Appendix D, we can obtain the solutions of the algebraic PSGs:

$$W_{T_x}(X, Y, u) = \eta_y^Y \tau^0, \quad W_{T_y}(X, Y, u) = \tau^0, \quad (\text{G9})$$

$$W_{C_4}(X, Y, u) = \eta_{C_4 y}^Y \eta_y^{XY} \mathcal{W}_{C_4, u}, \quad (\text{G10})$$

$$W_{\mathcal{T}}(X, Y, u) = \eta_{\mathcal{T}}^{X+Y} \eta_{\mathcal{T} C_4}^u \mathcal{W}_{\mathcal{T}}. \quad (\text{G11})$$

Here, $\mathcal{W}_{C_4, u} = \{\tau^0, \tau^0, \tau^0, \eta_{C_4} \tau^0\}$, and the matrix $\mathcal{W}_{\mathcal{T}}$ can be either τ^0 or $i\tau^y$. Each of the five parameters $\{\eta_y, \eta_{C_4}, \eta_{C_4 y}, \eta_{\mathcal{T}}, \eta_{\mathcal{T} C_4}\}$ take values ± 1 , so together with the two options for $\mathcal{W}_{\mathcal{T}}$, we find a total of 64 algebraic PSGs. However, for $\mathcal{W}_{\mathcal{T}} = \tau^0$, the solution with $\eta_{\mathcal{T}} = \eta_{\mathcal{T} C_4} = +1$ has to be excluded as the mean-field parameters trivially vanish on all the bonds. Therefore, we are left with 56 PSGs. The corresponding symmetry-allowed mean-field parameters are documented in Table XV. Note that since we restrict ourselves to short-range *Ansätze* with only NN and NNN bonds, only 48 of the 56 PSGs lead to QSL states with IGG \mathbb{Z}_2 . The remaining eight (P22A, P22B, P23A, P23B, P26A, P26B, P27A, and P27B) carry a U(1) IGG since the pairing terms identically vanish up to the neighbors we considered. In Table XV, each row corresponds to two *Ansätze*, one with $\eta_y = +1$ (class A) and the other with $\eta_y = -1$ (class B). Realization of the class-B *Ansätze* requires dou-

Label	$\{\eta_y, \eta_{C_4}, \eta_{C_4y}, \eta_T, \eta_{TC_4}\}$	\mathcal{W}_T	u_s	u'_s	u_d	$u_{d'}$	u_\square	$u_{\square'}$	Onsite
P1A/B	$\{\eta_y, +, +, +, +\}$	$i\tau^y$	$\tau^{z,x}$	$\tau^{z,x}$	$\tau^{z,x}$	$\tau^{z,x}$	$\tau^{z,x}$	$\tau^{z,x}$	$\tau^{z,x}$
P2A/B	$\{\eta_y, +, -, +, +\}$	$i\tau^y$	$\tau^{z,x}$	$\tau^{z,x}$	0	0	0	0	$\tau^{z,x}$
P3A/B	$\{\eta_y, -, +, +, +\}$	$i\tau^y$	$\tau^{z,x}$	$\tau^{z,x}$	0	0	$\tau^{z,x}$	0	$\tau^{z,x}$
P4A/B	$\{\eta_y, -, -, +, +\}$	$i\tau^y$	$\tau^{z,x}$	$\tau^{z,x}$	$\tau^{z,x}$	$\tau^{z,x}$	0	$\tau^{z,x}$	$\tau^{z,x}$
P5A/B	$\{\eta_y, +, +, +, -\}$	$i\tau^y$	$\tau^{0,y}$	$\tau^{0,y}$	$\tau^{z,x}$	$\tau^{z,x}$	$\tau^{z,x}$	$\tau^{z,x}$	$\tau^{z,x}$
P6A/B	$\{\eta_y, +, -, +, -\}$	$i\tau^y$	$\tau^{0,y}$	$\tau^{0,y}$	0	0	0	0	$\tau^{z,x}$
P7A/B	$\{\eta_y, -, +, +, -\}$	$i\tau^y$	$\tau^{0,y}$	$\tau^{0,y}$	0	0	$\tau^{z,x}$	0	$\tau^{z,x}$
P8A/B	$\{\eta_y, -, -, +, -\}$	$i\tau^y$	$\tau^{0,y}$	$\tau^{0,y}$	$\tau^{z,x}$	$\tau^{z,x}$	0	$\tau^{z,x}$	$\tau^{z,x}$
P9A/B	$\{\eta_y, +, +, -, +\}$	$i\tau^y$	$\tau^{z,x}$	$\tau^{0,y}$	τ^y	τ^y	$\tau^{z,x}$	$\tau^{z,x}$	$\tau^{z,x}$
P10A/B	$\{\eta_y, +, -, -, +\}$	$i\tau^y$	$\tau^{z,x}$	$\tau^{0,y}$	τ^0	τ^0	0	0	$\tau^{z,x}$
P11A/B	$\{\eta_y, -, +, -, +\}$	$i\tau^y$	$\tau^{z,x}$	$\tau^{0,y}$	τ^0	τ^0	$\tau^{z,x}$	0	$\tau^{z,x}$
P12A/B	$\{\eta_y, -, -, -, +\}$	$i\tau^y$	$\tau^{z,x}$	$\tau^{0,y}$	τ^y	τ^y	0	$\tau^{z,x}$	$\tau^{z,x}$
P13A/B	$\{\eta_y, +, +, -, -\}$	$i\tau^y$	$\tau^{0,y}$	$\tau^{z,x}$	τ^y	τ^y	$\tau^{z,x}$	$\tau^{z,x}$	$\tau^{z,x}$
P14A/B	$\{\eta_y, +, -, -, -\}$	$i\tau^y$	$\tau^{0,y}$	$\tau^{z,x}$	τ^0	τ^0	0	0	$\tau^{z,x}$
P15A/B	$\{\eta_y, -, +, -, -\}$	$i\tau^y$	$\tau^{0,y}$	$\tau^{z,x}$	τ^0	τ^0	$\tau^{z,x}$	0	$\tau^{z,x}$
P16A/B	$\{\eta_y, -, -, -, -\}$	$i\tau^y$	$\tau^{0,y}$	$\tau^{z,x}$	τ^y	τ^y	0	$\tau^{z,x}$	$\tau^{z,x}$
P17A/B	$\{\eta_y, +, +, +, -\}$	τ^0	$\tau^{0,z}$	$\tau^{0,x,z}$	0	0	0	0	0
P18A/B	$\{\eta_y, +, -, +, -\}$	τ^0	$\tau^{0,z}$	$\tau^{0,x,z}$	0	0	0	0	0
P19A/B	$\{\eta_y, -, +, +, -\}$	τ^0	$\tau^{0,z}$	$\tau^{0,x,z}$	0	0	0	0	0
P20A/B	$\{\eta_y, -, -, +, -\}$	τ^0	$\tau^{0,z}$	$\tau^{0,x,z}$	0	0	0	0	0
P21A/B	$\{\eta_y, +, +, -, +\}$	τ^0	0	$\tau^{0,z}$	$\tau^{x,z}$	$\tau^{x,y,z}$	0	0	0
P22A/B	$\{\eta_y, +, -, -, +\}$	τ^0	0	$\tau^{0,z}$	τ^0	τ^0	0	0	0
P23A/B	$\{\eta_y, -, +, -, +\}$	τ^0	0	$\tau^{0,z}$	τ^0	τ^0	0	0	0
P24A/B	$\{\eta_y, -, -, -, +\}$	τ^0	0	$\tau^{0,z}$	$\tau^{x,z}$	$\tau^{x,y,z}$	0	0	0
P25A/B	$\{\eta_y, +, +, -, -\}$	τ^0	$\tau^{0,z}$	0	$\tau^{x,z}$	$\tau^{x,y,z}$	0	0	0
P26A/B	$\{\eta_y, +, -, -, -\}$	τ^0	$\tau^{0,z}$	0	τ^0	τ^0	0	0	0
P27A/B	$\{\eta_y, -, +, -, -\}$	τ^0	$\tau^{0,z}$	0	τ^0	τ^0	0	0	0
P28A/B	$\{\eta_y, -, -, -, -\}$	τ^0	$\tau^{0,z}$	0	$\tau^{x,z}$	$\tau^{x,y,z}$	0	0	0

TABLE XV. Mean-field parameters on the reference bonds, u_s , u'_s , u_d , $u_{d'}$, u_\square and $u_{\square'}$ for all possible *Ansätze* taking only translations, C_4 , and time-reversal symmetries into account. Each row stands for two *Ansätze* labeled by classes A ($\eta_y = +1$) and B ($\eta_y = -1$). All the *Ansätze* besides P22A, P22B, P23A, P23B, P26A, P26B, P27A, and P27B correspond to a \mathbb{Z}_2 IGG.

bling of the unit cell along the x -axis. The detailed sign structures of these *Ansätze* are illustrated in Fig. 32.

Among the *Ansätze* compiled in Table XV, the *Ansatz* labelled by P5A is a descendant of Z3000 when breaking σ_{xy} and G_x while preserving C_4 . Although this connection is not immediately apparent in the listed form, one can recast this *Ansatz* in terms of real hopping and pairing amplitudes using a gauge transformation $W(X, Y, u) = (-1)^{(\delta_{u,1} + \delta_{u,4})} (i\tau^z)^{(\delta_{u,2} + \delta_{u,4})}$ as follows:

$$\begin{aligned}
\hat{\mathcal{H}}_{\text{MF}}^{\text{P5A}} = & \sum_i \left[\mu \sum_\alpha \hat{f}_{i,\alpha}^\dagger \hat{f}_{i,\alpha} + \Delta (-1)^i (\hat{f}_{i,\uparrow}^\dagger \hat{f}_{i,\downarrow}^\dagger + \text{h.c.}) \right] \\
& + \sum_{(ij) \text{ light blue}} \left[\chi_s \sum_\alpha s_{ij}^s \hat{f}_{i,\alpha}^\dagger \hat{f}_{j,\alpha} + \Delta_s \nu_{ij}^s (\hat{f}_{i,\uparrow}^\dagger \hat{f}_{j,\downarrow}^\dagger + \text{h.c.}) \right] \\
& + \sum_{(ij) \text{ dark blue}} \left[\chi_{s'} \sum_\alpha s_{ij}^{s'} \hat{f}_{i,\alpha}^\dagger \hat{f}_{j,\alpha} + \Delta_{s'} \nu_{ij}^{s'} (\hat{f}_{i,\uparrow}^\dagger \hat{f}_{j,\downarrow}^\dagger + \text{h.c.}) \right]
\end{aligned}$$

$$\begin{aligned}
& + \sum_{(ij) \text{ teal}} \left[\chi_d \sum_\alpha s_{ij}^d \hat{f}_{i,\alpha}^\dagger \hat{f}_{j,\alpha} + \Delta_d \nu_{ij}^d (\hat{f}_{i,\uparrow}^\dagger \hat{f}_{j,\downarrow}^\dagger + \text{h.c.}) \right] \\
& + \sum_{(ij) \text{ orange}} \left[\chi_{d'} \sum_\alpha s_{ij}^{d'} \hat{f}_{i,\alpha}^\dagger \hat{f}_{j,\alpha} + \Delta_{d'} \nu_{ij}^{d'} (\hat{f}_{i,\uparrow}^\dagger \hat{f}_{j,\downarrow}^\dagger + \text{h.c.}) \right] \\
& + \sum_{(ij) \text{ light green}} \left[\chi_\square \sum_\alpha s_{ij}^\square \hat{f}_{i,\alpha}^\dagger \hat{f}_{j,\alpha} + \Delta_\square \nu_{ij}^\square (\hat{f}_{i,\uparrow}^\dagger \hat{f}_{j,\downarrow}^\dagger + \text{h.c.}) \right] \\
& + \sum_{(ij) \text{ dark green}} \left[\chi_{\square'} \sum_\alpha s_{ij}^{\square'} \hat{f}_{i,\alpha}^\dagger \hat{f}_{j,\alpha} + \Delta_{\square'} \nu_{ij}^{\square'} (\hat{f}_{i,\uparrow}^\dagger \hat{f}_{j,\downarrow}^\dagger + \text{h.c.}) \right].
\end{aligned} \tag{G12}$$

The associated sign parameters can be read off Fig. 33. The *Ansatz* Z3000 can be obtained from P5A by setting $\chi_s = \chi_{s'}$, $\Delta_s = \Delta_{s'}$, $\chi_\square = \chi_{\square'}$, $\Delta_\square = \Delta_{\square'}$, and $\Delta_d = \Delta_{d'} = 0$.

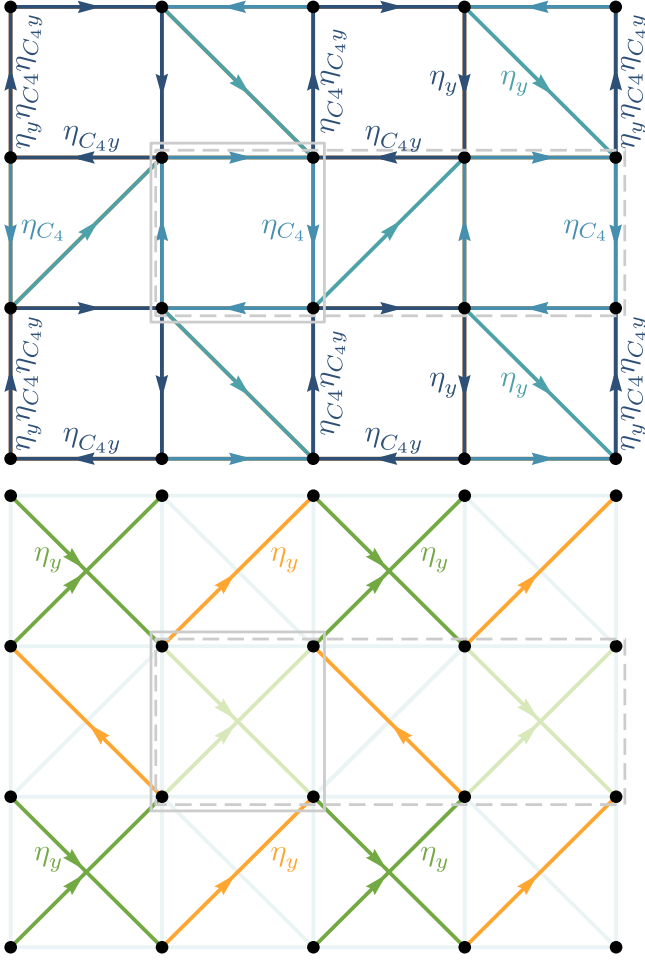


FIG. 32. Representation of \mathbb{Z}_2 *Ansätze* compatible with the symmetry group of the plaquette VBC. The link fields on the light blue (square), dark blue (square), teal (diagonal), orange (diagonal), light green (diagonal), and dark green (diagonal) bonds are given by $u_s = i\chi_s^0\tau^0 + \Delta_s^1\tau^x + \Delta_s^2\tau^y + \chi_s^3\tau^z$, $u'_s = i\chi'_s\tau^0 + \Delta'_s\tau^x + \Delta'_s\tau^y + \chi'_s\tau^z$, $u_d = i\chi_d^0\tau^0 + \Delta_d^1\tau^x + \Delta_d^2\tau^y + \chi_d^3\tau^z$, $u_{d'} = i\chi_{d'}\tau^0 + \Delta_{d'}\tau^x + \Delta_{d'}\tau^y + \chi_{d'}\tau^z$, $u_\square = i\chi_\square^0\tau^0 + \Delta_\square^1\tau^x + \Delta_\square^2\tau^y + \chi_\square^3\tau^z$, and $u_{\square'} = i\chi_{\square'}\tau^0 + \Delta_{\square'}\tau^x + \Delta_{\square'}\tau^y + \chi_{\square'}\tau^z$, respectively. The allowed mean fields for the 48 different \mathbb{Z}_2 *Ansätze* can be read off from Table XV. The solid (dashed) gray box marks the unit cell required to realize *Ansätze* in class A, with $\eta_y = +1$ (class B, with $\eta_y = -1$). The onsite terms are uniform.

Appendix H: Parent U(1) states for Z3000

As mentioned in Sec. VA, the Z3000 *Ansatz* can be obtained by starting from three *distinct* U(1) states, namely, U100, U300, and U800, and breaking down the U(1) IGG to \mathbb{Z}_2 via singlet pairing terms. While we earlier focused on the viewpoint that the Z3000 state is a descendant of U100, here, for completeness, we illustrate how both U300 and U800 can equivalently be regarded as the parent state instead.

This is easier to see first for U800. Concretely, the

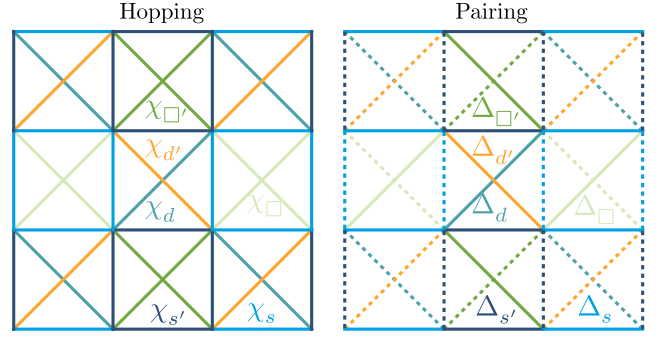


FIG. 33. Graphical illustration of the sign structure of hopping and pairing fields in the *Ansatz* P5A. In contrast to the mean-field parameters listed in Table XV, here, we choose a real gauge in order to write the *Ansatz* purely in terms of real hopping and pairing parameters, thereby making the connection to Z3000 explicit. The dashed lines denote a negative sign. The onsite hopping is uniform while the onsite pairing is negative on even numbered sites.

connection of U800 to Z3000 can be found by setting the mean-field parameters on all the diagonal bonds in Z3000 to zero, followed by an appropriate gauge transform. In the hopping-only gauge, the U800 state exhibits a Dirac cone anchored at the Γ point (see Fig. 26).

The U300 *Ansatz* has a nontrivial sign structure. Considering all the diagonals, this is given by

$$\begin{aligned} u_{12} = u_{43} = u_{21} = u_{34} = u_{14} = u_{23} = u_{41} = u_{32} &= \chi_s\tau^z, \\ u_{13} = -u_{42} = \chi_d\tau^z, \quad u_{d1} = -u_{d2} &= \chi_{d'}\tau^z, \\ u_{d3} = -u_{d4} = u_{d5} = -u_{d6} &= \chi_\square\tau^z, \\ \sum_\gamma a_\gamma(m, n, u)\tau^\gamma &= (-)^u\mu\tau^z. \end{aligned} \quad (\text{H1})$$

At first glance, the connection to Z3000 is therefore far from apparent. However, this can be established by setting $\chi_s = 0$ and $\Delta_\square = 0$ in the Z3000 *Ansatz*, followed by a gauge transformation of the form

$$W(m, n, u) = (-1)^{(\delta_{u,1} + \delta_{u,2})} (i\tau^y)^{(\delta_{u,2} + \delta_{u,4})}.$$

The dispersion of the U3000 state is sketched in Fig. 34(a), and features clear Fermi surfaces as evidenced by Fig. 34(b).

Appendix I: Chiral spin liquid descendants of Z3000

An *Ansatz* belongs to the class of chiral spin liquids (CSLs) when time-reversal symmetry \mathcal{T} is broken while spin-rotation symmetry remains intact. In contrast to the classification discussed previously—which assumes full symmetry of the lattice space group together with time reversal—a CSL respects lattice symmetries only up to a possible combination with \mathcal{T} . Consequently, the

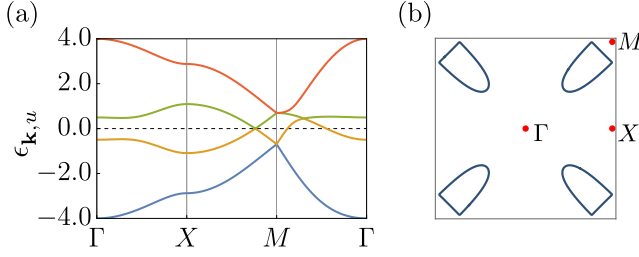


FIG. 34. (a) Dispersion of the U300 state, and (b) illustration of its Fermi surfaces. The mean-field parameters here are set to $\chi_s = 1.0$, $\chi_d = 0.5$, $\chi_{d'} = 0.4$, and $\chi_\square = 0.3$. The dashed line indicates the Fermi level.

relevant symmetry group in the present case is

$$\mathcal{O}' \in \{T_x, T_y, G_x \mathcal{T}^{\nu_{G_x}}, \sigma_{xy} \mathcal{T}^{\nu_{\sigma_{xy}}}\}, \quad (11)$$

where $\nu_{\mathcal{O}} \in \{0, 1\}$. When $\nu_{\mathcal{O}} = 0$, the lattice symmetry \mathcal{O} is preserved while \mathcal{T} is broken. In contrast, when $\nu_{\mathcal{O}} = 1$, both \mathcal{O} and \mathcal{T} are individually broken, but their product $\mathcal{O}\mathcal{T}$ remains a symmetry of the system.

The next step is to determine the projective realization of this symmetry group. Since time reversal does

not change the position of lattice sites, the projective symmetry group (PSG) of $\mathcal{O}\mathcal{T}$ coincides with that of \mathcal{O} . Therefore, the PSG elements associated with \mathcal{O}' are identical to those obtained previously for the symmetric case and are given by Eqs. (26), (27), and (28).

The corresponding *Ansätze* must then satisfy the symmetry condition

$$W_{\mathcal{O}}^\dagger(\mathcal{O}(i)) u_{\mathcal{O}(i)\mathcal{O}(j)} W_{\mathcal{O}}^\dagger(\mathcal{O}(j)) = (-1)^{\nu_{\mathcal{O}}} u_{ij}, \quad (12)$$

which ensures invariance under the combined operation $\mathcal{O}\mathcal{T}^{\nu_{\mathcal{O}}}$.

In the following, we focus on CSL states obtained by breaking time-reversal symmetry in the \mathbb{Z}_2 spin-liquid *Ansatz* labeled Z3000. The corresponding PSG is given by

$$W_{T_x}(m, n, u) = W_{T_y}(m, n, u) = \tau^0, \quad (13)$$

$$W_{G_x}(m, n, u) = \tau^0, \quad W_{\sigma_{xy}}(m, n, u) = i\tau^z. \quad (14)$$

With this PSG, four distinct CSL realizations are possible, corresponding to the four choices of $(\nu_{G_x}, \nu_{\sigma_{xy}})$: (0, 0), (0, 1), (1, 0), and (1, 1). We label these states using the notation $Z3000_{\nu_{G_x}, \nu_{\sigma_{xy}}}$. The explicit forms of the four CSL *Ansätze* are presented below.

$$u_{12} = u_{43}^\dagger = \eta_{\nu_{G_x}} u_{21} = \eta_{\nu_{G_x}} u_{34}^\dagger = u_s = i\chi_s^0 \tau^0 + \Delta_s^1 \tau^x + \Delta_s^2 \tau^y + \chi_s^3 \tau^z, \quad (15)$$

$$\eta_{\nu_{\sigma_{xy}}} u_{14} = \eta_{\nu_{\sigma_{xy}}} u_{23}^\dagger = \eta_{\nu_{G_x}} \eta_{\nu_{\sigma_{xy}}} u_{41} = \eta_{\nu_{G_x}} \eta_{\nu_{\sigma_{xy}}} u_{32}^\dagger = \tau^z u_s \tau^z, \quad (16)$$

$$u_{13} = \eta_{\nu_{G_x}} u_{42} = u_d = (\Delta_d^1 \tau^x + \Delta_d^2 \tau^y) \delta_{\nu_{\sigma_{xy}}, 1} + \chi_d^3 \tau^z \delta_{\nu_{\sigma_{xy}}, 0}, \quad (17)$$

$$u_{d_1} = \eta_{\nu_{G_x}} u_{d_2} = u_{d'} = (\Delta_{d'}^1 \tau^x + \Delta_{d'}^2 \tau^y) \delta_{\nu_{\sigma_{xy}}, 1} + \chi_{d'}^3 \tau^z \delta_{\nu_{\sigma_{xy}}, 0}, \quad (18)$$

$$u_{d_3} = \eta_{\nu_{G_x}} \eta_{\nu_{\sigma_{xy}}} (\tau^z)^p u_{d_4} (\tau^z)^p = \eta_{\nu_{\sigma_{xy}}} (\tau^z)^p u_{d_5} (\tau^z)^p = \eta_{\nu_{G_x}} u_{d_6} = u_\square \equiv \Delta_\square^1 \tau^x + \Delta_\square^2 \tau^y + \chi_\square^3 \tau^z, \quad (19)$$

$$a_\gamma(m, n, u + 1) \tau^\gamma = \eta_{\nu_{G_x}}^{u+1} \left((\Delta^1 \tau^x + \Delta^2 \tau^y) \delta_{\nu_{\sigma_{xy}}, 1} + \mu \tau^z \delta_{\nu_{\sigma_{xy}}, 0} \right). \quad (110)$$

Among these four possibilities, the connection between the Z3000 state and the *Ansatz* corresponding to $(\nu_{G_x}, \nu_{\sigma_{xy}}) = (0, 0)$, denoted Z3000₀₀, is explicit. The

correspondence for the remaining three cases can be revealed through appropriate gauge transformations. The resulting gauge representations are given as follows:

$$\hat{\mathcal{H}}_{\text{MF}}^{\text{Z3000}_{00}} = \hat{\mathcal{H}}_{\text{MF}}^{\text{Z3000}} + i\chi_s^0 \sum_{\langle ij \rangle_{\text{blue}, \alpha}} s_{ij,0}^s \hat{f}_{i,\alpha}^\dagger \hat{f}_{j,\alpha} + \sum_{\langle ij \rangle_{\text{green}}} i\Delta_{\square,2} \nu_{ij,\square} (\hat{f}_{i,\uparrow}^\dagger \hat{f}_{j,\downarrow} + \text{h.c.}), \quad (111)$$

$$\begin{aligned} \hat{\mathcal{H}}_{\text{MF}}^{\text{Z3000}_{01}} = & \hat{\mathcal{H}}_{\text{MF}}^{\text{Z3000}} + \sum_{\langle ij \rangle_{\text{blue}}} \left[i\chi_s^0 \sum_{\alpha} s_{ij,0}^s \hat{f}_{i,\alpha}^\dagger \hat{f}_{j,\alpha} + i\Delta_s^2 \nu_{ij,2}^s (\hat{f}_{i,\uparrow}^\dagger \hat{f}_{j,\downarrow} + \text{h.c.}) \right] + \sum_{\langle ij \rangle_{\text{teal}}} i\Delta_d^2 \nu_{ij,2}^d (\hat{f}_{i,\uparrow}^\dagger \hat{f}_{j,\downarrow} + \text{h.c.}) \\ & + \sum_{\langle ij \rangle_{\text{orange}}} i\Delta_{d'}^2 \nu_{ij,2}^{d'} (\hat{f}_{i,\uparrow}^\dagger \hat{f}_{j,\downarrow} + \text{h.c.}) + \sum_{\langle ij \rangle_{\text{green}}} i\Delta_\square^2 \nu_{ij,\square} (\hat{f}_{i,\uparrow}^\dagger \hat{f}_{j,\downarrow} + \text{h.c.}), \end{aligned} \quad (112)$$

$$\begin{aligned}
\hat{\mathcal{H}}_{\text{MF}}^{\text{Z3000}_{10}} &= \hat{\mathcal{H}}_{\text{MF}}^{\text{Z3000}} + \sum_{\langle ij \rangle_{\text{blue}}} \left[i\chi_s^0 \sum_{\alpha} s_{ij,0}^s \hat{f}_{i,\alpha}^{\dagger} \hat{f}_{j,\alpha} + i\Delta_s^2 \nu_{ij,2}^s (\hat{f}_{i,\uparrow}^{\dagger} \hat{f}_{j,\downarrow}^{\dagger} + \text{h.c.}) \right] + \sum_{\langle ij \rangle_{\text{green}}} i\Delta_{\square}^2 \nu_{ij,2}^{\square} (\hat{f}_{i,\uparrow}^{\dagger} \hat{f}_{j,\downarrow}^{\dagger} + \text{h.c.}), \quad (\text{I13}) \\
\hat{\mathcal{H}}_{\text{MF}}^{\text{Z3000}_{11}} &= \hat{\mathcal{H}}_{\text{MF}}^{\text{Z3000}} + \sum_{\langle ij \rangle_{\text{blue}}} \left[i\chi_s^0 \sum_{\alpha} s_{ij,0}^s \hat{f}_{i,\alpha}^{\dagger} \hat{f}_{j,\alpha} + i\Delta_s^2 \nu_{ij,2}^s (\hat{f}_{i,\uparrow}^{\dagger} \hat{f}_{j,\downarrow}^{\dagger} + \text{h.c.}) \right] + \sum_{\langle ij \rangle_{\text{teal}}} \Delta_d^1 \nu_{ij,1}^d (\hat{f}_{i,\uparrow}^{\dagger} \hat{f}_{j,\downarrow}^{\dagger} + \text{h.c.}) \\
&+ \sum_{\langle ij \rangle_{\text{orange}}} \Delta_d^1 \nu_{ij,1}^{d'} (\hat{f}_{i,\uparrow}^{\dagger} \hat{f}_{j,\downarrow}^{\dagger} + \text{h.c.}) + \sum_{\langle ij \rangle_{\text{green}}} \Delta_{\square}^2 \nu_{ij,2}^{\square} (\hat{f}_{i,\uparrow}^{\dagger} \hat{f}_{j,\downarrow}^{\dagger} + \text{h.c.}) + \Delta^1 \sum_i \nu_{i,1} (\hat{f}_{i,\uparrow}^{\dagger} \hat{f}_{i,\downarrow}^{\dagger} + \text{h.c.}). \quad (\text{I14})
\end{aligned}$$

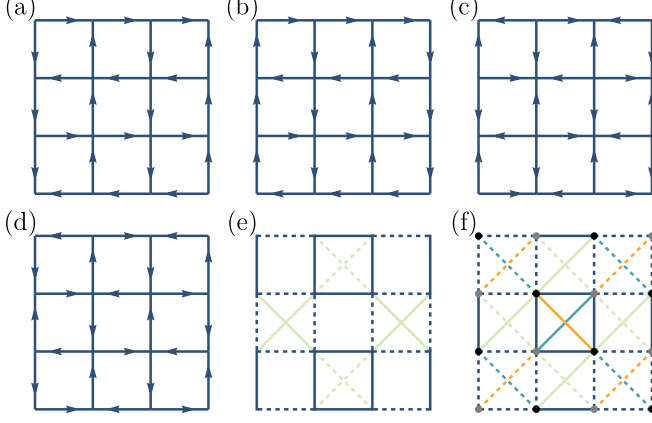


FIG. 35. Graphical illustration of the sign structures (s_{ij} and ν_{ij}) for the CSL states obtained by lowering the symmetry of the Z3000 *Ansatz*. Panels (a)–(d) show the configurations of $s_{ij,0}^s$ for the *Ansätze* labeled Z3000₀₀, Z3000₀₁, Z3000₁₀, and Z3000₁₁, respectively. Along the array direction $s_{ij,0}^s = +1$, while $s_{ij,0}^s = -1$ elsewhere. Panel (e) illustrates the configurations of $\nu_{ij,2}^s$ and $\nu_{ij,2}^{\square}$ for Z3000₁₀, shown in blue and green, respectively; solid (dashed) bonds denote positive (negative) signs. Panel (f) shows the configurations of $\nu_{ij,2}^s$, $\nu_{ij,1}^d$, $\nu_{ij,1}^{d'}$, and $\nu_{ij,2}^{\square}$ for Z3000₁₁, represented in blue, teal, orange, and green, respectively. In addition, this state exhibits a staggered onsite pairing, where the positive ($\nu_{i,1} = +1$) and negative ($\nu_{i,1} = -1$) signs are indicated by gray and black sites.

Here, the parameters s and ν specify the sign configurations of the corresponding amplitudes. For Z3000₀₀, the pairing term $\nu_{ij,2}^{\square}$ follows the same sign pattern as ν_{ij}^{\square} in Eq. (49) (see also Fig. 10(c)). In the case of Z3000₀₁, all additional pairing terms are uniform, namely $\nu_{ij,2}^s = \nu_{ij,2}^d = \nu_{ij,2}^{d'} = \nu_{ij,2}^{\square} = +1$. The remaining sign configurations for the other chiral *Ansätze* are illustrated in Fig. 35.

The CSL *Ansatz* labeled Z3000₀₀ exhibits gapless excitations with Dirac points located along either the \overline{MT} or \overline{MX} directions, depending on the values of the parameters χ_s^0 and Δ_{\square}^2 . In contrast, the Z3000₀₁ *Ansatz* generally develops a gapped dispersion when the pairing amplitudes Δ_d^2 and $\Delta_{d'}^2$ become sufficiently large. The remaining two CSL *Ansätze*, Z3000₁₀ and Z3000₁₁, typically exhibit fully gapped excitation spectra. The corre-

Label	G_x	σ_{xy}	\mathcal{T}	$\mathcal{T}G_x$	$\mathcal{T}\sigma_{xy}$
Z3000 ₀₀	✓	✓	✗	✗	✗
Z3000 ₀₁	✓	✗	✗	✗	✓
Z3000 ₁₀	✗	✓	✗	✓	✗
Z3000 ₁₁	✗	✗	✗	✓	✓

TABLE XVI. Symmetry properties of the four CSLs which are symmetry-lowered descendants of Z3000.

sponding dispersions for these four CSL states are shown in Fig. 36.

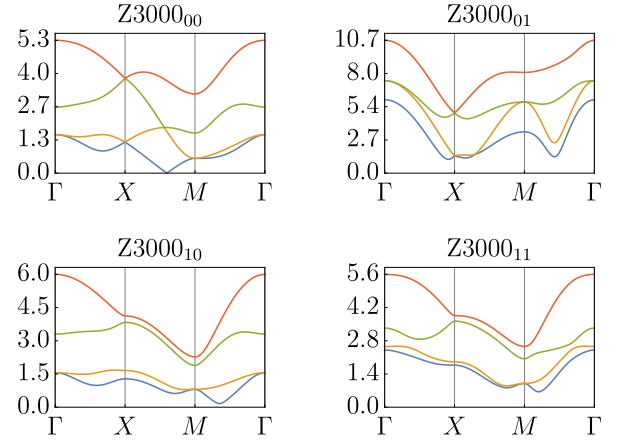


FIG. 36. Mean-field dispersion of the four chiral spin-liquid states derived from the Z3000 *Ansatz*.

- [1] B. Sriram Shastry and B. Sutherland, Exact ground state of a quantum mechanical antiferromagnet, *Physica B+C* **108**, 1069 (1981).
- [2] H. Kageyama, K. Yoshimura, R. Stern, N. V. Mushnikov, K. Onizuka, M. Kato, K. Kosuge, C. P. Slichter, T. Goto, and Y. Ueda, Exact Dimer Ground State and Quantized Magnetization Plateaus in the Two-Dimensional Spin System $\text{SrCu}_2(\text{BO}_3)_2$, *Phys. Rev. Lett.* **82**, 3168 (1999).
- [3] S. Miyahara and K. Ueda, Theory of the orthogonal dimer Heisenberg spin model for $\text{SrCu}_2(\text{BO}_3)_2$, *J. Phys.: Condens. Matter* **15**, R327 (2003).
- [4] P. C. G. Vlaar and P. Corboz, Tensor network study of the Shastry-Sutherland model with weak interlayer coupling, *SciPost Phys.* **15**, 126 (2023).
- [5] F. Ferrari and R. Valentí, Altermagnetism on the Shastry-Sutherland lattice, *Phys. Rev. B* **110**, 205140 (2024).
- [6] Q. Ma, B. R. Billingsley, M. Marshall, D. A. Dahlbom, Y. Hao, D. M. Pajerowski, A. I. Kolesnikov, X. Bai, C. D. Batista, T. Kong, and H. Cao, Quantum entanglement of XY-type spin dimers in Shastry-Sutherland lattice (2024), [arXiv:2412.17913 \[cond-mat.str-el\]](https://arxiv.org/abs/2412.17913).
- [7] N. Li, A. Brassington, M. F. Shu, Y. Y. Wang, H. Liang, Q. J. Li, X. Zhao, P. J. Baker, H. Kikuchi, T. Masuda, G. Duan, C. Liu, H. Wang, W. Xie, R. Zhong, J. Ma, R. Yu, H. D. Zhou, and X. F. Sun, Spinons in a new Shastry-Sutherland lattice magnet $\text{Pr}_2\text{Ga}_2\text{BeO}_7$ (2024), [arXiv:2405.13628 \[cond-mat.str-el\]](https://arxiv.org/abs/2405.13628).
- [8] A. Liu, F. Song, Y. Cao, H. Ge, H. Bu, J. Zhou, Y. Qin, Q. Zeng, J. Li, L. Ling, W. Tong, J. Sheng, M. Yang, L. Wu, H. Guo, and Z. Tian, Distinct magnetic ground states in Shastry-Sutherland lattice materials: $\text{Pr}_2\text{Be}_2\text{GeO}_7$ versus $\text{Nd}_2\text{Be}_2\text{GeO}_7$, *Phys. Rev. B* **109**, 184413 (2024).
- [9] M. Pula, S. Sharma, J. Gautreau, S. K. P., A. Kanigel, M. D. Frontzek, T. N. Dolling, L. Clark, S. Dunsiger, A. Ghara, and G. M. Luke, Candidate for a quantum spin liquid ground state in the Shastry-Sutherland lattice material $\text{Yb}_2\text{Be}_2\text{GeO}_7$, *Phys. Rev. B* **110**, 014412 (2024).
- [10] A. Brassington, Q. Ma, G. Sala, A. I. Kolesnikov, K. M. Taddei, Y. Wu, E. S. Choi, H. Wang, W. Xie, J. Ma, H. D. Zhou, and A. A. Aczel, Magnetic properties of the quasi-XY Shastry-Sutherland magnet $\text{Er}_2\text{Be}_2\text{SiO}_7$, *Phys. Rev. Mater.* **8**, 094001 (2024).
- [11] L. Yadav, A. Rufino, R. Bag, M. Ennis, J. A. Koziol, C. d. Cruz, A. I. Kolesnikov, V. O. Garlea, K. M. Taddei, D. Graf, K. P. Schmidt, F. Mila, and S. Haravifard, Observation of unprecedented fractional magnetization plateaus in a new shastry-sutherland ising compound, *Phys. Rev. X* **15**, 041045 (2025).
- [12] M. Pula, S. Sharma, J. Gautreau, S. KP, A. Kanigel, C. dela Cruz, T. Dolling, L. Clark, and G. Luke, Fractional magnetization plateaus in the Shastry-Sutherland lattice material $\text{Er}_2\text{Be}_2\text{GeO}_7$, *Journal of Physics: Condensed Matter* **37**, 425802 (2025).
- [13] S. Miyahara and K. Ueda, Exact Dimer Ground State of the Two Dimensional Heisenberg Spin System $\text{SrCu}_2(\text{BO}_3)_2$, *Phys. Rev. Lett.* **82**, 3701 (1999).
- [14] Z. Weihong, C. J. Hamer, and J. Oitmaa, Series expansions for a Heisenberg antiferromagnetic model for $\text{SrCu}_2(\text{BO}_3)_2$, *Phys. Rev. B* **60**, 6608 (1999).
- [15] E. Müller-Hartmann, R. R. P. Singh, C. Knetter, and G. S. Uhrig, Exact Demonstration of Magnetization Plateaus and First-Order Dimer-Néel Phase Transitions in a Modified Shastry-Sutherland Model for $\text{SrCu}_2(\text{BO}_3)_2$, *Phys. Rev. Lett.* **84**, 1808 (2000).
- [16] M. Albrecht and F. Mila, First-order transition between magnetic order and valence bond order in a 2D frustrated Heisenberg model, *Europhys. Lett.* **34**, 145 (1996).
- [17] T. Munehisa and Y. Munehisa, Numerical Study of Excited States in the Shastry-Sutherland Model, *J. Phys. Soc. Jpn.* **72**, 160 (2003).
- [18] T. Munehisa and Y. Munehisa, The Stochastic State Selection Method for Energy Eigenvalues in the Shastry-Sutherland Model, *J. Phys. Soc. Jpn.* **73**, 340 (2004).
- [19] R. Darradi, J. Richter, and D. J. J. Farnell, Coupled cluster treatment of the Shastry-Sutherland antiferromagnet, *Phys. Rev. B* **72**, 104425 (2005).
- [20] C. Knetter, A. Bühler, E. Müller-Hartmann, and G. S. Uhrig, Dispersion and Symmetry of Bound States in the Shastry-Sutherland Model, *Phys. Rev. Lett.* **85**, 3958 (2000).
- [21] M. Al Hajj and J.-P. Malrieu, Phase transitions in the Shastry-Sutherland lattice, *Phys. Rev. B* **72**, 094436 (2005).
- [22] A. Koga and N. Kawakami, Quantum Phase Transitions in the Shastry-Sutherland Model for $\text{SrCu}_2(\text{BO}_3)_2$, *Phys. Rev. Lett.* **84**, 4461 (2000).
- [23] Y. Takushima, A. Koga, and N. Kawakami, Competing Spin-Gap Phases in a Frustrated Quantum Spin System in Two Dimensions, *J. Phys. Soc. Jpn.* **70**, 1369 (2001).
- [24] W. Zheng, J. Oitmaa, and C. J. Hamer, Phase diagram of the Shastry-Sutherland antiferromagnet, *Phys. Rev. B* **65**, 014408 (2001).
- [25] C. H. Chung, J. B. Marston, and S. Sachdev, Quantum phases of the Shastry-Sutherland antiferromagnet: Application to $\text{SrCu}_2(\text{BO}_3)_2$, *Phys. Rev. B* **64**, 134407 (2001).
- [26] A. Läuchli, S. Wessel, and M. Sgrist, Phase diagram of the quadrumerized Shastry-Sutherland model, *Phys. Rev. B* **66**, 014401 (2002).
- [27] R. Kumar and B. Kumar, Triplon mean-field analysis of an antiferromagnet with degenerate Shastry-Sutherland ground states, *J. Phys. Commun.* **1**, 055020 (2017).
- [28] S. Moukouri, Plaquette ground state of the Shastry-Sutherland model: Density-matrix renormalization-group calculations, *Phys. Rev. B* **78**, 132405 (2008).
- [29] A. Isacsson and O. F. Syljuåsen, Variational treatment of the Shastry-Sutherland antiferromagnet using projected entangled pair states, *Phys. Rev. E* **74**, 026701 (2006).
- [30] P. Corboz and F. Mila, Tensor network study of the Shastry-Sutherland model in zero magnetic field, *Phys. Rev. B* **87**, 115144 (2013).

- [31] J. Y. Lee, Y.-Z. You, S. Sachdev, and A. Vishwanath, Signatures of a Deconfined Phase Transition on the Shastry-Sutherland Lattice: Applications to Quantum Critical $\text{SrCu}_2(\text{BO}_3)_2$, *Phys. Rev. X* **9**, 041037 (2019).
- [32] A. Keleş and E. Zhao, Rise and fall of plaquette order in the Shastry-Sutherland magnet revealed by pseudofermion functional renormalization group, *Phys. Rev. B* **105**, L041115 (2022).
- [33] T. Waki, K. Arai, M. Takigawa, Y. Saiga, Y. Uwatoko, H. Kageyama, and Y. Ueda, A Novel Ordered Phase in $\text{SrCu}_2(\text{BO}_3)_2$ under High Pressure, *J. Phys. Soc. Jpn.* **76**, 073710 (2007).
- [34] M. E. Zayed, C. Rüegg, J. Larrea J., A. M. Läuchli, C. Panagopoulos, S. S. Saxena, M. Ellerby, D. F. McMorrow, T. Strässle, S. Klotz, G. Hamel, R. A. Sadykov, V. Pomjakushin, M. Boehm, M. Jiménez-Ruiz, A. Schneidewind, E. Pomjakushina, M. Stingaciu, K. Conder, and H. M. Rønnow, 4-spin plaquette singlet state in the Shastry-Sutherland compound $\text{SrCu}_2(\text{BO}_3)_2$, *Nat. Phys.* **13**, 962 (2017).
- [35] J. Guo, G. Sun, B. Zhao, L. Wang, W. Hong, V. A. Sidorov, N. Ma, Q. Wu, S. Li, Z. Y. Meng, A. W. Sandvik, and L. Sun, Quantum Phases of $\text{SrCu}_2(\text{BO}_3)_2$ from High-Pressure Thermodynamics, *Phys. Rev. Lett.* **124**, 206602 (2020).
- [36] W.-Y. Liu, X.-T. Zhang, Z. Wang, S.-S. Gong, W.-Q. Chen, and Z.-C. Gu, Quantum Criticality with Emergent Symmetry in the Extended Shastry-Sutherland Model, *Phys. Rev. Lett.* **133**, 026502 (2024).
- [37] X. Qian, R. Lv, J. Y. Lee, and M. Qin, From the shastry-sutherland model to the $J_1 - J_2$ heisenberg model, *Phys. Rev. B* **111**, L241113 (2025).
- [38] H. Chen, G. Duan, C. Liu, Y. Cui, W. Yu, Z. Y. Xie, and R. Yu, Spin excitations of the Shastry-Sutherland model – altermagnetism and proximate deconfined quantum criticality (2024), [arXiv:2411.00301 \[cond-mat.str-el\]](https://arxiv.org/abs/2411.00301).
- [39] Y.-T. Yang, F.-Z. Chen, and H.-G. Luo, Identifying the ground state phases by spin-patterns in the Shastry-Sutherland model (2024), [arXiv:2404.16330 \[cond-mat.str-el\]](https://arxiv.org/abs/2404.16330).
- [40] N. Xi, H. Chen, Z. Y. Xie, and R. Yu, Plaquette valence bond solid to antiferromagnet transition and deconfined quantum critical point of the Shastry-Sutherland model, *Phys. Rev. B* **107**, L220408 (2023).
- [41] A. Feuerpfel, L. Shackleton, A. Maity, R. Thomale, S. Sachdev, and Y. Iqbal, Unifying Dirac Spin Liquids on Square and Shastry-Sutherland Lattices via Fermionic Deconfined Criticality, (2026), [arXiv:2601.19980 \[cond-mat.str-el\]](https://arxiv.org/abs/2601.19980).
- [42] J. Yang, A. W. Sandvik, and L. Wang, Quantum criticality and spin liquid phase in the Shastry-Sutherland model, *Phys. Rev. B* **105**, L060409 (2022).
- [43] L. Wang, Y. Zhang, and A. W. Sandvik, Quantum Spin Liquid Phase in the Shastry-Sutherland Model Detected by an Improved Level Spectroscopic Method, *Chin. Phys. Lett.* **39**, 077502 (2022).
- [44] H. Nakano and T. Sakai, Third Boundary of the Shastry-Sutherland Model by Numerical Diagonalization, *J. Phys. Soc. Jpn.* **87**, 123702 (2018).
- [45] D. C. Ronquillo and M. R. Peterson, Identifying topological order in the Shastry-Sutherland model via entanglement entropy, *Phys. Rev. B* **90**, 201108 (2014).
- [46] L. L. Viteritti, R. Rende, A. Parola, S. Goldt, and F. Becca, Transformer wave function for two dimensional frustrated magnets: Emergence of a spin-liquid phase in the Shastry-Sutherland model, *Phys. Rev. B* **111**, 134411 (2025).
- [47] M. Mezera, J. Menšíková, P. Baláz, and M. Žonda, Neural network quantum states analysis of the Shastry-Sutherland model, *SciPost Phys. Core* **6**, 088 (2023).
- [48] W.-J. Hu, F. Becca, A. Parola, and S. Sorella, Direct evidence for a gapless Z_2 spin liquid by frustrating Néel antiferromagnetism, *Phys. Rev. B* **88**, 060402 (2013).
- [49] F. Ferrari and F. Becca, Gapless spin liquid and valence-bond solid in the $J_1 - J_2$ Heisenberg model on the square lattice: Insights from singlet and triplet excitations, *Phys. Rev. B* **102**, 014417 (2020).
- [50] S. Morita, R. Kaneko, and M. Imada, Quantum Spin Liquid in Spin-1/2 $J_1 - J_2$ Heisenberg Model on Square Lattice: Many-Variable Variational Monte Carlo Study Combined with Quantum-Number Projections, *J. Phys. Soc. Jpn.* **84**, 024720 (2015).
- [51] Y. Nomura and M. Imada, Dirac-Type Nodal Spin Liquid Revealed by Refined Quantum Many-Body Solver Using Neural-Network Wave Function, Correlation Ratio, and Level Spectroscopy, *Phys. Rev. X* **11**, 031034 (2021).
- [52] L. Wang and A. W. Sandvik, Critical Level Crossings and Gapless Spin Liquid in the Square-Lattice Spin-1/2 $J_1 - J_2$ Heisenberg Antiferromagnet, *Phys. Rev. Lett.* **121**, 107202 (2018).
- [53] W.-Y. Liu, S. Dong, C. Wang, Y. Han, H. An, G.-C. Guo, and L. He, Gapless spin liquid ground state of the spin- $\frac{1}{2}$ $J_1 - J_2$ Heisenberg model on square lattices, *Phys. Rev. B* **98**, 241109 (2018).
- [54] W.-Y. Liu, S.-S. Gong, Y.-B. Li, D. Poilblanc, W.-Q. Chen, and Z.-C. Gu, Gapless quantum spin liquid and global phase diagram of the spin-1/2 $J_1 - J_2$ square antiferromagnetic Heisenberg model, *Sci. Bull.* **67**, 1034 (2022).
- [55] A. Ralko, M. Mambrini, and D. Poilblanc, Generalized quantum dimer model applied to the frustrated Heisenberg model on the square lattice: Emergence of a mixed columnar-plaquette phase, *Phys. Rev. B* **80**, 184427 (2009).
- [56] X.-G. Wen, Quantum orders and symmetric spin liquids, *Phys. Rev. B* **65**, 165113 (2002).
- [57] X.-G. Wen, *Quantum Field Theory of Many-Body Systems: From the Origin of Sound to an Origin of Light and Electrons* (Oxford University Press, 2007).
- [58] F. Wang and A. Vishwanath, Spin-liquid states on the triangular and Kagomé lattices: A projective-symmetry-group analysis of Schwinger boson states, *Phys. Rev. B* **74**, 174423 (2006).
- [59] M. J. Lawler, A. Paramekanti, Y. B. Kim, and L. Balents, Gapless Spin Liquids on the Three-Dimensional Hyperkagome Lattice of $\text{Na}_4\text{Ir}_3\text{O}_8$, *Phys. Rev. Lett.* **101**, 197202 (2008).
- [60] T.-P. Choy and Y. B. Kim, Classification of quantum phases for the star-lattice antiferromagnet via a projective symmetry group analysis, *Phys. Rev. B* **80**, 064404 (2009).
- [61] B.-J. Yang, A. Paramekanti, and Y. B. Kim, Competing quantum paramagnetic ground states of the Heisenberg

- antiferromagnet on the star lattice, *Phys. Rev. B* **81**, 134418 (2010).
- [62] Y.-M. Lu, Y. Ran, and P. A. Lee, \mathbb{Z}_2 spin liquids in the $S = \frac{1}{2}$ Heisenberg model on the kagome lattice: A projective symmetry-group study of Schwinger fermion mean-field states, *Phys. Rev. B* **83**, 224413 (2011).
- [63] Y.-M. Lu and Y. Ran, \mathbb{Z}_2 spin liquid and chiral antiferromagnetic phase in the Hubbard model on a honeycomb lattice, *Phys. Rev. B* **84**, 024420 (2011).
- [64] F. Yang and H. Yao, Frustrated resonating valence bond states in two dimensions: Classification and short-range correlations, *Phys. Rev. Lett.* **109**, 147209 (2012).
- [65] L. Messio, C. Lhuillier, and G. Misguich, Time reversal symmetry breaking chiral spin liquids: Projective symmetry group approach of bosonic mean-field theories, *Phys. Rev. B* **87**, 125127 (2013).
- [66] S. Bieri, L. Messio, B. Bernu, and C. Lhuillier, Gapless chiral spin liquid in a kagome Heisenberg model, *Phys. Rev. B* **92**, 060407 (2015).
- [67] X. Yang and F. Wang, Schwinger boson spin-liquid states on square lattice, *Phys. Rev. B* **94**, 035160 (2016).
- [68] Y.-M. Lu, Symmetric \mathbb{Z}_2 spin liquids and their neighboring phases on triangular lattice, *Phys. Rev. B* **93**, 165113 (2016).
- [69] S. Bieri, C. Lhuillier, and L. Messio, Projective symmetry group classification of chiral spin liquids, *Phys. Rev. B* **93**, 094437 (2016).
- [70] B. Huang, Y. B. Kim, and Y.-M. Lu, Interplay of nonsymmorphic symmetry and spin-orbit coupling in hyperkagome spin liquids: Applications to $\text{Na}_4\text{Ir}_3\text{O}_8$, *Phys. Rev. B* **95**, 054404 (2017).
- [71] B. Huang, W. Choi, Y. B. Kim, and Y.-M. Lu, Classification and properties of quantum spin liquids on the hyperhoneycomb lattice, *Phys. Rev. B* **97**, 195141 (2018).
- [72] Y.-M. Lu, Symmetry-protected gapless \mathbb{Z}_2 spin liquids, *Phys. Rev. B* **97**, 094422 (2018).
- [73] C. Liu, G. B. Halász, and L. Balents, Competing orders in pyrochlore magnets from a \mathbb{Z}_2 spin liquid perspective, *Phys. Rev. B* **100**, 075125 (2019).
- [74] H.-K. Jin and Y. Zhou, Classical and quantum order in hyperkagome antiferromagnets, *Phys. Rev. B* **101**, 054408 (2020).
- [75] J. Sonnenschein, A. Chauhan, Y. Iqbal, and J. Reuther, Projective symmetry group classifications of quantum spin liquids on the simple cubic, body centered cubic, and face centered cubic lattices, *Phys. Rev. B* **102**, 125140 (2020).
- [76] J. Sahoo and R. Flint, Symmetric spin liquids on the stuffed honeycomb lattice, *Phys. Rev. B* **101**, 115103 (2020).
- [77] C. Liu, G. B. Halász, and L. Balents, Symmetric $U(1)$ and \mathbb{Z}_2 spin liquids on the pyrochlore lattice, *Phys. Rev. B* **104**, 054401 (2021).
- [78] L. E. Chern and Y. B. Kim, Theoretical study of quantum spin liquids in $S = \frac{1}{2}$ hyper-hyperkagome magnets: Classification, heat capacity, and dynamical spin structure factor, *Phys. Rev. B* **104**, 094413 (2021).
- [79] L. E. Chern, Y. B. Kim, and C. Castelnovo, Competing quantum spin liquids, gauge fluctuations, and anisotropic interactions in a breathing pyrochlore lattice, *Phys. Rev. B* **106**, 134402 (2022).
- [80] B. Schneider, J. C. Halimeh, and M. Punk, Projective symmetry group classification of chiral \mathbb{Z}_2 spin liquids on the pyrochlore lattice: Application to the spin- $\frac{1}{2}$ XXZ Heisenberg model, *Phys. Rev. B* **105**, 125122 (2022).
- [81] A. Maity, F. Ferrari, R. Thomale, S. Mandal, and Y. Iqbal, Projective symmetry group classification of Abrikosov fermion mean-field ansätze on the square-octagon lattice, *Phys. Rev. B* **107**, 134438 (2023).
- [82] A. Chauhan, A. Maity, C. Liu, J. Sonnenschein, F. Ferrari, and Y. Iqbal, Quantum spin liquids on the diamond lattice, *Phys. Rev. B* **108**, 134424 (2023).
- [83] K. Liu and F. Wang, Schwinger boson symmetric spin liquids of Shastry-Sutherland model, *Phys. Rev. B* **109**, 134409 (2024).
- [84] J. Sonnenschein, A. Maity, C. Liu, R. Thomale, F. Ferrari, and Y. Iqbal, Candidate quantum spin liquids on the maple-leaf lattice, *Phys. Rev. B* **110**, 014414 (2024).
- [85] A. Maity, R. Samajdar, and Y. Iqbal, Gapped and gapless quantum spin liquids on the ruby lattice (2024), [arXiv:2409.16344 \[cond-mat.str-el\]](https://arxiv.org/abs/2409.16344).
- [86] A. Maity, Y. Iqbal, and R. Samajdar, Fermionic parton theory of Rydberg \mathbb{Z}_2 quantum spin liquids (2024), [arXiv:2409.17219 \[cond-mat.str-el\]](https://arxiv.org/abs/2409.17219).
- [87] A. A. Abrikosov, Electron scattering on magnetic impurities in metals and anomalous resistivity effects, *Physics* **2**, 5 (1965).
- [88] G. Baskaran and P. W. Anderson, Gauge theory of high-temperature superconductors and strongly correlated Fermi systems, *Phys. Rev. B* **37**, 580 (1988).
- [89] I. Affleck, Z. Zou, T. Hsu, and P. W. Anderson, $SU(2)$ gauge symmetry of the large- U limit of the Hubbard model, *Phys. Rev. B* **38**, 745 (1988).
- [90] Z.-X. Liu, Y. Zhou, and T.-K. Ng, Fermionic theory for quantum antiferromagnets with spin $S > \frac{1}{2}$, *Phys. Rev. B* **82**, 144422 (2010).
- [91] R. Shindou, S. Yunoki, and T. Momoi, Projective studies of spin nematics in a quantum frustrated ferromagnet, *Phys. Rev. B* **84**, 134414 (2011).
- [92] J. Reuther, S.-P. Lee, and J. Alicea, Classification of spin liquids on the square lattice with strong spin-orbit coupling, *Phys. Rev. B* **90**, 174417 (2014).
- [93] F. Becca and S. Sorella, *Quantum Monte Carlo Approaches for Correlated Systems* (Cambridge University Press, 2017).
- [94] S. Sorella, Wave function optimization in the variational Monte Carlo method, *Phys. Rev. B* **71**, 241103 (2005).
- [95] S. Yunoki and S. Sorella, Two spin liquid phases in the spatially anisotropic triangular Heisenberg model, *Phys. Rev. B* **74**, 014408 (2006).
- [96] Y. Iqbal, D. Poilblanc, and F. Becca, Spin- $\frac{1}{2}$ Heisenberg $J_1 - J_2$ antiferromagnet on the kagome lattice, *Phys. Rev. B* **91**, 020402 (2015).
- [97] Y. Iqbal, F. Ferrari, A. Chauhan, A. Parola, D. Poilblanc, and F. Becca, Gutzwiller projected states for the $J_1 - J_2$ Heisenberg model on the Kagome lattice: Achievements and pitfalls, *Phys. Rev. B* **104**, 144406 (2021).
- [98] M. Hering, V. Noculak, F. Ferrari, Y. Iqbal, and J. Reuther, Dimerization tendencies of the pyrochlore Heisenberg antiferromagnet: A functional renormalization group perspective, *Phys. Rev. B* **105**, 054426 (2022).

- [99] F. Ferrari, S. Niu, J. Hasik, Y. Iqbal, D. Poilblanc, and F. Becca, Static and dynamical signatures of Dzyaloshinskii-Moriya interactions in the Heisenberg model on the kagome lattice, *SciPost Phys.* **14**, 139 (2023).
- [100] T. Müller, R. Thomale, S. Sachdev, and Y. Iqbal, Polaronic correlations from optimized ancilla wave functions for the Fermi-Hubbard model, *Proc. Natl. Acad. Sci. U.S.A.* **122**, e2504261122 (2025).
- [101] S. Sorella, Generalized Lanczos algorithm for variational quantum Monte Carlo, *Phys. Rev. B* **64**, 024512 (2001).
- [102] F. Becca, W.-J. Hu, Y. Iqbal, A. Parola, D. Poilblanc, and S. Sorella, Lanczos steps to improve variational wave functions, *J. Phys. Conf. Ser.* **640**, 012039 (2015).
- [103] Y. Iqbal, F. Becca, and D. Poilblanc, Projected wave function study of \mathbb{Z}_2 spin liquids on the kagome lattice for the spin- $\frac{1}{2}$ quantum Heisenberg antiferromagnet, *Phys. Rev. B* **84**, 020407 (2011).
- [104] Y. Iqbal, F. Becca, S. Sorella, and D. Poilblanc, Gapless spin-liquid phase in the kagome spin- $\frac{1}{2}$ Heisenberg antiferromagnet, *Phys. Rev. B* **87**, 060405 (2013).
- [105] Y. Iqbal, W.-J. Hu, R. Thomale, D. Poilblanc, and F. Becca, Spin liquid nature in the Heisenberg $J_1 - J_2$ triangular antiferromagnet, *Phys. Rev. B* **93**, 144411 (2016).
- [106] Y. Iqbal, D. Poilblanc, and F. Becca, Vanishing spin gap in a competing spin-liquid phase in the kagome Heisenberg antiferromagnet, *Phys. Rev. B* **89**, 020407 (2014).
- [107] C. Knetter and G. S. Uhrig, Dynamic Structure Factor of the Two-Dimensional Shastry-Sutherland Model, *Phys. Rev. Lett.* **92**, 027204 (2004).
- [108] T. Müller, D. Kiese, N. Niggemann, B. Sbierski, J. Reuther, S. Trebst, R. Thomale, and Y. Iqbal, Pseudo-fermion functional renormalization group for spin models, *Rep. Prog. Phys.* **87**, 036501 (2024).
- [109] J. Reuther and R. Thomale, Cluster functional renormalization group, *Phys. Rev. B* **89**, 024412 (2014).
- [110] J. Potten, Y. Iqbal, R. Thomale, and T. Müller, Keldysh pseudofermion functional renormalization group for quantum magnetism, *Phys. Rev. B* **112**, 235132 (2025).
- [111] U. Löw and E. Müller-Hartmann, Exact Bounds on the Critical Frustration in the Shastry-Sutherland Model, *J. Low Temp. Phys.* **126**, 1135 (2002).
- [112] A. Grechnev, Exact ground state of the Shastry-Sutherland lattice with classical Heisenberg spins, *Phys. Rev. B* **87**, 144419 (2013).
- [113] A. V. Chubukov, On the quantum effects in helimagnets, *J. Phys. C* **17**, L991 (1984).
- [114] D. Kiese, F. Ferrari, N. Astrakhantsev, N. Niggemann, P. Ghosh, T. Müller, R. Thomale, T. Neupert, J. Reuther, M. J. P. Gingras, S. Trebst, and Y. Iqbal, Pinch-points to half-moons and up in the stars: The kagome skymap, *Phys. Rev. Res.* **5**, L012025 (2023).
- [115] E. Manousakis, The spin- $\frac{1}{2}$ Heisenberg antiferromagnet on a square lattice and its application to the cuprous oxides, *Rev. Mod. Phys.* **63**, 1 (1991).
- [116] P. Corboz, Y. Zhang, B. Ponsioen, and F. Mila, Quantum spin liquid phase in the Shastry-Sutherland model revealed by high-precision infinite projected entangled-pair states, (2025), [arXiv:2502.14091](https://arxiv.org/abs/2502.14091) [cond-mat.str-el].
- [117] A. Thomson and S. Sachdev, Fermionic Spinon Theory of Square Lattice Spin Liquids near the Néel State, *Phys. Rev. X* **8**, 011012 (2018).
- [118] H. Shackleton, A. Thomson, and S. Sachdev, Deconfined criticality and a gapless \mathbb{Z}_2 spin liquid in the square-lattice antiferromagnet, *Phys. Rev. B* **104**, 045110 (2021).
- [119] J.-W. Yang, W.-W. Luo, W. Zhu, L. Wang, B. Yang, and P. Sengupta, Chiral spin liquid on a Shastry-Sutherland Heisenberg antiferromagnet, *Phys. Rev. B* **109**, 205111 (2024).
- [120] F. Dusel, T. Hofmann, A. Maity, R. Mosseri, J. Vidal, Y. Iqbal, M. Greiter, and R. Thomale, Chiral Gapless Spin Liquid in Hyperbolic Space, *Phys. Rev. Lett.* **134**, 256604 (2025).
- [121] F. Oliviero, J. A. Sobral, E. C. Andrade, and R. G. Pereira, Noncoplanar magnetic orders and gapless chiral spin liquid on the kagome lattice with staggered scalar spin chirality, *SciPost Phys.* **13**, 050 (2022).
- [122] H. S. Kim, H.-J. Yang, K. Penc, and S. Lee, Spin liquid landscapes in the kagome lattice: A variational Monte Carlo study of the chiral Heisenberg model and experimental signatures, *Phys. Rev. B* **113**, 064432 (2026).
- [123] G. Duan, R. Yu, and C. Liu, Theory of magnetism for rare-earth magnets on the Shastry-Sutherland lattice with non-Kramers ions, *Phys. Rev. B* **110**, 214410 (2024).
- [124] C. Liu, G. Duan, and R. Yu, Theory of rare-earth Kramers magnets on a Shastry-Sutherland lattice: dimer phases in the presence of strong spin-orbit coupling, *npj Quantum Mater.* **10**, 109 (2025).
- [125] W.-J. Hu, S.-S. Gong, F. Becca, and D. N. Sheng, Variational Monte Carlo study of a gapless spin liquid in the spin- $\frac{1}{2}$ XXZ antiferromagnetic model on the kagome lattice, *Phys. Rev. B* **92**, 201105 (2015).
- [126] J. Romhányi, K. Totsuka, and K. Penc, Effect of Dzyaloshinskii-Moriya interactions on the phase diagram and magnetic excitations of $\text{SrCu}_2(\text{BO}_3)_2$, *Phys. Rev. B* **83**, 024413 (2011).
- [127] T. Chen, C. Guo, P. Sengupta, and D. Poletti, Effects of staggered Dzyaloshinskii-Moriya interactions in a quasi-two-dimensional Shastry-Sutherland model, *Phys. Rev. B* **101**, 064417 (2020).
- [128] H.-J. Yang and S. Lee, Topological phases of nonsymmorphic crystals: Shastry-Sutherland lattice at integer filling, *Phys. Rev. B* **99**, 165140 (2019).
- [129] Y. Ran, W.-H. Ko, P. A. Lee, and X.-G. Wen, Spontaneous Spin Ordering of a Dirac Spin Liquid in a Magnetic Field, *Phys. Rev. Lett.* **102**, 047205 (2009).
- [130] A. W. Sandvik, Computational studies of quantum spin systems, *AIP Conference Proceedings* **1297**, 135 (2010).
- [131] A. Wietek and A. M. Läuchli, Sublattice coding algorithm and distributed memory parallelization for large-scale exact diagonalizations of quantum many-body systems, *Phys. Rev. E* **98**, 033309 (2018).
- [132] L. Chen and Z.-X. Liu, Deconfined Gapless phases and criticalities in Shastry-Sutherland Antiferromagnet, (2025), [arXiv:2503.20122](https://arxiv.org/abs/2503.20122) [cond-mat.str-el].
- [133] Z. Yuan, M. Wu, D.-X. Yao, and H.-Q. Wu, Spiral Phase and Phase Diagram of the $S=1/2$ XXZ Model on the Shastry-Sutherland Lattice, (2026), [arXiv:2601.22924](https://arxiv.org/abs/2601.22924) [cond-mat.str-el].